Air Force Institute of Technology
AFIT Scholar

Theses and Dissertations   Student Graduate Works

6-19-2014

Enhanced Polarimetric Radar Imaging Using Cross-Channel Coupling Constraints

Andrea E. Perhai

Follow this and additional works at: https://scholar.afit.edu/etd

ENHANCED POLARIMETRIC RADAR IMAGING USING CROSS-CHANNEL

COUPLING CONSTRAINTS

THESIS

Andrea E. Perhai, Contractor, USAF

AFIT-ENG-T-14-J-9

AFIT-ENG-T-14-J-9

ENHANCED POLARIMETRIC RADAR IMAGING USING CROSS-CHANNEL

COUPLING CONSTRAINTS

THESIS

Presented to the Faculty

Department of Electrical and Computer Engineering

Graduate School of Engineering and Management

Air Force Institute of Technology

Air University

Air Education and Training Command

in Partial Fulfillment of the Requirements for the

Degree of Master of Science in Electrical Engineering

Andrea E. Perhai, B.A. Mathematics

Contractor, USAF

June 2014

AFIT-ENG-T-14-J-9

ENHANCED POLARIMETRIC RADAR IMAGING USING CROSS-CHANNEL

COUPLING CONSTRAINTS

Andrea E. Perhai, B.A. Mathematics
Contractor, USAF

Approved:

/signed/	20 May 2014
Julie A. Jackson, PhD (Chairman)	Date
/signed/	20 May 2014
Capt. Dustin G. Mixon, PhD (Member)	Date
/signed/	20 May 2014
Gilbert L. Peterson, PhD (Member)	Date

Abstract

Data for a scene of interest may be collected over multiple polarization channels. In the case of polarimetric synthetic aperture radar images, regularization techniques are typically applied independently to each polarimetric channel. However, independent processing does not account for cross-channel coupling and may corrupt the polarimetric information in the signals. Recent consideration of joint enhancement techniques has shown promising results for multi-channel datasets with similar regions of signal magnitude and/or phase. However, in the case of polarimetric SAR data, scattering may be present in some channels and not in others. This thesis mathematically formulates multi-channel sparse imaging for polarimetric radar data using a joint enhancement algorithm to enforce sparsity and polarimetric coupling constraints.

Two candidate functional relationships are derived to describe polarimetric coupling among received signal channels: one convex function and one non-convex function. These functions are reformed as optimization constraints. Then, an optimization problem is constructed to maintain signal fidelity, enforce sparsity, and preserve interchannel coupling. An iterative dual gradient descent algorithm is used to alternatively calculate updated scene estimates for each channel and the maximizing Lagrange multipliers for each coupling constraint. Results are found for several polarimetric SAR datasets. Jointly enhanced images are compared with corresponding images found through independent enhancement, taking into consideration signal fidelity, sparsity, polarimetric preservation, and scattering classification.

Overall, the jointly enhanced image channels display significantly better polarimetric preservation compared to the corresponding independently restored image channels. More research is needed to understand how improved polarimetric preservation can be used to improve target classification.

To my Dad.

Acknowledgments

I cannot express enough thanks to my advisor, Dr. Julie A. Jackson. I sincerely appreciate her guidance and patience throughout this entire project.

Andrea E. Perhai

Table of Contents

List of Figures

Figure   Page

xi

List of Tables

List of Acronyms

Acronym	Definition
RADAR	Radio Detection and Ranging
H	Horizontal
V	Vertical
SAR	Synthetic aperture radar
RGB	Red, Green, Blue
LFM	linear frequency modulated
I	in-phase
Q	quadrature
PFA	Polar Reformat algorithm
RIP	Restricted Isometry Property
WGN	White Gaussian noise
RCS	radar cross section
SNR	signal-to-noise Ratio

ENHANCED POLARIMETRIC RADAR IMAGING USING CROSS-CHANNEL COUPLING CONSTRAINTS

I. Introduction

Iɴ the late 1800's, physicist Heinrich Hertz demonstrated several important properties of electromagnetism that sparked widespread research interest in radio waves. Among these experiments, Hertz showed that radio waves can be transmitted, re-radiated by metallic objects, and then detected [1]. These important discoveries led to the development of Radio Detection and Ranging (RADAR). Early radar systems were simple and primarily used to determine a target's range and velocity in a given direction [2]. Modern radar systems also have the capability to track targets, determine a target's size and shape, form images of a scene of interest, and eliminate unwanted interference. Principles of radar have led to advancements in many fields including meteorology, law enforcement, military operations, and medicine [2].

The importance of wave polarization in radar was first studied extensively by George Sinclair in the 1940's [1]. Sinclair determined that radar targets transform the transmitted wave polarization based on target attributes such as material and shape. By transmitting and receiving both a Horizontal (H) and Vertical (V) polarization, Sinclair characterized basic properties of targets of interest [1]. Sinclair's foundational work led to significant advances in *polarimetry*, the study of target aspects that can be determined by changing the transmitted and received wave polarization state [1]. State-of-the-art radar systems use multiple transmit/receive polarization *channels* for automated target classification and interference reduction [3]. This thesis presents a method to preserve

the relationship between multiple radar polarization channels during sparsity-constrained image enhancement in order to improve scene estimates and target classification.

1.1 Motivation

Synthetic aperture radar (SAR) images contain impulse response effects that appear to smear or blur the image [4]. Sparse imaging is a regularization method which has proved desirable for many radar applications since it provides a way to remove smearing resulting from limited datasets [3]. In essence, regularization methods estimate scene reflectivity by reducing the impulse response effects. Sparsity constraints enforced alongside data fidelity constraints lead to signal energy placement in only high amplitude pixels [3]. Hence, enforcing sparsity in an image emphasizes high magnitude scatterers while reducing the effects of noise and the impulse response.

Often times, data for a scene of interest is collected over multiple channels, such as frequency, elevation, or polarization [5]. In the case of polarimetric SAR images, the regularization techniques are typically applied independently to each polarimetric channel. However, independent processing may corrupt the polarimetric information in the signals, as it does not account for cross-channel coupling. Recent research into joint enhancement techniques has shown promising results for multi-channel datasets with similar support regions, i.e., regions of similar signal magnitude and/or phase [5],[6]. However, in the case of polarimetric SAR data, scattering may be present in some channels and not in others. This thesis mathematically formulates multi-channel sparse imaging for polarimetric radar data using a joint enhancement algorithm to enforce sparsity and polarimetric coupling constraints.

1.2 Layout

Chapter 2 presents relevant background information on polarimetry, SAR, and current image enhancement techniques. The Sinclair scattering matrix is presented along with

related polarimetric decompositions, which are later used to formulate coupling constraints. Moreover, current techniques for independent and joint image enhancement are presented, as well as the problems that arise with each when considering polarimetric data.

Chapter 3 derives two possible functional relationships to describe polarimetric channel coupling among received signal channels. Then, an optimization problem is constructed to maintain signal fidelity, enforce sparsity, and preserve interchannel coupling. The convexity of the problem is analyzed. Finally, an algorithmic solution of the optimization problem is developed and a measure of scattering classification is defined.

In Chapter 4, the joint optimization problem is solved using the algorithm described in Ch. 3 for several polarimetric SAR datasets. These datasets include simulated radar data of various canonical scatterers. Jointly enhanced images are compared with corresponding images found through independent enhancement, taking into consideration signal fidelity, sparsity, polarimetric preservation, and scattering classification.

Chapter 5 concludes the findings of our research and provides ideas for future research into this topic.

II.   Background

T HIS chapter introduces the basics of polarimetry, synthetic aperture radar (SAR), and sparse imaging. Then, the multichannel imaging problem is introduced, including current methods for independent and joint image enhancement.

2.1   Notation

Scalars are denoted by italicized letters. Vectors and matrices are bold and single and double underlined, respectively, such as $\underline{f}$ and $\underline{\underline{M}}$. The ith entry in a vector is given by $\underline{f}(i)$. Similarly, the ijth entry in a matrix is denoted $\underline{\underline{M}}(i, j)$. A set of n vectors or matrices is denoted by a subscript such as $\underline{f}_1, \underline{f}_2, ..., \underline{f}_n$. The term $diag\{\cdot\}$ represents a diagonal matrix whose ii^{th} entry is defined by the expression in the brackets. The operator $(\cdot)^H$ represents the Hermitian operator for vectors and matrices, and represents the complex conjugate for scalars.

2.2   Polarimetry

In a monostatic radar system, the transmitting and receiving antennas are colocated [2]. An electromagnetic wave pulse is transmitted, interacts with a target of interest, and is reradiated non-uniformly in every direction. The backscattered pulse is collected at the receiver. The ideal signal power received at the antenna, P_r, is given by the radar range equation

$$P_r = \frac{P_t G^2 w^2 \sigma}{(4\pi)^3 R^4},\qquad(2.1)$$

where P_t is the transmitted signal power, G is the antenna gain, w is the wavelength, σ is the target radar cross section (RCS) and R is the one-way range from the radar to the target [2]. The RCS is determined by target characteristics such as size, shape, or material, and radar parameters such as wavelength and incidence angle [7]. The RCS is a measure of

detectability and hence provides an effective area of the target [7, 8]. Definitively,

$$\sigma = \lim_{R \to \infty} 4\pi R^2 \frac{|\underline{E}^r|^2}{|\underline{E}^t|^2} \quad \approx \quad 4\pi|S|^2 \text{ in the far field,} \tag{2.2}$$

where $|\underline{E}^{t,r}|^2$ represents the intensity of the transmitted and received electromagnetic waves, respectively, and $|S|$ is defined as the complex scattering amplitude of the wave [7, 8].

2.2.1 Scattering Matrix.

The RCS σ also depends on the polarization of the incident and scattered waves. Specifically,

$$\sigma_{pq} \approx 4\pi|S_{pq}|^2, \tag{2.3}$$

where p is the polarization of the transmitted/incident field and q is the polarization of the scattered/received field [1][7]. The polarization states p and q are orthogonal, such as a linear basis with horizontal and vertical components or circular basis with left and right components. For simplicity, this work assumes p, q are either horizontal (H) or vertical (V). The transmitted and received fields have components in the horizontal direction $\underline{\hat{h}}$ and vertical direction $\hat{\underline{v}}$, i.e.,

$$\underline{E}^t = E_V^t \hat{\underline{v}} + E_H^t \underline{\hat{h}}, \tag{2.4}$$

$$\underline{E}^r = E_V^r \hat{\underline{v}} + E_H^r \underline{\hat{h}}, \tag{2.5}$$

where E_H, E_V denote the horizontal and vertical components, respectively, of the incident and scattered fields [8]. A fully polarimetric radar can transmit and receive both horizontal and vertical polarizations. By alternating the transmit and receive polarization states, the radar collects all four complex scattering amplitudes. The entire scattering response is stored in the Sinclair or Scattering Matrix $\underline{\underline{S}}$, which relates the transmitted and received fields as $\underline{E}^r = \frac{e^{ik_0R}}{R}\underline{\underline{S}}\underline{E}^t$ [8][9]. Explicitly,

$$\begin{bmatrix} E_H^r \\ E_V^r \end{bmatrix} = \frac{e^{ik_0R}}{R} \begin{bmatrix} S_{HH} & S_{HV} \\ S_{VH} & S_{VV} \end{bmatrix} \begin{bmatrix} E_H^t \\ E_V^t \end{bmatrix}, \tag{2.6}$$

where k_0 is the wavenumber of the transmitted wave, and the term $\frac{e^{ik_0 R}}{R}$ accounts for magnitude and phase deviations due to propagation over the distance R [9].

The four scattering amplitudes in $\underline{\underline{S}}$ are complex-valued and hence contain both a magnitude and relative phase. Each scattering amplitude is a function of the radar frequency and the target aspect angle [8]. The diagonal elements are known as *co-polarization* terms since they relate the scattering amplitude for the same transmit and receive polarization. Similarly, the off-diagonal elements are known as *cross-polarization* terms since they relate perpendicular polarizations. In the case of monostatic radar, the cross-polarization terms are equal due to electromagnetic reciprocity [7–9]. Note that a backscatter coordinate system is assumed, which is radar-centric. Within this model, the horizontal and vertical transmit channels are initially off-set in phase by 180° or π radians [8, 9].

The material and geometry of a particular target determine the characteristics of the reradiated wave. When an incident pulse reflects once off a target surface, the signal is said to *single bounce*. Similarly, when an incident pulse is scattered by two surfaces of the target before returning to the receiver, the signal is said to *double bounce*. In general, wave pulses that deflect off of an odd number of surfaces are called *odd bounce*, and wave pulses that deflect off an even number of surfaces are called *even bounce* [10]. Physical boundary conditions on perfect conductors lead to a phase shift of 180° on every bounce [9]. Therefore, odd and even bounce scattering are determined from the phase difference of the co-polarization terms, S_{HH} and S_{VV}. The class of odd bounce scatterers have a scattering matrix of the form [7, 9, 11]

$$\underline{\underline{S}}_{odd} = \frac{1}{\sqrt{2}} \begin{bmatrix} 1 & 0 \\ 0 & 1 \end{bmatrix}. \qquad (2.7)$$

Backscatter from a perfect odd-bounce conductor leads to a 0° shift between the polarization channels, since the co-polarization terms are initially offset in phase by 180°.

Therefore, the co-polarization scattering magnitudes are equal, $|S_{HH}| = |S_{VV}|$. Similarly, the class of even bounce scatterers have a scattering matrix of the form [7, 9, 11]

$$\underline{\underline{S}}_{even} = \frac{1}{\sqrt{2}} \begin{bmatrix} 1 & 0 \\ 0 & -1 \end{bmatrix}. \tag{2.8}$$

Backscatter from a perfect even-bounce conductor leads to a 180° phase shift between the polarization channels [9], since two 180° phase shifts cancel, leaving the initial 180° shift. Therefore, the co-polarization scattering magnitudes are opposite, $|S_{HH}| = -|S_{VV}|$. Cross-polarization scattering, also called diffuse scattering, happens when the reradiated pulse is orthogonal to the one transmitted and hence bounce parity is unknown. The amount of diffuse scattering is determined by the cross-polarization magnitude, $|S_{HV}|$. The scattering matrix for the diffuse class of scatterers is given by [7, 9, 11]

$$\underline{\underline{S}}_{diffuse} = \begin{bmatrix} 0 & 1 \\ 1 & 0 \end{bmatrix}. \tag{2.9}$$

Common canonical shapes have a known scattering response and are often used for data calibration [10]. Canonical scatterers encompass a set of shapes including dihedrals, trihedrals, spheres, flat plates, cylinders and top-hats. These shapes are characterized by several parameters including: the (x, y, z) location of the shape, the length L, the height H, the radius r, and the roll, pitch and yaw angles [10]. The roll, pitch, and yaw angles define the counterclockwise rotation of the shape with respect to the x, y, and z axis, respectively. In general, dihedrals and top-hats are even bounce scatterers and plates, trihedrals, cylinders, and spheres are odd bounce scatterers [11]. Figure 2.1 shows an example of all these shapes. In Chapter 4, we use the plate, dihedral, and top-hat to illustrate the proposed polarization-preserving image enhancement techniques.

A rectangular plate is an odd bounce scatterer that is characterized as an object with one flat surface. Reflected energy from a plate is directionally dependent [8, 10],

(a) Plate   (b) Dihedral   (c) Trihedral

(d) Cylinder   (e) Top-hat   (f) Sphere
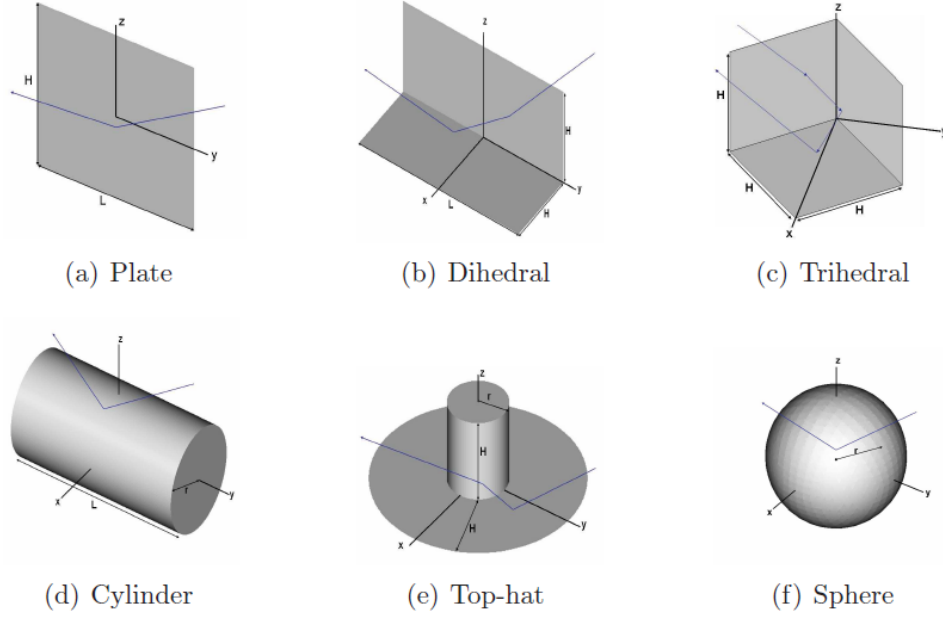
Figure 2.1: The six canonical shapes characterized by [10].

and thus backscattered energy is only received by a monostatic radar when the plate is normal to the transmitted signal. A plate with (roll,pitch,yaw) = $(0°, 0°, 0°)$ and location $(x, y, z) = (0, 0, 0)$ is as pictured in Figure 2.1a. The peak RCS σ_{plate} is defined as [10]

$$\sigma_{plate} = \frac{4\pi L^2 H^2}{w^2},\tag{2.10}$$

where w is the radar wavelength.

Dihedrals are even bounce scatterers formed from two flat plates joined at a 90° angle. A dihedral with (roll,pitch,yaw) = $(0°, 0°, 0°)$ and location $(x, y, z) = (0, 0, 0)$ is as pictured in Figure 2.1b. The peak RCS $\sigma_{dihedral}$ is given by[10]

$$\sigma_{dihedral} = \frac{8\pi L^2 H^2}{w^2}.\tag{2.11}$$

The top-hat is an even bounce scatterer that is formed from a circular flat plate and cylinder. A top-hat with (roll,pitch,yaw) = $(0°, 0°, 0°)$ and location $(x, y, z) = (0, 0, 0)$ is as

pictured in Figure 2.1e. The top-hat has a peak RCS σ_{tophat} given by [10]

$$\sigma_{tophat} = \frac{8\pi r H^2}{w \sqrt{2}}. \tag{2.12}$$

2.2.2 Polarimetric Decompositions and Classification.

In general, a scattering matrix $\underline{\underline{S}}$ corresponds to a complex coherent target that is a composite of many scatterer responses [11]. Information about the target cannot be obtained purely from $\underline{\underline{S}}$. Instead, useful information is obtained by decomposing $\underline{\underline{S}}$ into a combination of scattering responses of canonical shapes [7, 11]. The Pauli decomposition is one standard basis used to decompose a scattering matrix [1, 7]. It characterizes $\underline{\underline{S}}$ in terms of the standard scattering matrices of a sphere $\underline{\underline{S}}_{odd}$, dihedral $\underline{\underline{S}}_{even}$, and dihedral with $-45°$ pitch angle $\underline{\underline{S}}_{diffuse}$. Specifically, the Pauli decomposition is given as [7, 9]

$$\underline{\underline{S}} = a\underline{\underline{S}}_{odd} + b\underline{\underline{S}}_{even} + c\underline{\underline{S}}_{diffuse} \tag{2.13}$$

where

$$a = \frac{S_{HH} + S_{VV}}{\sqrt{2}} \tag{2.14}$$

$$b = \frac{S_{HH} - S_{VV}}{\sqrt{2}} \tag{2.15}$$

$$c = \sqrt{2}S_{HV}. \tag{2.16}$$

The Pauli basis decomposition constants are such that $|a|^2$ is the power scattered by targets with odd bounce, $|b|^2$ is the power scattered by targets with even bounce and $|c|^2$ is the power from diffuse scattering [7]. Similarly, the Krogager decomposition characterizes the scattering matrix by the responses of a sphere, diplane and helix [7].

The Pauli and Krogager polarimetric decompositions provide a simple target classification based on bounce type. Knowledge of the bounce type is useful to distinguish between natural and man-made targets [12], and for automatic target recognition algorithms which look for salient features to classify a target [11, 12]. Moreover, knowledge of $\underline{\underline{S}}$ allows for full polarimetric characterization of the scattering for the target of interest [8],

9
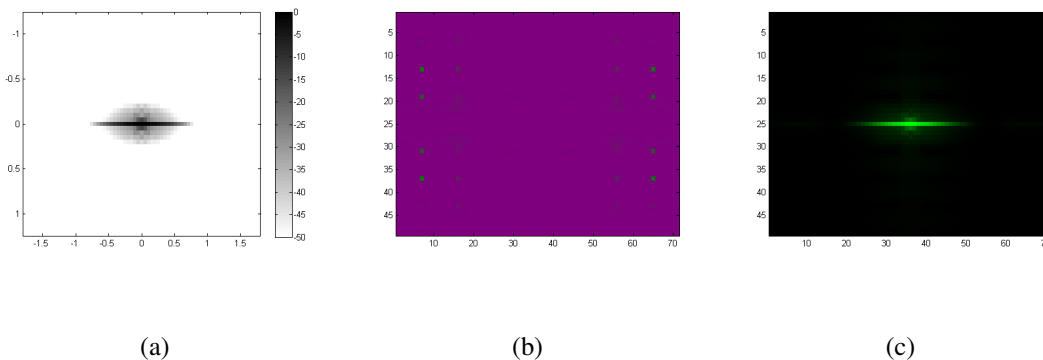
Figure 2.2: The (a) gray-scale SPAN (b) color coded SPAN, and (c) Pauli basis decomposition of a dihedral.

and hence, the scattering response can be determined in any polarimetric basis. Changing the polarimetric basis allows one to determine the scattered polarization state for any incident polarization state, perhaps to enhance specific features of interest, by applying signal processing techniques instead of physical antenna changes [8, 9].

2.2.3 *Polarimetric Image Formation.*

Since a fully polarimetric radar is a multichannel system, all the polarimetric channels must be considered to determine the total scattered power, or SPAN, at a given pixel. The SPAN is given by [7]

$$\text{SPAN} = |S_{HH}|^2 + 2|S_{HV}|^2 + |S_{VV}|^2. \tag{2.17}$$

The SPAN can be presented as a gray-scale image, where the intensity of a given pixel represents the relative SPAN magnitude at that pixel. Figure 2.2(a) shows an example of this type of image. While this method does effectively image a scene of interest, the polarimetric information is not portrayed.

The SPAN can also be presented as a color-coded image where the relative term intensities represent the color weights on a Red, Green, Blue (RGB) scale [7, 8]. For example, let $|S_{HH}|^2$ correspond to red, $2|S_{HV}|^2$ correspond to green, and $|S_{VV}|^2$ correspond

10

to blue. Figure 2.2(b) shows an example of this type of image. The polarimetric information is portrayed in this image; however, the physical interpretation of the colors can be difficult to comprehend. Furthermore, notice that in both gray-scale and color-coded SPAN images, no information is portrayed about the relative phase.

One method to present both the polarimetric information and relative phase is through a scattering matrix decomposition. For instance, the Pauli decomposition can be presented as a color-coded image where $|a|^2$, $|b|^2$, and $|c|^2$ represent the relative weights on an RGB scale [1, 7]. In this case, the polarimetric information is portrayed with a meaningful physical interpretation and the relative phase is captured within a and b. Notice that SPAN $= |a|^2 + |b|^2 + |c|^2$, so the total scattered power is maintained. Figure 2.2(c) shows an example of a dihedral in the Pauli basis decomposition. Notice that the dihedral appears green, since it is an even bounce structure.

2.3 Synthetic Aperture Radar

A synthetic aperture radar (SAR) is a radar system that simulates a large antenna aperture by moving a small antenna over a large aperture extent [4]. The dual nature of SAR allows for creation of high resolution ground images. Images are created of the measured ground reflectivity of a scene of interest. There are two SAR modes, stripmap and spotlight, which distinguish the scene geometry based on the radar. In stripmap mode, the radar beam points in a fixed direction for the desired aperture duration. In spotlight mode, the radar beam points at a fixed target for the desired aperture duration [4][2]. Circular flight paths are optimal for spotlight mode since data is collected for a full 360° aperture. This work assumes the use of spotlight mode SAR with a known radar flight path.

Typically, a SAR transmits a linear frequency modulated (LFM) chirp $s(t)$ given by [4, 13]

$$s(t) = \begin{cases} e^{j(f_0 t + \alpha t^2)}, & -\frac{\tau_c}{2} \leq t \leq \frac{\tau_c}{2} \\ 0, & \text{else} \end{cases}, \tag{2.18}$$

11
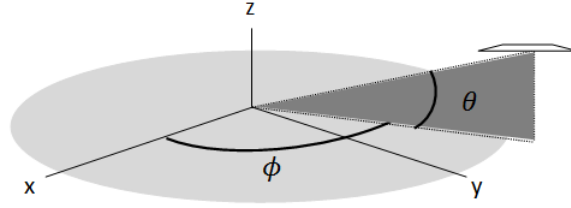
Figure 2.3: Illustration of grazing angle θ and azimuth angle ϕ.

where f_0 is the carrier frequency, α is the chirp rate, and τ_c is the time duration of the chirp. The received signal $r(t)$ is first mixed with delayed in-phase (I) and quadrature (Q) versions of the transmitted chirp and then low-pass filtered. Denote this signal $r_c(t)$. Thus, [4, 13]

$$r_c(t) = \frac{A}{2} \int_{-u_1}^{u_1} g(u) e^{j\frac{4\alpha u^2}{c^2}} e^{-j\frac{2u}{c}(f_0 + 2\alpha(t-\tau_0))} du, \tag{2.19}$$

where A is a scale factor that accounts for attenuation effects, $g(u)$ is the scene reflectivity function, u is the distance along the range direction, c is the speed of light, τ_0 is the time delay from the radar platform to the scene center, and the interval $[-u_1, u_1]$ denotes the radar range based on chirp duration. Notice that by ignoring the quadratic phase skew term $\frac{4\alpha u^2}{c^2}$, the desired scene reflectivity function $g(u)$ is the inverse Fourier transform of $r_c(t)$[13]. The signal $r_c(t)$ is also known as phase history data.

Phase history data is measured at each grazing angle θ and azimuth angle ϕ, as shown in Figure 2.3, where $(0, 0, 0)$ corresponds to the scene center [4]. Assume the grazing angle is constant throughout the flight path. Backprojection [14] or Polar Reformat [4] algorithms are used to accurately combine the information from all azimuth samples to create an image of the scene. The backprojection algorithm is based on tomographic imaging principles [14]. For each (x, y) coordinate in the scene extent, the inverse Radon transform is computed to sum the reflectivity contributions from each azimuth angle at that point [14]. Alternatively, the Polar Reformat algorithm (PFA) interpolates the range and azimuth samples into a Cartesian raster before performing a two-dimensional Fourier

transform [4]. This research uses PFA to find scene reflectivity. The range resolution ρ_r and cross-range resolution ρ_c are determined by the bandwidth and aperture extent. Specifically, [4]

$$\rho_r = \frac{c}{2B_c}, \qquad \rho_c = \frac{w}{2\Delta\phi}, \tag{2.20}$$

where B_c is the chirp bandwidth, w is the radar wavelength, and $\Delta\phi$ is the aperture extent.

The ideal phase history data can also be thought of as a complex vector $\underline{r}$ of signal magnitude and phase. Then, the sampled scene reflectivity $\underline{x}$ is the Fourier Transform of $\underline{r}$. Hence,

$$\underline{r} = \underline{\underline{\Psi}}\,\underline{x}, \tag{2.21}$$

where $\underline{\underline{\Psi}}$ denotes the Fourier Transform matrix. In other words, $\underline{r}$ is a linear combination of the basis $\underline{\underline{\Psi}}$ with coefficients $\underline{x}$. The complex measured phase history $\underline{y}$ is then given by [15]

$$\underline{y} = \underline{\underline{\Phi}}\,\underline{r} = \underline{\underline{\Phi}}\,\underline{\underline{\Psi}}\,\underline{x} = \underline{\underline{\Theta}}\,\underline{x}, \tag{2.22}$$

where $\underline{\underline{\Phi}}$ is the measurement matrix which accounts for the limited nature of data collection that transforms $\underline{r}$ to $\underline{y}$ and $\underline{\underline{\Theta}} = \underline{\underline{\Phi}}\,\underline{\underline{\Psi}}$. The matrix $\underline{\underline{\Psi^{-1}\Phi\Psi}}$ represents the radar point spread function, which indicates the multi-dimensional impulse response of the imaging system. The observed scene reflectivity $\underline{\underline{\Psi}}^{-1}\underline{y}$ is a convolution of the point spread function with $\underline{x}$. Ideally, the scene reflectivity $\underline{x}$ is recovered by deconvolution of the point spread function.

2.4 The Assumption of Sparsity

In reality, the received signal contains a large amount of interference due to clutter, thermal noise, and smearing from the impulse response. Due to bandlimited and aperture-limited data collection, $\underline{\underline{\Theta}}$ is ill-posed and therefore not invertible [3]. It follows that directly using scattering matrix decomposition theory on the received signal produces images that may give incorrect information to the user, such as a misclassified target. The smearing effects first need to be reduced from the received signal. If it is assumed that

13

the scene of interest has discrete scatterers, then the received signal will be sparse and can be represented in a basis with only a few nonzero entries [3, 15]. Sparse imaging is a regularization method that estimates the scene reflectivity by putting signal energy in only high amplitude pixels, thus emphasizing targets and reducing noise and smearing.

The assumption of sparsity holds when the measurement matrix $\underline{\underline{\Phi}}$ satisfies the Restricted Isometry Property (RIP) [3]. RIP describes matrices which are orthogonal or close to orthogonal. Specifically, $\underline{\underline{\Phi}}$ should satisfy the relationship [3]

$$(1 - \delta_k)\|\underline{x}\|_2^2 \; \leq \; \|\underline{\underline{\Phi}}\underline{x}\|_2^2 \; \leq \; (1 + \delta_k)\|\underline{x}\|_2^2, \tag{2.23}$$

where δ_k is the restricted isometry constant and $\underline{x}$ is the vector of measured data. The radar collection model has sufficient performance guarantees which validate the use of sparse reconstruction [3].

The system of equations in Eq. (2.22) is under-determined. The sparse estimate for the measured data, $\hat{\underline{x}}$, is given by

$$\hat{\underline{x}} = \arg \min_{\underline{x}} \|\underline{x}\|_0 \quad \text{s.t.} \quad \|\underline{y} - \underline{\underline{\Theta}}\underline{x}\|_2^2 \leq \epsilon_1, \tag{2.24}$$

where the ℓ_2 norm preserves the accuracy of the signal and ϵ_1 is a predetermined infinitesimal scalar corresponding to the level of error allowed [3][15]. However, the ℓ_0 norm is an NP-complete problem and is therefore impractical for real-world applications. Switching the ℓ_0 to an ℓ_1 norm finds a relaxed sparse solution [15]. By including the constraint directly in the objective function, the sparsity can be enforced through a regularization parameter, λ. This produces the least squares problem [3, 15]

$$\hat{\underline{x}} = \arg \min_{\underline{x}} \|\underline{y} - \underline{\underline{\Theta}}\underline{x}\|_2^2 + \lambda\|\underline{x}\|_1. \tag{2.25}$$

Note that the Lagrange multiplier λ is a positive scalar [16]. The ideal value of λ for a particular scenario can be found though a dual optimization problem [17]. This research considers sparse enhancement over various values of λ.

2.5 Multichannel Enhancement

Often times, data for a scene of interest is collected over multiple channels, such as frequency, elevation, or polarization. Since the channels carry common and/or complementary information about the same scene, combining the channels proves useful for improving estimates of appropriate scene attributes [3]. For example, data from multiple elevations can be used to refine height estimates of scatterers within a scene [5]. Multichannel images are formed using signal processing techniques to enhance and combine multiple image channels. Enhancement is typically done independently for each channel. Recent research has also considered joint enhancement, which involves simultaneously enhancing each channel based on a known interchannel relationship [5, 6]. In [5], scatterer height estimates are shown to be more accurate using joint enhancement versus independent enhancement techniques. Furthermore, in [6] the interchannel covariance matrix is used to improve signal estimates and reduce noise in hyperspectral imaging. Our work specifically considers image enhancement through the assumption of sparsity.

2.5.1 Independent Enhancement.

Independent enhancement is appropriate for a single image or multiple independent images. In the case of polarimetric data, independently enhancing each polarimetric channel may corrupt the original signal or phase ratio between the channels by modifying energy placement in the pixels. The outcome is an inferior solution that ignores the interchannel coupling.

Sparse solution estimates for n multichannel images each with N pixels are found independently for each channel through the least squares problem [18]

$$\hat{\underline{x}}_1, \hat{\underline{x}}_2, ..., \hat{\underline{x}}_n = \arg\min_{\underline{x}_1,\underline{x}_2,...,\underline{x}_n} \sum_{i=1}^{n} C(\underline{x}_i), \qquad (2.26)$$

where the objective function $C(\underline{x}_i)$ is given by

$$C(\underline{x}_i) = \|\underline{y}_i - \underline{\underline{\Theta}}_i \underline{x}_i\|_2^2 + \lambda_i \|\underline{x}_i\|_1. \qquad (2.27)$$

15

Hence, a particular enhanced image $\hat{\underline{x}}$ based on the phase history $\underline{y}$ is given by

$$\hat{\underline{x}} = \arg\min_{\underline{x}} \ \|\underline{y} - \underline{\underline{\Theta}}\underline{x}\|_2^2 + \lambda\|\underline{x}\|_1. \tag{2.28}$$

Most numeric solutions of Eq. (2.27) involve determining the gradient of C. To avoid differentiating the ℓ_1 norm for values of $\underline{x}$ close to zero, $\|\underline{x}\|_1$ is approximated as [5, 18]

$$\|\underline{x}\|_1 \approx \sum_{j=1}^{N} (|\underline{x}(j)|^2 + \epsilon)^{1/2}. \tag{2.29}$$

It follows that

$$\hat{\underline{x}} \ \cong \ \arg\min_{\underline{x}} \ (\underline{y} - \underline{\underline{\Theta}}\underline{x})^T(\underline{y} - \underline{\underline{\Theta}}\underline{x}) + \lambda\sum_{j=1}^{N}(|\underline{x}(j)|^2 + \epsilon)^{1/2} \tag{2.30}$$

$$= \ \arg\min_{\underline{x}} \ \underline{y}^T\underline{y} - 2\underline{y}^T\underline{\underline{\Theta}}\underline{x} + \underline{x}^T\underline{\underline{\Theta}}^T\underline{\underline{\Theta}}\underline{x} + \lambda\sum_{j=1}^{N}(|\underline{x}(j)|^2 + \epsilon)^{1/2}. \tag{2.31}$$

The gradient with respect to $\underline{x}$ is given by [5]

$$\nabla_{\underline{x}} \ = \ -2\underline{\underline{\Theta}}^T\underline{y} + 2\underline{\underline{\Theta}}^T\underline{\underline{\Theta}}\underline{x} + \lambda\sum_{j=1}^{N} \frac{|(\underline{x})_j|}{(|(\underline{x})_j|^2 + \epsilon)^{1/2}} \tag{2.32}$$

$$= \ -2\underline{\underline{\Theta}}^T\underline{y} + 2\underline{\underline{\Theta}}^T\underline{\underline{\Theta}}\underline{x} + \lambda\underline{\underline{\Gamma}}(\underline{x})\underline{x}, \tag{2.33}$$

where $\underline{\underline{\Gamma}}(\underline{x}) = diag\left\{\frac{1}{(|(\underline{x})_j|^2+\epsilon)^{1/2}}\right\}$. Note that the approximate Hessian matrix is given by $\underline{\underline{H}} \approx 2\underline{\underline{\Theta}}^T\underline{\underline{\Theta}} + \lambda\underline{\underline{\Gamma}}(\underline{x})$ [18].

The least squares problem in Eq. (2.26) has no closed form solution for $\lambda \neq 0$ [16]. However, Eq. (2.26) can also be phrased as a linear program or second order cone program which are well known convex optimization problems [16]. Optimization schemes such as conjugate gradient descent or quasi-Newton methods can be used to find a minimizing solution [16]. However, these methods may be slow to converge due to expensive computations. In [16], an algorithm is developed using Optimization Transfer to iteratively converge while avoiding expensive computations. The output of each iterate k is an estimate of the enhanced image, $\hat{\underline{x}}^k$. Within the $(k + 1)^{th}$ iterate, a surrogate function $M(\underline{x}; \hat{\underline{x}}^k)$ is formed and minimized. Hence,

$$\hat{\underline{x}}^{k+1} = \arg\min_{\underline{x}} M(\underline{x}; \hat{\underline{x}}^k). \tag{2.34}$$

The minimum of a proper surrogate function will converge to the minimum of the original objective function [16]. In other words,

$$\lim_{k \to \infty} \arg \min_{\hat{\underline{x}}^k} M(\underline{x}; \hat{\underline{x}}^k) = \arg \min_{\underline{x}} C(\underline{x}). \tag{2.35}$$

To guarantee the convergence in Eq. (2.35), the surrogate function must be monotonically non-increasing and differentiable. To solve the problem in Eq. (2.35), the authors of [16] derive the quadratic surrogate function

$$M(\underline{x}; \hat{\underline{x}}^k) = \|\underline{y} - \underline{\underline{\Theta}}\underline{x}\|_2^2 + \lambda \sum_{i=1}^{N} |\hat{\underline{x}}^k(i)| + \text{Re}\left\{ \left(|\hat{\underline{x}}^k(i)| \right)^* \left(\underline{x}(i) - \hat{\underline{x}}^k(i) \right) \right\} + \frac{|\hat{\underline{x}}^k(i)| \|\underline{x}(i) - \hat{\underline{x}}^k(i)|^2}{2\hat{\underline{x}}^k(i)}. \tag{2.36}$$

The closed form solution of the $(k + 1)^{th}$ iterate is [16]

$$\hat{\underline{x}}^{k+1} = \left[\underline{\underline{\Theta}}^H \underline{\underline{\Theta}} + \frac{\lambda}{2} \underline{\underline{D}}(\hat{\underline{x}}^k) \right]^{-1} \underline{\underline{\Theta}}^H \underline{y}, \tag{2.37}$$

where $\underline{\underline{D}}(\hat{\underline{x}}^k) = diag\left\{ \frac{|\hat{\underline{x}}^k(i)|}{\hat{\underline{x}}^k(i)} \right\}$. However, the closed-form solution is costly to calculate for each iterate. Therefore, preconditioned conjugate gradient methods [16] are used to find the minimum of Eq. (2.36) at each iterate, and Fast Fourier Transforms are used for convolution. We employ the algorithm from [16] to obtain results for independent enhancement.

2.5.2   Joint Enhancement.

Suppose the channels are known to be coupled through a set of functions. In this case, it is appropriate to include the coupling functions as additional optimization constraints. Current joint optimization problems are formulated as [5][19]

$$\hat{\underline{x}}_1, \hat{\underline{x}}_2, ..., \hat{\underline{x}}_n = \arg \min_{\underline{x}_1, \underline{x}_2, ..., \underline{x}_n} \sum_{i=1}^{n} C(\underline{x}_i)$$

$$\text{s.t. } \sum_{i=1}^{n} h_{ij}(\underline{x}_i) = 0, \ j = 1...N, \tag{2.38}$$

where the real-valued coupling functions $\sum_{i=1}^{n} h_{ij}(\underline{x}_i)$ are continuous and N is the number of image pixels. Note that the coupling functions have an independent additive form, which implies that the individual images may be still be independently enhanced [5].

17

A method for solution involves incorporating the constraint functions into the objective function through the use of Lagrange multipliers [5]. Assume that a local minimum point $(\underline{x}'_1, .., \underline{x}'_n)$ exists. Hence, there exists a Lagrange multiplier β'_j for each set of constraints $\left\{ h_{1j}(\underline{x}_1), h_{2j}(\underline{x}_2), ..., h_{nj}(\underline{x}_n) \right\}$ which corresponds to the local minimum. It follows that the analogous unconstrained objective function is given by [5]

$$\sum_{i=1}^{n} C(\underline{x}_i) + \underline{\beta'}^T \underline{h}, \tag{2.39}$$

where $\underline{h}$ is the stack of constraint functions given by

$$\underline{h} = \left[\sum_{i=1}^{n} h_{i1}(\underline{x}_i), \sum_{i=1}^{n} h_{i2}(\underline{x}_i), ..., \sum_{i=1}^{n} h_{iN}(\underline{x}_i) \right]^T, \tag{2.40}$$

and $\underline{\beta'}$ is a vector such that $\underline{\beta'}(j) = \beta'_j$. Moreover, (2.39) is locally convex around $(\underline{x}'_1, ..., \underline{x}'_n)$. Using the Local Duality Theorem, Eq. (2.38) is equivalent to the dual function [5]

$$\hat{\underline{x}}_1, \hat{\underline{x}}_2, ..., \hat{\underline{x}}_n = \arg \max_{\underline{\beta}} \ \arg \min_{\underline{x}_1, \underline{x}_2, ..., \underline{x}_n} \sum_{i=1}^{n} C(\underline{x}_i) + \underline{\beta}^T \underline{h}, \tag{2.41}$$

for any $\underline{\beta}$ locally near $\underline{\beta'}$.

Notice that the optimization problem in (2.41) involves solving for both the Lagrange multipliers β_j and the enhanced images $\underline{x}_i$. The Dual Descent algorithm [5] is a numerical optimization scheme which employs a dual gradient descent to solve for the Lagrange multipliers and enhanced images. In particular, the Dual Descent algorithm fixes the set of β_j while solving for the restored images $\underline{x}_i$ and then subsequently fixes the set of restored images $\underline{x}_i$ to solve for the set of β_j [5]. The process is repeated until the relative change in both β_j and the restored images has been sufficiently minimized.

Specifically, the estimated Lagrange multiplier vector $\hat{\underline{\beta}}$ is updated for each iterate k using the gradient based equation [5]

$$\hat{\underline{\beta}}^k = \hat{\underline{\beta}}^{k-1} + \alpha \underline{h}^{k-1}, \tag{2.42}$$

where $\underline{h}^{k-1}$ is the set of constraint functions based on the $(k-1)^{th}$ image estimates, $\hat{\underline{x}}_1^{k-1}, ..., \hat{\underline{x}}_n^{k-1}$. Subsequently, the enhanced image estimates for an iterate k are found by

18

Input: Measured images $\underline{y}_i$, forward operators $\underline{\underline{\Theta}}_i$, sparseness parameters p, λ_i, stepsize α, and convergence parameters δ_1, δ_2, where $i = 1, ..., n$.

Output: Jointly enhanced images $\underline{x}_i$, where $i = 1, .., n$.

Initialize: $\underline{x}_i^0 = \underline{y}_i$, $\underline{\beta}^0 = 1$, and $\nabla_{\underline{\beta}^0} = \sum_{i=1}^{n} h_{ij}(\underline{x}_i^0)$, $j = 1, .., N$.

Algorithm:
while $e > \delta_2$ do
    Calculate $\underline{\beta}^{k+1} = \underline{\beta}^k + \alpha \nabla_{\underline{\beta}^k}$
    while Relative change in all $\underline{x}_i^l > \delta_1$ **do**
        Form diagonal matrix $\underline{\underline{\Gamma}}_i$ using $\underline{x}_i^l$
        Solve for $\underline{x}_i^{l+1}$ given $\underline{\beta}^{k+1}$
        Calcuate relative change in $\underline{x}_i^l$ given as $\frac{\|\underline{x}_i^{l+1} - \underline{x}_i^l\|}{\|\underline{x}_i^l\|}$
    end while
    Save solution as $\underline{x}_i^{k+1} = \underline{x}_i^{l+1}$
    Calculate $\nabla_{\underline{\beta}^{k+1}} = \sum_{j=1}^{N} h_j(\underline{x}_1^{k+1}, ..., \underline{x}_n^{k+1})$
    Calculate relative change in $\underline{\beta}$ given as $e = \dfrac{\left| \text{Cost fn using } \underline{\beta}^{k+1} - \text{Cost fn using } \underline{\beta}^k \right|}{\left| \text{Cost fn using } \underline{\beta}^k \right|}$
end while
Output $\underline{x}_i = \underline{x}_i^{k+1}$

Figure 2.4: Pseudocode for the Dual Descent Algorithm [5].

minimizing (2.35) using conjugate gradient or quasi-Newton methods. Table 2.1 shows the pseudocode for the Dual Descent method. The Dual Descent method provides a starting point to solve the joint enhancement problem for polarimetric radar data.

2.5.3 Issues.

Recent research into joint enhancement has shown promising results for multichannel images with similar support regions, such as signal magnitude or phase [5, 6]. In the case of polarimetric data, specific scatterers have high signal strength in some channels but not in others. This is true for a dihedral, which has similar support in the S_{HH} and S_{VV} channels,
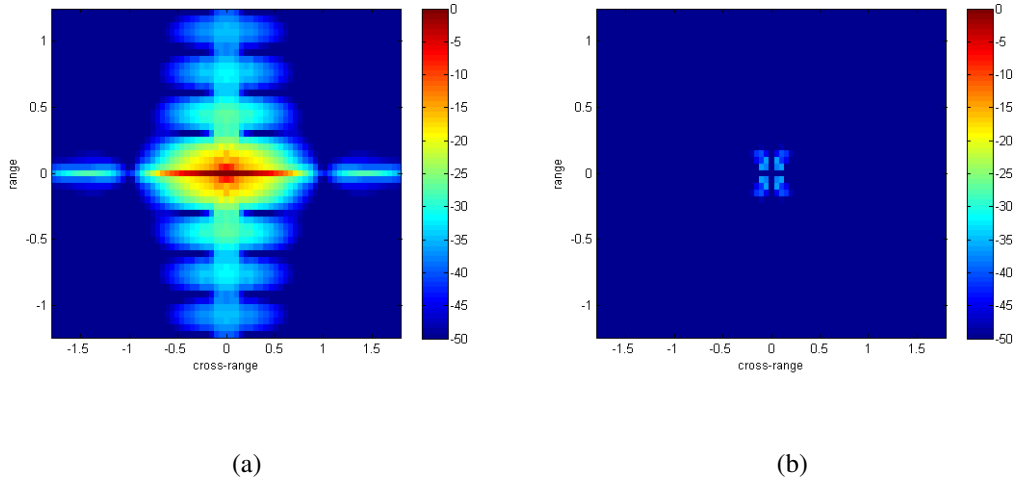
Figure 2.5: The (a) $|S_{HH}|$ ($= |S_{VV}|$), and (b) $|S_{HV}|$ unenhanced responses of a dihedral.

but has a low response in the S_{HV} channel. Figure 2.4 shows the scattering responses of the dihedral.

Moreover, the formulation of coupling constraints in Equation (2.38) does not account for interchannel relationships in which an independent additive form cannot be achieved. For example, consider the convex function

$$h(\underline{z_1}, \underline{z_2}) = \frac{1}{2}|\underline{z}_1 + \underline{z}_2|. \tag{2.43}$$

Notice that without further assumptions (2.43) cannot be written in the form $h(\underline{z}_1, \underline{z}_2) = h_1(\underline{z}_1) + h_2(\underline{z}_2)$, where h_1, h_2 are any convex functions. Similarly, the relationship between polarimetric channels given by scattering matrix decomposition does not follow an independent additive form. Consequently, the generalized joint enhancement theory must be modified before application to polarimetric data. Chapter 3 presents such a generalized method.

III.   Joint Enhancement of Polarimetric Data

Radar data may be collected over multiple polarization channels [3]. Channels may carry common and/or complementary information about the scene of interest. Combining appropriate channels produces improved estimates of scene attributes [5]. Multichannel images are formed by enhancing and combining multiple image channels. This research specifically considers image enhancement using the assumption of sparsity.

Although image enhancement is usually done independently for each channel, recent research has showed promising results for joint image enhancement [5][6]. Joint image enhancement accounts for the interchannel relationship that exists when multiple channels are coupled through a known set of functions. The Dual Descent algorithm is a current scheme designed to optimize the tradeoff between sparsity in the image and preservation of interchannel relationships that satisfy Eq. (2.38) [5]. Joint enhancement has proved successful for multichannel datasets with similar support regions, such as signal magnitude or phase [5, 6, 19]. In the case of polarimetric radar data, the received signal may be different from one channel to the next. However, the polarimetric channels are related to one another and together provide useful information about the scattering of a target of interest. It is important to preserve the interchannel relationship during image enhancement.

This section derives two functional relationships to describe polarimetric channel coupling among received signal channels. Then, an optimization problem is constructed to maintain signal fidelity, enforce sparsity, and preserve interchannel coupling. The convexity of the solution is analyzed. Finally, an algorithmic solution of the optimization problem is developed.
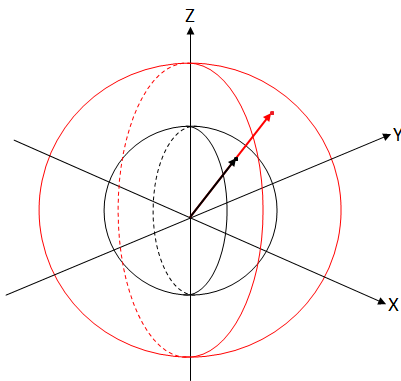
Figure 3.1: Illustration of a polarization state vector mapped onto the Poincaré Sphere shown in red, and scaled sub-sphere shown in black.

3.1 Non-Convex Constraint for Polarimetric Data

Recall that a fully polarimetric monostatic radar produces three distinct polarimetric data channels: S_{HH}, S_{HV} and S_{VV}. For clarity, let $\underline{y}_{HH}$, $\underline{y}_{HV}$, $\underline{y}_{VV}$ and $\underline{x}_{HH}$, $\underline{x}_{HV}$, $\underline{x}_{VV}$ represent the received phase history and enhanced scene reflectivity of the S_{HH}, S_{HV} and S_{VV} channels, respectively. The three enhanced polarimetric channels $\underline{x}_{HH}$, $\underline{x}_{HV}$, and $\underline{x}_{VV}$ are the foundation for a variety of radar applications including data calibration and target classification, and therefore, need to be accurate signals with precise interchannel relationships.

The Poincaré Polarization sphere [7, 9] provides a useful picture of all possible scattered polarization states. In particular, each point on the sphere corresponds to a specific scattered polarization state. Recall that the scattered polarization state can be fully described by the incident polarization state and the scattering matrix. Therefore, preservation of the scattering matrix is important to maintain the proper direction vector of the point on the Poincaré sphere, i.e., the precise scattered polarization state. Although the radius of the Poincaré sphere is informative, the direction vector fully describes the polarization state [7]. Permitting the radius to change but maintaining the vector direction allows for signal sparsity without changing the inherent information about the polarization

22

state. To preserve the vector direction, the contributions of the enhanced channels should remain proportional to the contributions of the received channels. Moreover, the phase between channels is informative for the classification of scattering types. Since phase is captured within a complex exponential, the ratio of any two channels gives the phase differences as well as the ratio of the signal magnitudes. Therefore, we propose an appropriate coupling constraint

$$
h_j(\underline{x}_{HH}, \underline{x}_{HV}, \underline{x}_{VV}) = \left| \frac{\underline{y}_{HH}(j)}{\underline{y}_{VV}(j)} - \frac{\underline{x}_{HH}(j)}{\underline{x}_{VV}(j)} \right| + \left| \frac{\underline{y}_{HV}(j)}{\underline{y}_{VV}(j)} - \frac{\underline{x}_{HV}(j)}{\underline{x}_{VV}(j)} \right| + \left| \frac{\underline{y}_{HV}(j)}{\underline{y}_{HH}(j)} - \frac{\underline{x}_{HV}(j)}{\underline{x}_{HH}(j)} \right|, \quad (3.1)
$$

to preserve relative channel magnitudes and phase differences. The real-valued constraint of Eq. (3.1) is a measure of the absolute error between received and enhanced polarimetric ratios for each resolution cell j, or pixel, in the image. Polarimetric preservation occurs when $h_j(\underline{x}_{HH}, \underline{x}_{HV}, \underline{x}_{VV}) = 0$ for each pixel j.

3.1.1 Convexity.

Consider the convexity of h_j. Clearly, h_j is not a linear function. In general, a function is convex if the Hessian is positive semidefinite [20]. The Lagrangian $\nabla h_j(\underline{x}_{HH}, \underline{x}_{HV}, \underline{x}_{VV})$ is given by

$$
\nabla h_j(\underline{x}_{HH}, \underline{x}_{HV}, \underline{x}_{VV}) = \left[\frac{\partial h_j}{\partial \underline{x}_{HH}(j)} \quad \frac{\partial h_j}{\partial \underline{x}_{HV}(j)} \quad \frac{\partial h_j}{\partial \underline{x}_{VV}(j)} \right]^T, \quad (3.2)
$$

where

$$\frac{\partial h_j}{\partial \underline{x}_{HH}(j)} = \frac{\partial}{\partial \underline{x}_{HH}(j)} \left\{ \left| \frac{\underline{y}_{HH}(j)}{\underline{y}_{VV}(j)} - \frac{\underline{x}_{HH}(j)}{\underline{x}_{VV}(j)} \right| + \left| \frac{\underline{y}_{HV}(j)}{\underline{y}_{VV}(j)} - \frac{\underline{x}_{HV}(j)}{\underline{x}_{VV}(j)} \right| + \left| \frac{\underline{y}_{HV}(j)}{\underline{y}_{HH}(j)} - \frac{\underline{x}_{HV}(j)}{\underline{x}_{HH}(j)} \right| \right\}$$

$$(3.3)$$

$$= \frac{1}{|\underline{x}_{VV}(j)|} \frac{\underline{y}_{VV}(j)}{|\underline{y}_{VV}(j)|} \frac{\left| \underline{y}_{VV}(j)\underline{x}_{HH}(j) - \underline{y}_{HH}(j)\underline{x}_{VV}(j) \right|}{(\underline{y}_{VV}(j)\underline{x}_{VV}(j) - \underline{y}_{HH}(j)\underline{x}_{VV}(j))} + \frac{\underline{x}_{HV}(j)}{\underline{x}_{HH}^2(j)} \frac{\left(\frac{\underline{y}_{HV}(j)}{\underline{y}_{HH}(j)} - \frac{\underline{x}_{HV}(j)}{\underline{x}_{HH}(j)} \right)}{\left| \frac{\underline{y}_{HV}(j)}{\underline{y}_{HH}(j)} - \frac{\underline{x}_{HV}(j)}{\underline{x}_{HH}(j)} \right|}$$

$$(3.4)$$

$$\frac{\partial h_j}{\partial \underline{x}_{HV}(j)} = \frac{\partial}{\partial \underline{x}_{HV}(j)} \left\{ \left| \frac{\underline{y}_{HH}(j)}{\underline{y}_{VV}(j)} - \frac{\underline{x}_{HH}(j)}{\underline{x}_{VV}(j)} \right| + \left| \frac{\underline{y}_{HV}(j)}{\underline{y}_{VV}(j)} - \frac{\underline{x}_{HV}(j)}{\underline{x}_{VV}(j)} \right| + \left| \frac{\underline{y}_{HV}(j)}{\underline{y}_{HH}(j)} - \frac{\underline{x}_{HV}(j)}{\underline{x}_{HH}(j)} \right| \right\}$$

$$(3.5)$$

$$= \frac{1}{|\underline{x}_{VV}(j)|} \frac{\underline{y}_{VV}(j)}{|\underline{y}_{VV}(j)|} \frac{\left| \underline{y}_{VV}(j)\underline{x}_{HV}(j) - \underline{y}_{HV}(j)\underline{x}_{VV}(j) \right|}{(\underline{y}_{VV}(j)\underline{x}_{HV}(j) - \underline{y}_{HV}(j)\underline{x}_{VV}(j))}$$

$$(3.6)$$

$$+ \frac{1}{|\underline{x}_{HH}(j)|} \frac{\underline{y}_{HH}(j)}{|\underline{y}_{HH}(j)|} \frac{\left| \underline{y}_{HH}(j)\underline{x}_{HV}(j) - \underline{y}_{HV}(j)\underline{x}_{HH}(j) \right|}{(\underline{y}_{HH}(j)\underline{x}_{HV}(j) - \underline{y}_{HV}(j)\underline{x}_{HH}(j))}$$

$$(3.7)$$

$$\frac{\partial h_j}{\partial \underline{x}_{VV}(j)} = \frac{\partial}{\partial \underline{x}_{VV}(j)} \left\{ \left| \frac{\underline{y}_{HH}(j)}{\underline{y}_{VV}(j)} - \frac{\underline{x}_{HH}(j)}{\underline{x}_{VV}(j)} \right| + \left| \frac{\underline{y}_{HV}(j)}{\underline{y}_{VV}(j)} - \frac{\underline{x}_{HV}(j)}{\underline{x}_{VV}(j)} \right| + \left| \frac{\underline{y}_{HV}(j)}{\underline{y}_{HH}(j)} - \frac{\underline{x}_{HV}(j)}{\underline{x}_{HH}(j)} \right| \right\}$$

$$(3.8)$$

$$= \frac{\underline{x}_{HH}(j)}{\underline{x}_{VV}^2(j)} \frac{\left(\frac{\underline{y}_{HH}(j)}{\underline{y}_{VV}(j)} - \frac{\underline{x}_{HH}(j)}{\underline{x}_{VV}(j)} \right)}{\left| \frac{\underline{y}_{HH}(j)}{\underline{y}_{VV}(j)} - \frac{\underline{x}_{HH}(j)}{\underline{x}_{VV}(j)} \right|} + \frac{\underline{x}_{HV}(j)}{\underline{x}_{VV}^2(j)} \frac{\left(\frac{\underline{y}_{HV}(j)}{\underline{y}_{VV}(j)} - \frac{\underline{x}_{HV}(j)}{\underline{x}_{VV}(j)} \right)}{\left| \frac{\underline{y}_{HV}(j)}{\underline{y}_{VV}(j)} - \frac{\underline{x}_{HV}(j)}{\underline{x}_{VV}(j)} \right|}.$$

$$(3.9)$$

Therefore the Hessian $\underline{\underline{H}}_h$ is given by $\underline{\underline{H}}_h = \begin{bmatrix} \frac{\partial^2 h_j}{\partial \underline{x}_{HH}^2(j)} & \frac{\partial^2 h_j}{\partial \underline{x}_{HH}(j)\partial \underline{x}_{HV}(j)} & \frac{\partial^2 h_j}{\partial \underline{x}_{HH}(j)\partial \underline{x}_{VV}(j)} \\ \frac{\partial^2 h_j}{\partial \underline{x}_{HH}(j)\partial \underline{x}_{HV}(j)} & \frac{\partial^2 h_j}{\partial \underline{x}_{HV}^2(j)} & \frac{\partial^2 h_j}{\partial \underline{x}_{HV}(j)\partial \underline{x}_{VV}(j)} \\ \frac{\partial^2 h_j}{\partial \underline{x}_{HH}(j)\partial \underline{x}_{VV}(j)} & \frac{\partial^2 h_j}{\partial \underline{x}_{HV}(j)\partial \underline{x}_{VV}(j)} & \frac{\partial^2 h_j}{\partial \underline{x}_{VV}^2(j)} \end{bmatrix}$

where

$$\frac{\partial^2 h_j}{\partial \underline{x}_{HH}^2(j)} = \left(\frac{-2\underline{x}_{HV}(j)\left(\frac{\underline{y}_{HV}(j)}{\underline{y}_{HH}(j)} - \frac{\underline{x}_{HV}(j)}{\underline{x}_{HH}(j)}\right)}{\underline{x}_{HH}^3(j)\left|\frac{\underline{y}_{HV}(j)}{\underline{y}_{HH}(j)} - \frac{\underline{x}_{HV}(j)}{\underline{x}_{HH}(j)}\right|} \right) \tag{3.10}$$

$$\frac{\partial^2 h_j}{\partial \underline{x}_{HH}(j)\partial \underline{x}_{HV}(j)} = \left(\frac{\left(\frac{\underline{y}_{HV}(j)}{\underline{y}_{HH}(j)} - \frac{\underline{x}_{HV}(j)}{\underline{x}_{HH}(j)}\right)}{\underline{x}_{HH}^2(j)\left|\frac{\underline{y}_{HV}(j)}{\underline{y}_{HH}(j)} - \frac{\underline{x}_{HV}(j)}{\underline{x}_{HH}(j)}\right|} \right) \tag{3.11}$$

$$\frac{\partial^2 h_j}{\partial \underline{x}_{HH}(j)\partial \underline{x}_{VV}(j)} = \left(\frac{\left(\frac{\underline{y}_{HH}(j)}{\underline{y}_{VV}(j)} - \frac{\underline{x}_{HH}(j)}{\underline{x}_{VV}(j)}\right)}{\underline{x}_{VV}^2(j)\left|\frac{\underline{y}_{HH}(j)}{\underline{y}_{VV}(j)} - \frac{\underline{x}_{HH}(j)}{\underline{x}_{VV}(j)}\right|} \right) \tag{3.12}$$

$$\frac{\partial^2 h_j}{\partial \underline{x}_{HV}^2(j)} = 0 \tag{3.13}$$

$$\frac{\partial^2 h_j}{\partial \underline{x}_{HV}(j)\partial \underline{x}_{VV}(j)} = \left(\frac{\frac{\underline{y}_{HV}(j)}{\underline{y}_{VV}(j)} - \frac{\underline{x}_{HV}(j)}{\underline{x}_{VV}(j)}}{\underline{x}_{VV}^2(j)\left|\frac{\underline{y}_{HV}(j)}{\underline{y}_{VV}(j)} - \frac{\underline{x}_{HV}(j)}{\underline{x}_{VV}(j)}\right|} \right) \tag{3.14}$$

$$\frac{\partial^2 h_j}{\partial \underline{x}_{VV}^2(j)} = \left(\frac{2\underline{x}_{HH}(j)\left(\frac{\underline{y}_{HH}(j)}{\underline{y}_{VV}(j)} - \frac{\underline{x}_{HH}(j)}{\underline{x}_{VV}(j)}\right)}{\underline{x}_{VV}^3(j)\left|\frac{\underline{y}_{HH}(j)}{\underline{y}_{VV}(j)} - \frac{\underline{x}_{HH}(j)}{\underline{x}_{VV}(j)}\right|} - \frac{2\underline{x}_{HV}(j)\left(\frac{\underline{y}_{HV}(j)}{\underline{y}_{VV}(j)} - \frac{\underline{x}_{HV}(j)}{\underline{x}_{VV}(j)}\right)}{\underline{x}_{VV}^3(j)\left|\frac{\underline{y}_{HV}(j)}{\underline{y}_{VV}(j)} - \frac{\underline{x}_{HV}(j)}{\underline{x}_{VV}(j)}\right|} \right). \tag{3.15}$$

Let $\underline{f} = [f_1^H \ f_2^H \ f_3^H]^H \in \mathbb{C}^3$. Then $\underline{\underline{H}}_h \underline{f} = \begin{bmatrix} a & b & c \end{bmatrix}^H$ where

$$a = f_1\left(\frac{-2\underline{x}_{HV}(j)\left(\frac{\underline{y}_{HV}(j)}{\underline{y}_{HH}(j)} - \frac{\underline{x}_{HV}(j)}{\underline{x}_{HH}(j)}\right)}{\underline{x}_{HH}^3(j)\left|\frac{\underline{y}_{HV}(j)}{\underline{y}_{HH}(j)} - \frac{\underline{x}_{HV}(j)}{\underline{x}_{HH}(j)}\right|} \right) + f_2\left(\frac{\left(\frac{\underline{y}_{HV}(j)}{\underline{y}_{HH}(j)} - \frac{\underline{x}_{HV}(j)}{\underline{x}_{HH}(j)}\right)}{\underline{x}_{HH}^2(j)\left|\frac{\underline{y}_{HV}(j)}{\underline{y}_{HH}(j)} - \frac{\underline{x}_{HV}(j)}{\underline{x}_{HH}(j)}\right|} \right) \tag{3.16}$$

$$+ f_3\left(\frac{\left(\frac{\underline{y}_{HH}(j)}{\underline{y}_{HV}(j)} - \frac{\underline{x}_{HH}(j)}{\underline{x}_{VV}(j)}\right)}{\underline{x}_{VV}^2(j)\left|\frac{\underline{y}_{HH}(j)}{\underline{y}_{VV}(j)} - \frac{\underline{x}_{HH}(j)}{\underline{x}_{VV}(j)}\right|} \right)$$

$$b = f_1\left(\frac{\left(\frac{\underline{y}_{HV}(j)}{\underline{y}_{HH}(j)} - \frac{\underline{x}_{HV}(j)}{\underline{x}_{HH}(j)}\right)}{\underline{x}_{HH}^2(j)\left|\frac{\underline{y}_{HV}(j)}{\underline{y}_{HH}(j)} - \frac{\underline{x}_{HV}(j)}{\underline{x}_{HH}(j)}\right|} \right) + f_3\left(\frac{\frac{\underline{y}_{HV}(j)}{\underline{y}_{VV}(j)} - \frac{\underline{x}_{HV}(j)}{\underline{x}_{VV}(j)}}{\underline{x}_{VV}^2(j)\left|\frac{\underline{y}_{HV}(j)}{\underline{y}_{VV}(j)} - \frac{\underline{x}_{HV}(j)}{\underline{x}_{VV}(j)}\right|} \right) \tag{3.17}$$

$$c = f_1 \left(\frac{\left(\frac{\underline{\mathbf{y}}_{HH}(j)}{\underline{\mathbf{y}}_{VV}(j)} - \frac{\underline{\mathbf{x}}_{HH}(j)}{\underline{\mathbf{x}}_{VV}(j)} \right)}{\underline{\mathbf{x}}_{VV}^2(j) \left| \frac{\underline{\mathbf{y}}_{HH}(j)}{\underline{\mathbf{y}}_{VV}(j)} - \frac{\underline{\mathbf{x}}_{HH}(j)}{\underline{\mathbf{x}}_{VV}(j)} \right|} \right) + f_2 \left(\frac{\frac{\underline{\mathbf{y}}_{HV}(j)}{\underline{\mathbf{y}}_{VV}(j)} - \frac{\underline{\mathbf{x}}_{HV}(j)}{\underline{\mathbf{x}}_{VV}(j)}}{\underline{\mathbf{x}}_{VV}^2(j) \left| \frac{\underline{\mathbf{y}}_{HV}(j)}{\underline{\mathbf{y}}_{VV}(j)} - \frac{\underline{\mathbf{x}}_{HV}(j)}{\underline{\mathbf{x}}_{VV}(j)} \right|} \right) \tag{3.18}$$

$$+ f_3 \left(\frac{2\underline{\mathbf{x}}_{HH}(j) \left(\frac{\underline{\mathbf{y}}_{HH}(j)}{\underline{\mathbf{y}}_{VV}(j)} - \frac{\underline{\mathbf{x}}_{HH}(j)}{\underline{\mathbf{x}}_{VV}(j)} \right)}{\underline{\mathbf{x}}_{VV}^3(j) \left| \frac{\underline{\mathbf{y}}_{HH}(j)}{\underline{\mathbf{y}}_{VV}(j)} - \frac{\underline{\mathbf{x}}_{HH}(j)}{\underline{\mathbf{x}}_{VV}(j)} \right|} - \frac{2\underline{\mathbf{x}}_{HV}(j) \left(\frac{\underline{\mathbf{y}}_{HV}(j)}{\underline{\mathbf{y}}_{VV}(j)} - \frac{\underline{\mathbf{x}}_{HV}(j)}{\underline{\mathbf{x}}_{VV}(j)} \right)}{\underline{\mathbf{x}}_{VV}^3(j) \left| \frac{\underline{\mathbf{y}}_{HV}(j)}{\underline{\mathbf{y}}_{VV}(j)} - \frac{\underline{\mathbf{x}}_{HV}(j)}{\underline{\mathbf{x}}_{VV}(j)} \right|} \right).$$

Therefore $\underline{\mathbf{f}}^H \underline{\underline{\mathbf{H}}}_h \underline{\mathbf{f}} =$

$$f_1^H f_1 \left(\frac{-2\underline{\mathbf{x}}_{HV}(j) \left(\frac{\underline{\mathbf{y}}_{HV}(j)}{\underline{\mathbf{y}}_{HH}(j)} - \frac{\underline{\mathbf{x}}_{HV}(j)}{\underline{\mathbf{x}}_{HH}(j)} \right)}{\underline{\mathbf{x}}_{HH}(j)^3 \left| \frac{\underline{\mathbf{y}}_{HV}(j)}{\underline{\mathbf{y}}_{HH}(j)} - \frac{\underline{\mathbf{x}}_{HV}(j)}{\underline{\mathbf{x}}_{HH}(j)} \right|} \right) + f_1^H f_2 \left(\frac{\left(\frac{\underline{\mathbf{y}}_{HV}(j)}{\underline{\mathbf{y}}_{HH}(j)} - \frac{\underline{\mathbf{x}}_{HV}(j)}{\underline{\mathbf{x}}_{HH}(j)} \right)}{\underline{\mathbf{x}}_{HH}^2(j) \left| \frac{\underline{\mathbf{y}}_{HV}(j)}{\underline{\mathbf{y}}_{HH}(j)} - \frac{\underline{\mathbf{x}}_{HV}(j)}{\underline{\mathbf{x}}_{HH}(j)} \right|} \right) \tag{3.19}$$

$$+ f_1^H f_3 \left(\frac{\left(\frac{\underline{\mathbf{y}}_{HH}(j)}{\underline{\mathbf{y}}_{VV}(j)} - \frac{\underline{\mathbf{x}}_{HH}(j)}{\underline{\mathbf{x}}_{VV}(j)} \right)}{\underline{\mathbf{x}}_{VV}^2(j) \left| \frac{\underline{\mathbf{y}}_{HH}(j)}{\underline{\mathbf{y}}_{VV}(j)} - \frac{\underline{\mathbf{x}}_{HH}(j)}{\underline{\mathbf{x}}_{VV}(j)} \right|} \right) + f_2^H f_1 \left(\frac{\left(\frac{\underline{\mathbf{y}}_{HV}(j)}{\underline{\mathbf{y}}_{HH}(j)} - \frac{\underline{\mathbf{x}}_{HV}(j)}{\underline{\mathbf{x}}_{HH}(j)} \right)}{\underline{\mathbf{x}}_{HH}^2(j) \left| \frac{\underline{\mathbf{y}}_{HV}(j)}{\underline{\mathbf{y}}_{HH}(j)} - \frac{\underline{\mathbf{x}}_{HV}(j)}{\underline{\mathbf{x}}_{HH}(j)} \right|} \right)$$

$$+ f_2^H f_3 \left(\frac{\frac{\underline{\mathbf{y}}_{HV}(j)}{\underline{\mathbf{y}}_{VV}(j)} - \frac{\underline{\mathbf{x}}_{HV}(j)}{\underline{\mathbf{x}}_{VV}(j)}}{\underline{\mathbf{x}}_{VV}^2(j) \left| \frac{\underline{\mathbf{y}}_{HV}(j)}{\underline{\mathbf{y}}_{VV}(j)} - \frac{\underline{\mathbf{x}}_{HV}(j)}{\underline{\mathbf{x}}_{VV}(j)} \right|} \right) + f_3^H f_1 \left(\frac{\left(\frac{\underline{\mathbf{y}}_{HH}(j)}{\underline{\mathbf{y}}_{VV}(j)} - \frac{\underline{\mathbf{x}}_{HH}(j)}{\underline{\mathbf{x}}_{VV}(j)} \right)}{\underline{\mathbf{x}}_{VV}^2(j) \left| \frac{\underline{\mathbf{y}}_{HH}(j)}{\underline{\mathbf{y}}_{VV}(j)} - \frac{\underline{\mathbf{x}}_{HH}(j)}{\underline{\mathbf{x}}_{VV}(j)} \right|} \right)$$

$$+ f_3^H f_2 \left(\frac{\frac{\underline{\mathbf{y}}_{HV}(j)}{\underline{\mathbf{y}}_{VV}(j)} - \frac{\underline{\mathbf{x}}_{HV}(j)}{\underline{\mathbf{x}}_{VV}(j)}}{\underline{\mathbf{x}}_{VV}^2(j) \left| \frac{\underline{\mathbf{y}}_{HV}(j)}{\underline{\mathbf{y}}_{VV}(j)} - \frac{\underline{\mathbf{x}}_{HV}(j)}{\underline{\mathbf{x}}_{VV}(j)} \right|} \right)$$

$$+ f_3^H f_3 \left(\frac{2\underline{\mathbf{x}}_{HH}(j) \left(\frac{\underline{\mathbf{y}}_{HH}(j)}{\underline{\mathbf{y}}_{VV}(j)} - \frac{\underline{\mathbf{x}}_{HH}(j)}{\underline{\mathbf{x}}_{VV}(j)} \right)}{\underline{\mathbf{x}}_{VV}^3(j) \left| \frac{\underline{\mathbf{y}}_{HH}(j)}{\underline{\mathbf{y}}_{VV}(j)} - \frac{\underline{\mathbf{x}}_{HH}(j)}{\underline{\mathbf{x}}_{VV}(j)} \right|} - \frac{2\underline{\mathbf{x}}_{HV}(j) \left(\frac{\underline{\mathbf{y}}_{HV}(j)}{\underline{\mathbf{y}}_{VV}(j)} - \frac{\underline{\mathbf{x}}_{HV}(j)}{\underline{\mathbf{x}}_{VV}(j)} \right)}{\underline{\mathbf{x}}_{VV}^3(j) \left| \frac{\underline{\mathbf{y}}_{HV}(j)}{\underline{\mathbf{y}}_{VV}(j)} - \frac{\underline{\mathbf{x}}_{HV}(j)}{\underline{\mathbf{x}}_{VV}(j)} \right|} \right).$$

Equation (3.19) simplifies to

$$
\underline{f}^H \underline{\underline{H}}_h \underline{f} = f_1^H f_1 \left(\frac{-2\underline{x}_{HV}(j)\left(\frac{\underline{y}_{HV}(j)}{\underline{y}_{HH}(j)} - \frac{\underline{x}_{HV}(j)}{\underline{x}_{HH}(j)}\right)}{\underline{x}_{HH}^3(j)\left|\frac{\underline{y}_{HV}(j)}{\underline{y}_{HH}(j)} - \frac{\underline{x}_{HV}(j)}{\underline{x}_{HH}(j)}\right|} \right) \tag{3.20}
$$

$$
+ 2Re(f_1^H f_2)\left(\frac{\left(\frac{\underline{y}_{HV}(j)}{\underline{y}_{HH}(j)} - \frac{\underline{x}_{HV}(j)}{\underline{x}_{HH}(j)}\right)}{\underline{x}_{HH}^2(j)\left|\frac{\underline{y}_{HV}(j)}{\underline{y}_{HH}(j)} - \frac{\underline{x}_{HV}(j)}{\underline{x}_{HH}(j)}\right|} \right)
$$

$$
+ 2Re(f_1^H f_3)\left(\frac{\left(\frac{\underline{y}_{HH}(j)}{\underline{y}_{VV}(j)} - \frac{\underline{x}_{HH}(j)}{\underline{x}_{VV}(j)}\right)}{\underline{x}_{VV}^2(j)\left|\frac{\underline{y}_{HH}(j)}{\underline{y}_{VV}(j)} - \frac{\underline{x}_{HH}(j)}{\underline{x}_{VV}(j)}\right|} \right)
$$

$$
+ 2Re(f_3^H f_2)\left(\frac{\frac{\underline{y}_{HV}(j)}{\underline{y}_{VV}(j)} - \frac{\underline{x}_{HV}(j)}{\underline{x}_{VV}(j)}}{\underline{x}_{VV}^2(j)\left|\frac{\underline{y}_{HV}(j)}{\underline{y}_{VV}(j)} - \frac{\underline{x}_{HV}(j)}{\underline{x}_{VV}(j)}\right|} \right)
$$

$$
+ (f_3^H f_3)\left(\frac{2\underline{x}_{HH}(j)\left(\frac{\underline{y}_{HH}(j)}{\underline{y}_{VV}(j)} - \frac{\underline{x}_{HH}(j)}{\underline{x}_{VV}(j)}\right)}{\underline{x}_{VV}^3(j)\left|\frac{\underline{y}_{HH}(j)}{\underline{y}_{VV}(j)} - \frac{\underline{x}_{HH}(j)}{\underline{x}_{VV}(j)}\right|} - \frac{2\underline{x}_{HV}(j)\left(\frac{\underline{y}_{HV}(j)}{\underline{y}_{VV}(j)} - \frac{\underline{x}_{HV}(j)}{\underline{x}_{VV}(j)}\right)}{\underline{x}_{VV}^3(j)\left|\frac{\underline{y}_{HV}(j)}{\underline{y}_{VV}(j)} - \frac{\underline{x}_{HV}(j)}{\underline{x}_{VV}(j)}\right|} \right).
$$

At this point, it becomes difficult to make generalizations about the convexity of the function based on the definiteness of the Hessian. However, notice that h_j does have discontinuities whenever any components in $\underline{x}_i$ are zero, $i \in \{HH, VV\}$. Therefore, the domain of each image would certainly need restriction in some fashion to be convex. However, an argument can be made for local convexity of the function during optimization if an initial guess for each $\underline{x}_i$ is sufficiently close to the desired relative minimum point $\underline{x}_i^*$. Such an intital guess may be the received image $\underline{y}_i$.

3.2 Convex Constraint for Polarimetric Data

Equivalently, polarization preservation occurs when the received phase history polarization ratios are equal to the enhanced scene reflectivity polarization ratios, i.e.,

$$
\frac{\underline{y}_{HH}(j)}{\underline{y}_{VV}(j)} = \frac{\underline{x}_{HH}(j)}{\underline{x}_{VV}(j)}, \qquad \frac{\underline{y}_{HV}(j)}{\underline{y}_{VV}(j)} = \frac{\underline{x}_{HV}(j)}{\underline{x}_{VV}(j)}, \qquad \frac{\underline{y}_{HV}(j)}{\underline{y}_{HH}(j)} = \frac{\underline{x}_{HV}(j)}{\underline{x}_{HH}(j)}. \tag{3.21}
$$

Cross-multiplication leads to another appropriate real-valued constraint given by

$$g_j = \left| \underline{y}_{HH}(j)\underline{x}_{VV}(j) - \underline{y}_{VV}(j)\underline{x}_{HH}(j) \right| + \left| \underline{y}_{HV}(j)\underline{x}_{VV}(j) - \underline{y}_{VV}(j)\underline{x}_{HV}(j) \right| \tag{3.22}$$
$$+ \left| \underline{y}_{HV}(j)\underline{x}_{HH}(j) - \underline{y}_{HH}(j)\underline{x}_{HV}(j) \right|.$$

Notice that each term within $g_j(\underline{x}_{HH}, \underline{x}_{HV}, \underline{x}_{VV})$ is a composition of two convex functions: the absolute value function and a linear function of the channels. Convexity is preserved under composition and addition, so it follows that g_j is convex [20]. To see this rigorously, consider the Hessian of $g_j(\underline{x}_{HH}, \underline{x}_{HV}, \underline{x}_{VV})$. The Lagrangian $\nabla g_j(\underline{x}_{HH}, \underline{x}_{HV}, \underline{x}_{VV})$ is

$$\nabla g_j(\underline{x}_{HH}, \underline{x}_{HV}, \underline{x}_{VV}) = \left[\frac{\partial g_j}{\partial \underline{x}_{HH}(j)} \quad \frac{\partial g_j}{\partial \underline{x}_{HV}(j)} \quad \frac{\partial g_j}{\partial \underline{x}_{VV}(j)} \right]^T, \tag{3.23}$$

where

$$\frac{\partial g_j(\underline{x}_{HH}, \underline{x}_{HV}, \underline{x}_{VV})}{\partial \underline{x}_{HH}(j)} = -\underline{y}_{VV}(j)\frac{\underline{y}_{HH}(j)\underline{x}_{VV}(j) - \underline{y}_{VV}(j)\underline{x}_{HH}(j)}{\left| \underline{y}_{HH}(j)\underline{x}_{VV}(j) - \underline{y}_{VV}(j)\underline{x}_{HH}(j) \right|} \tag{3.24}$$
$$+ \underline{y}_{HV}(j)\frac{\underline{y}_{HV}(j)\underline{x}_{HH}(j) - \underline{y}_{HH}(j)\underline{x}_{HV}(j)}{\left| \underline{y}_{HV}(j)\underline{x}_{HH}(j) - \underline{y}_{HH}(j)\underline{x}_{HV}(j) \right|}$$

$$\frac{\partial g_j(\underline{x}_{HH}, \underline{x}_{HV}, \underline{x}_{VV})}{\partial \underline{x}_{HV}(j)} = -\underline{y}_{VV}(j)\frac{\underline{y}_{HV}(j)\underline{x}_{VV}(j) - \underline{y}_{VV}(j)\underline{x}_{HV}(j)}{\left| \underline{y}_{HV}(j)\underline{x}_{VV}(j) - \underline{y}_{VV}(j)\underline{x}_{HV}(j) \right|} \tag{3.25}$$
$$- \underline{y}_{HH}(j)\frac{\underline{y}_{HV}(j)\underline{x}_{HH}(j) - \underline{y}_{HH}(j)\underline{x}_{HV}(j)}{\left| \underline{y}_{HV}(j)\underline{x}_{HH}(j) - \underline{y}_{HH}(j)\underline{x}_{HV}(j) \right|}$$

$$\frac{\partial g_j(\underline{x}_{HH}, \underline{x}_{HV}, \underline{x}_{VV})}{\partial \underline{x}_{VV}(j)} = \underline{y}_{HH}(j)\frac{\underline{y}_{HH}(j)\underline{x}_{VV}(j) - \underline{y}_{VV}(j)\underline{x}_{HH}(j)}{\left| \underline{y}_{HH}(j)\underline{x}_{VV}(j) - \underline{y}_{VV}(j)\underline{x}_{HH}(j) \right|} \tag{3.26}$$
$$+ \underline{y}_{HV}(j)\frac{\underline{y}_{HV}(j)\underline{x}_{VV}(j) - \underline{y}_{VV}(j)\underline{x}_{HV}(j)}{\left| \underline{y}_{HV}(j)\underline{x}_{VV}(j) - \underline{y}_{VV}(j)\underline{x}_{HV}(j) \right|}.$$

Notice that the fractional term of each partial derivative simplifies to ± 1, meaning each partial derivative is not explicitly a function of the corresponding partial term. Therefore the Hessian $\underline{\underline{H}}_g$ is given by

$$\underline{\underline{H}}_g = \begin{bmatrix} 0 & 0 & 0 \\ 0 & 0 & 0 \\ 0 & 0 & 0 \end{bmatrix}. \tag{3.27}$$

Clearly, $\underline{f}^H \underline{\underline{H}} \underline{f} = 0$ for all $\underline{f} \in \mathbb{R}^3$, which implies the Hessian is positive semidefinite.

3.3   Polarimetric Data

The joint image enhancement problem for polarimetric radar data can be phrased as

$$\min_{\underline{x}_{HH}, \underline{x}_{HV}, \underline{x}_{VV}} \left\| \underline{y}_{HH} - \underline{\underline{\Theta}} \underline{x}_{HH} \right\|_2^2 + \left\| \underline{y}_{HV} - \underline{\underline{\Theta}} \underline{x}_{HV} \right\|_2^2 + \left\| \underline{y}_{VV} - \underline{\underline{\Theta}} \underline{x}_{VV} \right\|_2^2$$

$$\text{subject to} \quad \begin{aligned} & \|\underline{x}_{HH}\|_1 \leq \alpha_1 \\ & \|\underline{x}_{HV}\|_1 \leq \alpha_2 \\ & \|\underline{x}_{VV}\|_1 \leq \alpha_3 \\ & p_j(\underline{x}_{HH}, \underline{x}_{HV}, \underline{x}_{VV}) \leq \tau, \end{aligned} \qquad (3.28)$$

where for small values of $\alpha_1, \alpha_2, \alpha_3$, sparse solutions are enforced and for small values of τ, interchannel relationships are preserved through the coupling constraint $p_j = \{h_j, g_j\}$ for each pixel j. Note that the last constraint in Eq. (3.28) could be an equality constraint, equal to zero, which would preserve interchannel coupling. However, the requirement is relaxed to allow for small error tolerance since the signals will be noisy. Moreover, notice that the same $\underline{\underline{\Theta}}$ and λ are assumed for each channel since all the channels are collected at the same time and therefore undergo the same data collection effects.

Using the method of Lagrange multipliers and assuming the Kuhn-Tucker conditions hold [20], the optimal solution satisfies

$$\nabla L = \underline{0}, \qquad (3.29)$$

where

$$L = L_1 + \beta_1 p_1(\underline{x}_{HH}^*, \underline{x}_{HV}^*, \underline{x}_{VV}^*) + \beta_2 p_2(\underline{x}_{HH}^*, \underline{x}_{HV}^*, \underline{x}_{VV}^*) + \cdots + \beta_N p_N(\underline{x}_{HH}^*, \underline{x}_{HV}^*, \underline{x}_{VV}^*), \quad (3.30)$$

$$L_1 = \left\| \underline{y}_{HH} - \underline{\underline{\Theta}} \underline{x}_{HH}^* \right\|_2^2 + \left\| \underline{y}_{HV} - \underline{\underline{\Theta}} \underline{x}_{HV}^* \right\|_2^2 + \left\| \underline{y}_{VV} - \underline{\underline{\Theta}} \underline{x}_{VV}^* \right\|_2^2 + \lambda\|\underline{x}_{HH}^*\|_1 + \lambda\|\underline{x}_{HV}^*\|_1 + \lambda\|\underline{x}_{VV}^*\|_1,$$
$$(3.31)$$

$\underline{x}_{HH}^*, \underline{x}_{HV}^*, \underline{x}_{VV}^*$ are the relative minimum points, λ is the Lagrange multiplier corresponding to the ℓ_1-norm constraint, and β_j is the Lagrange multiplier corresponding to the

polarization-preserving constraint $p_j(\underline{x}^*_{HH}, \underline{x}^*_{HV}, \underline{x}^*_{VV})$ for the jth pixel. Since there are $n = 3$ data channels and N pixels per channel, the gradient of the Lagrangian becomes

$$
\begin{bmatrix}
\frac{\partial}{\partial \underline{x}_{HH}} \\[6pt]
\frac{\partial}{\partial \underline{x}_{HV}} \\[6pt]
\frac{\partial}{\partial \underline{x}_{VV}} \\[6pt]
\frac{\partial}{\partial \lambda_1} \\[6pt]
\frac{\partial}{\partial \lambda_2} \\[6pt]
\frac{\partial}{\partial \lambda_3} \\[6pt]
\frac{\partial}{\partial \beta_1} \\[6pt]
\frac{\partial}{\partial \beta_2} \\[6pt]
\vdots \\[6pt]
\frac{\partial}{\partial \beta_N}
\end{bmatrix} L =
\begin{bmatrix}
2\underline{\underline{\Theta}}^H\underline{\underline{\Theta}}\underline{x}_{HH} - 2\underline{\underline{\Theta}}^H\underline{y}_{HH} + \lambda_1
\begin{bmatrix}
\frac{|\underline{x}_{HH}(1)|}{(|\underline{x}_{HH}(1)|^2+\epsilon)^{1/2}} \\
\vdots \\
\frac{|\underline{x}_{HH}(N)|}{(|\underline{x}_{HH}(N)|^2+\epsilon)^{1/2}}
\end{bmatrix}
+
\begin{bmatrix}
\frac{\beta_1 \partial p_1(\underline{x}_{HH},\underline{x}_{HV},\underline{x}_{VV})}{\partial \underline{x}_{HH}(1)} \\
\vdots \\
\frac{\beta_N \partial p_N(\underline{x}_{HH},\underline{x}_{HV},\underline{x}_{VV})}{\partial \underline{x}_{HH}(N)}
\end{bmatrix} \\[20pt]
2\underline{\underline{\Theta}}^H\underline{\underline{\Theta}}\underline{x}_{HV} - 2\underline{\underline{\Theta}}^H\underline{y}_{HV} + \lambda_2
\begin{bmatrix}
\frac{|\underline{x}_{HV}(1)|}{(|\underline{x}_{HV}(1)|^2+\epsilon)^{1/2}} \\
\vdots \\
\frac{|\underline{x}_{HV}(N)|}{(|\underline{x}_{HV}(N)|^2+\epsilon)^{1/2}}
\end{bmatrix}
+
\begin{bmatrix}
\frac{\beta_1 \partial p_1(\underline{x}_{HH},\underline{x}_{HV},\underline{x}_{VV})}{\partial \underline{x}_{HV}(1)} \\
\vdots \\
\frac{\beta_N \partial p_N(\underline{x}_{HH},\underline{x}_{HV},\underline{x}_{VV})}{\partial \underline{x}_{HV}(N)}
\end{bmatrix} \\[20pt]
2\underline{\underline{\Theta}}^H\underline{\underline{\Theta}}\underline{x}_{VV} - 2\underline{\underline{\Theta}}^H\underline{y}_{VV} + \lambda_3
\begin{bmatrix}
\frac{|\underline{x}_{VV}(1)|}{(|\underline{x}_{VV}(1)|^2+\epsilon)^{1/2}} \\
\vdots \\
\frac{|\underline{x}_{VV}(N)|}{(|\underline{x}_{VV}(N)|^2+\epsilon)^{1/2}}
\end{bmatrix}
+
\begin{bmatrix}
\frac{\beta_1 \partial p_1(\underline{x}_{HH},\underline{x}_{HV},\underline{x}_{VV})}{\partial \underline{x}_{VV}(1)} \\
\vdots \\
\frac{\beta_N \partial p_N(\underline{x}_{HH},\underline{x}_{HV},\underline{x}_{VV})}{\partial \underline{x}_{VV}(N)}
\end{bmatrix} \\[20pt]
\|\underline{x}_{HH}\|_1 \\[6pt]
\|\underline{x}_{HV}\|_1 \\[6pt]
\|\underline{x}_{VV}\|_1 \\[6pt]
p_1(\underline{x}_{HH},\underline{x}_{HV},\underline{x}_{VV}) \\[6pt]
p_2(\underline{x}_{HH},\underline{x}_{HV},\underline{x}_{VV}) \\[6pt]
\vdots \\[6pt]
p_N(\underline{x}_{HH},\underline{x}_{HV},\underline{x}_{VV})
\end{bmatrix}
\tag{3.32}
$$

where we have approximated the ℓ_1-norm as in [18].

Using the Local Duality Theorem, Eq. (3.28) can be converted to the equivalent dual problem

$$
\hat{\underline{x}}_{HH}, \hat{\underline{x}}_{HV}, \hat{\underline{x}}_{VV} = \arg \max_{\underline{\beta}} \; \arg \min_{\underline{x}_{HH},\underline{x}_{HV},\underline{x}_{VV}} L_1(\underline{x}_{HH},\underline{x}_{HV},\underline{x}_{VV}) + \underline{\beta}^T\underline{p}, \tag{3.33}
$$

where $\underline{\beta}$ is a vector such that $\underline{\beta}(j) = \beta_j$ and $\underline{p}(j) = p_j$.

3.4 Algorithmic Solution

To solve the polarimetric joint enhancement problem given in Eq. (3.33), we employ an iterative dual gradient method similar to the Dual Descent method described in Table (2.1) [5]. Moreover, we set the initial estimates of $\underline{x}_i$ as the corresponding $\underline{y}_i$. Other inputs include the desired sparsity weighting λ, data collection operator $\underline{\underline{\Theta}}$, $\underline{\beta}$ stepsize α, and other desired convergence parameters. Then, a double loop is initiated, where we alternate solving for the estimates $\hat{\underline{x}}_i$ and the Lagrange multiplier estimates $\hat{\underline{\beta}}$.

The image estimates $\hat{\underline{x}}_i$ remain fixed while solving for $\hat{\underline{\beta}}$. Specifically, the $\hat{\underline{\beta}}$ update equation for the kth iterate is

$$\hat{\underline{\beta}}^k = \hat{\underline{\beta}}^{k-1} + \alpha \underline{p}^{k-1}, \tag{3.34}$$

where $\underline{p}^{k-1}$ is the set of constraint functions based on the $(k-1)^{th}$ image estimates, $\hat{\underline{x}}_{HH}^{k-1}, \hat{\underline{x}}_{HV}^{k-1}, \hat{\underline{x}}_{VV}^{k-1}$. Then each entry $\hat{\beta}_j^k$ in $\hat{\underline{\beta}}^k$ is scaled by the received signal strength s_j given by

$$s_j = (\underline{y}_{HH}^2(j) + 2\underline{y}_{HV}^2(j) + \underline{y}_{VV}^2(j)), \tag{3.35}$$

in order to emphasize preservation on regions of the scene where received signal strength is larger. Next, the $\hat{\underline{\beta}}^k$ remain constant while solving for the image estimates $\hat{\underline{x}}_i^k$. Specifically, a preconditioned conjugate gradient method with a quadratic surrogate function is used, as in [16]. Chapter 4 demonstrates the suitability of this algorithm, considering both the non-convex constraint $p_j = h_j$ and the convex constraint $p_j = g_j$.

IV. Results

This research considers optimization constraints to preserve coupling between multiple polarization channels of radar data collected for the same scene of interest. For a given resolution cell or pixel j, scattering types are preserved through the non-convex constraint

$$h_j(\underline{x}_{HH}, \underline{x}_{HV}, \underline{x}_{VV}) = \left| \frac{\underline{y}_{HH}(j)}{\underline{y}_{VV}(j)} - \frac{\underline{x}_{HH}(j)}{\underline{x}_{VV}(j)} \right| + \left| \frac{\underline{y}_{HV}(j)}{\underline{y}_{VV}(j)} - \frac{\underline{x}_{HV}(j)}{\underline{x}_{VV}(j)} \right| + \left| \frac{\underline{y}_{HV}(j)}{\underline{y}_{HH}(j)} - \frac{\underline{x}_{HV}(j)}{\underline{x}_{HH}(j)} \right|, \quad (4.1)$$

or the convex constraint

$$g_j(\underline{x}_{HH}, \underline{x}_{HV}, \underline{x}_{VV}) = \left| \underline{y}_{HH}(j)\underline{x}_{VV}(j) - \underline{y}_{VV}(j)\underline{x}_{HH}(j) \right| + \left| \underline{y}_{HV}(j)\underline{x}_{VV}(j) - \underline{y}_{VV}(j)\underline{x}_{HV}(j) \right|$$
$$+ \left| \underline{y}_{HV}(j)\underline{x}_{HH}(j) - \underline{y}_{HH}(j)\underline{x}_{HV}(j) \right|. \quad (4.2)$$

In this section, the joint optimization problem in Section 3.4 is solved using the algorithm described in Section 3.5 for both the convex and non-convex coupling constraints. Polarimetric SAR datasets of several canonical scatterers [10] are considered. Jointly enhanced images are compared with corresponding images found through independent enhancement. Specifically, the objective function is broken down and individual costs are considered to demonstrate fidelity of signal estimates as well as preservation of polarimetric channel coupling. Moreover, a scattering measure of success is derived and compared for the enhanced images.

4.1 Measures of Error

Recall that the optimization objective function L is given by

$$L = \left\| \underline{y}_{HH} - \underline{\underline{\Theta}} \underline{x}_{HH} \right\|_2^2 + \left\| \underline{y}_{HV} - \underline{\underline{\Theta}} \underline{x}_{HV} \right\|_2^2 + \left\| \underline{y}_{VV} - \underline{\underline{\Theta}} \underline{x}_{VV} \right\|_2^2 + \lambda_1 \|\underline{x}_{HH}\|_1 + \lambda_2 \|\underline{x}_{HV}\|_1 + \lambda_3 \|\underline{x}_{VV}\|_1$$
$$+ \beta_1 p_1(\underline{x}_{HH}, \underline{x}_{HV}, \underline{x}_{VV}) + \beta_2 p_2(\underline{x}_{HH}, \underline{x}_{HV}, \underline{x}_{VV}) + \cdots + \beta_N p_N(\underline{x}_{HH}, \underline{x}_{HV}, \underline{x}_{VV}), \quad (4.3)$$

where $p_j(\underline{x}_{HH}, \underline{x}_{HV}, \underline{x}_{VV})$ is either the convex constraint g_j or the non-convex constraint h_j. The individual costs of sparsity, error of signal estimates, and error of polarimetric preser-

vation are considered and are determined from the respective terms of *L*. Additionally, the error of scattering classification is derived from the Pauli basis decomposition.

4.1.1 *Objective Function.*

Signal fidelity indicates the accuracy of the signal estimate. The error due to loss of signal fidelity for a particular estimate $\hat{\underline{x}}_i, i \in \{HH, HV, VV\}$ is given by the 2-norm cost

$$\|\underline{y}_i - \underline{\underline{\Theta}}\hat{\underline{x}}_i\|_2^2. \tag{4.4}$$

The amount of sparsity present in a signal estimate $\hat{\underline{x}}_i$ is given by the 1-norm cost

$$\|\hat{\underline{x}}_i\|_1. \tag{4.5}$$

The error due to loss of polarimetric preservation is calculated using the cost of the polarimetric coupling constraint. Hence, when h_j was enforced during optimization, the error cost is given by $h_j(\hat{\underline{x}}_{HH}, \hat{\underline{x}}_{HV}, \hat{\underline{x}}_{VV})$, and similarly for g_j.

4.1.2 *Scattering Measure.*

Preservation of the scattering matrix is important, particularly for target classification efforts. Along with demonstrating that the objective function is effectively enforced, the classification of the enhanced images is considered. Forming an image from the Pauli basis decomposition creates a RBG vector $\underline{c} = [R\ G\ B]^T$ for each pixel, where high values of red correspond to strong odd bounce reflection, high values of green correspond to strong even bounce reflection, and strong values of blue correspond to high orthogonal reflection. If little to no returned signal is detected, $\underline{c}$ has values close to 0 and then the pixel is black. For clarity, off-target black pixels are recolored white. The classification error at a given pixel is given by

$$\|\hat{\underline{c}} - \underline{c}\|_2^2, \tag{4.6}$$

where $\hat{\underline{c}}$ is the RGB vector of the enhanced signal and $\underline{c}$ is the RBG vector of the ideal scattering matrix at that pixel.

33

4.1.3 Parameters.

This research considers the measures of error over several parameters, including sparsity level, noise level, and specific regions of the scene. In each case, error is averaged over 500 Monte Carlo noise simulations.

The value of the sparsity enforcing parameter λ ranges from $0.1 - 1.3$. As λ is increased, the level of sparsity enforced is increased. In [17], an algorithm is presented for determining the value of λ corresponding to the lowest objective function cost. For this research, an appropriate range of λ values was picked visually.

Furthermore, both datasets are simulated and therefore do not contain noise. White Gaussian noise (WGN) is added to the data at peak signal-to-noise Ratio (SNR) ranging from 20 dB to 50 dB, with 20 dB indicating a high noise environment and 50 dB indicating a low noise environment.

Moreover, measures of error were considered over specific regions of the scene. The *full scene* error is the error over the entire image. The *on-target* error is the error over image masks defined where the normalized span is at least 0.5 dB. Similarly, the *off-target* error is the error over image masks defined where the normalized span is lower than 0.5 dB, corresponding to all pixels not on-target. The *maximum pixel* error is the error at the pixel with the strongest scattered power.

4.2 Canonical Shapes

A complex target can be broken down into the known scattering responses of simple shapes, or canonical scatterers, as discussed in Section 2.2. To illustrate polarimetric preservation, we consider scenes containing odd, even, and diffuse bounce canonical shapes. Shape data is simulated over an azimuth extent of 20°, elevation of 30°, wavelength of 0.03m, center frequency of $f_c = 10e9$ Hz and bandwidth $B = 2.95e9$ Hz.
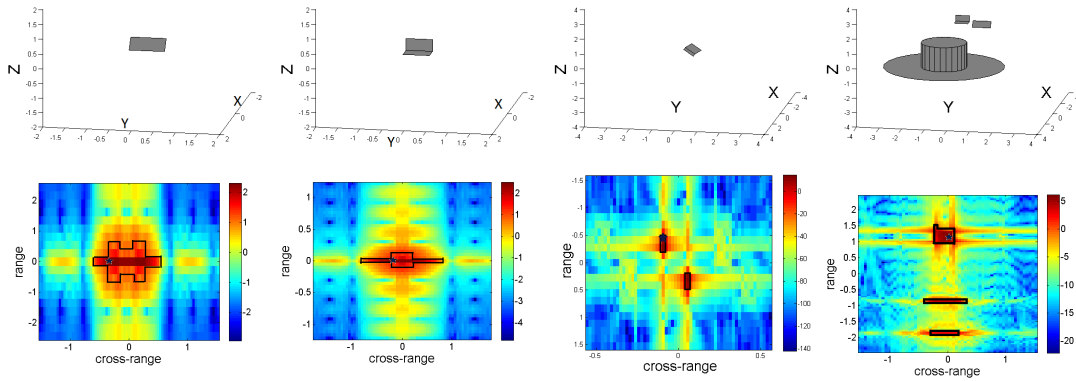
Figure 4.1: Top Row: The configuration for the plate, dihedral, titled dihedral, and group scenes. Second Row: The SPAN of the plate, dihedral, tilted dihedral and group scenes, along with regions of interest.

Polarization preservation imaging results are found for an individual plate, an individual standard dihedral, an individual tilted dihedral, and a group scene consisting of a plate, standard dihedral and top-hat. For clarity, the standard dihedral scene is called the 'dihedral scene', and the tilted dihedral scene is called the 'tilted dihedral scene.' To eliminate comparisons across RCS, the shape parameters are chosen such that the RCS is the same for each canonical shape. Figure 4.1 shows the scene setup and boxes in the on-target mask (black) and maximum pixel (star) for each scene. The off-target mask

Table 4.1: Canonical Shape Scene Parameters.

Parameters	Plate	Dihedral	Top-hat	Tilt-Dihedral
(x, y, z)	$(0, 0, 0)$ m	$(0, 0, 0)$ m	$(-1, -1, -1.5)$ m	$(0, 0, 0)$ m
L	0.8m	0.6m	-	0.6m
H	0.4243m	0.4m	1.6478m	0.4m
r	-	-	1m	-
RCS	1608.5 m^2	1608.5 m^2	1608.5 m^2	1608.5 m^2
Roll/Pitch/Yaw	30° pitch	-	-	45° pitch

contains all pixels outside the on-target mask. Table 4.1 lists the shape parameters for each canonical scene. It should be noted that the tilted dihedral has the same parameters as the dihedral along with a 45° pitch angle. Moreover, the group scene consists of a top-hat with parameters as listed as well as a plate at $(1, 1, 2)$ m and standard dihedral at $(0, 0, 2)$ m. All other plate and dihedral parameters are the same for the group scene.

Figures 4.2 - 4.5 show the $|S_{HH}|$, $|S_{HV}|$ and $|S_{VV}|$ signal responses for each scene at each stage of processing using 30 dB of WGN and $\lambda = 0.7$. The pure simulated images in the top row of each figure clearly show the impulse response smearing. Notice that due to the orientation of all the scatterers, tilted dihedral is the only object with significant response in the HV channel. The second row of each figure shows the images after adding noise at a moderate SNR of 30 dB. The third row in Figures 4.2-4.5 shows the results of independently enhancing each polarization channel under a sparsity constraint with $\lambda = 0.7$. The fourth row shows the results of jointly enhancing the polarimetric images using the non-convex constraint h_j. Finally, the fifth row shows the results of joint enhancement using the convex constraint g_j.

First consider noise level. Notice that in general the jointly restored images (both convex and non-convex) have reduced the noise better than the independently restored images; in the titled dihedral scene each enhancement type removes noise well. Next, consider signal restoration. In general, the independent images and non-convex jointly enhanced images produce similar results for the HH and VV channels; the convex jointly enhanced images appear to have preserved some high-level smearing close to the target, while decreasing the strength of the signal in the on-target region; this phenomena is most pronounced in the single shape cases, and less dramatic in the group scene. Moreover, in the dihedral case the non-convex constraint appears to have successfully restored some of
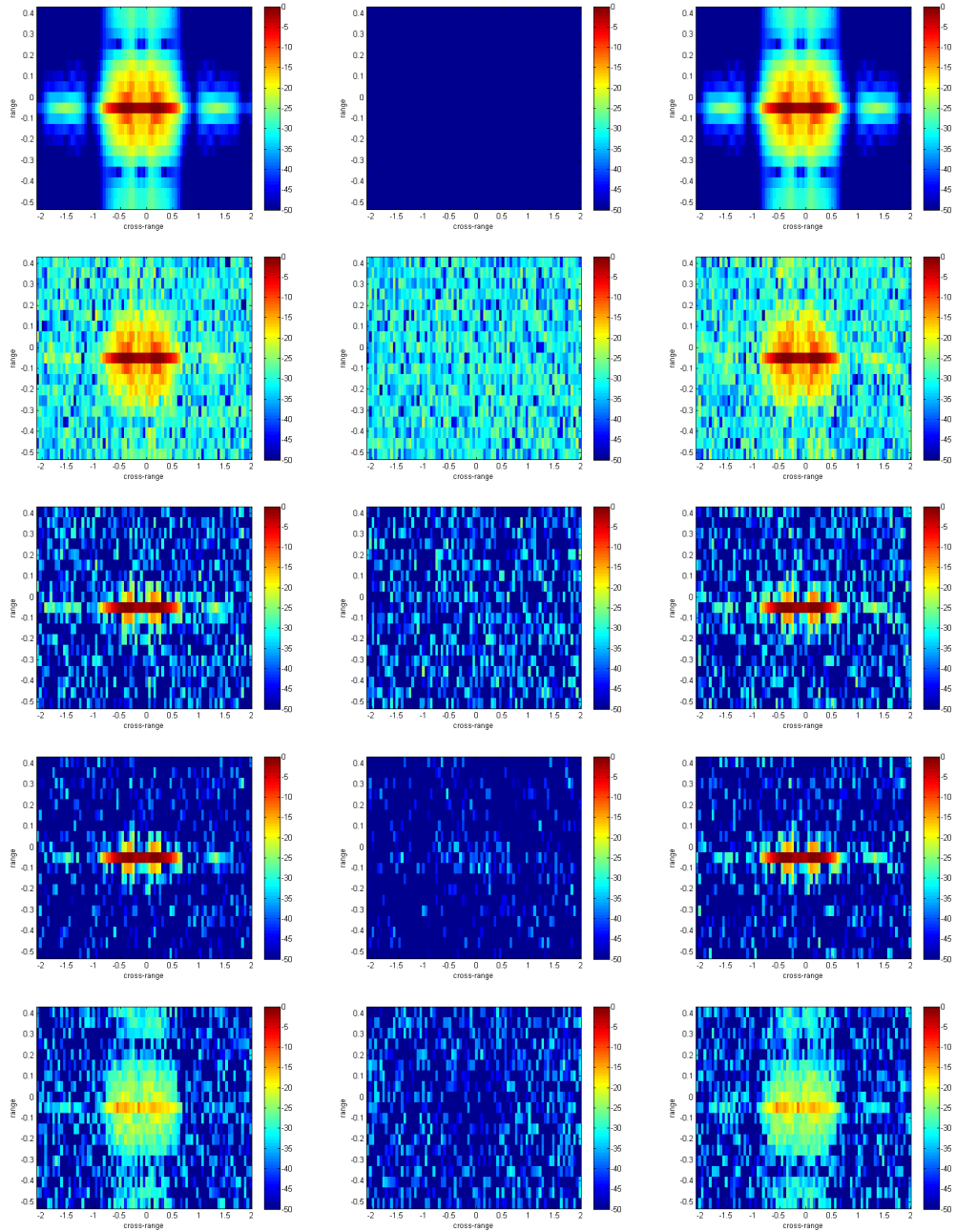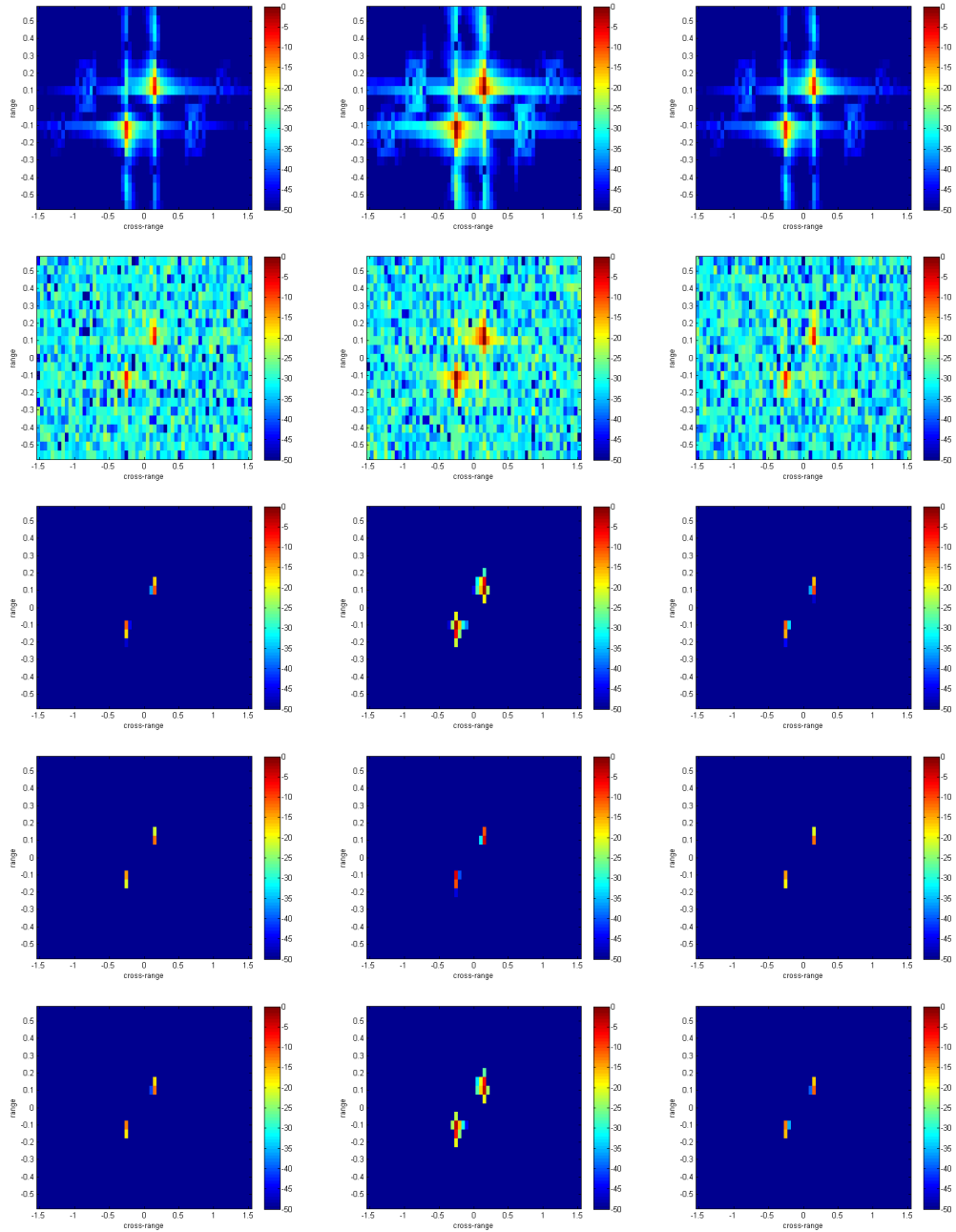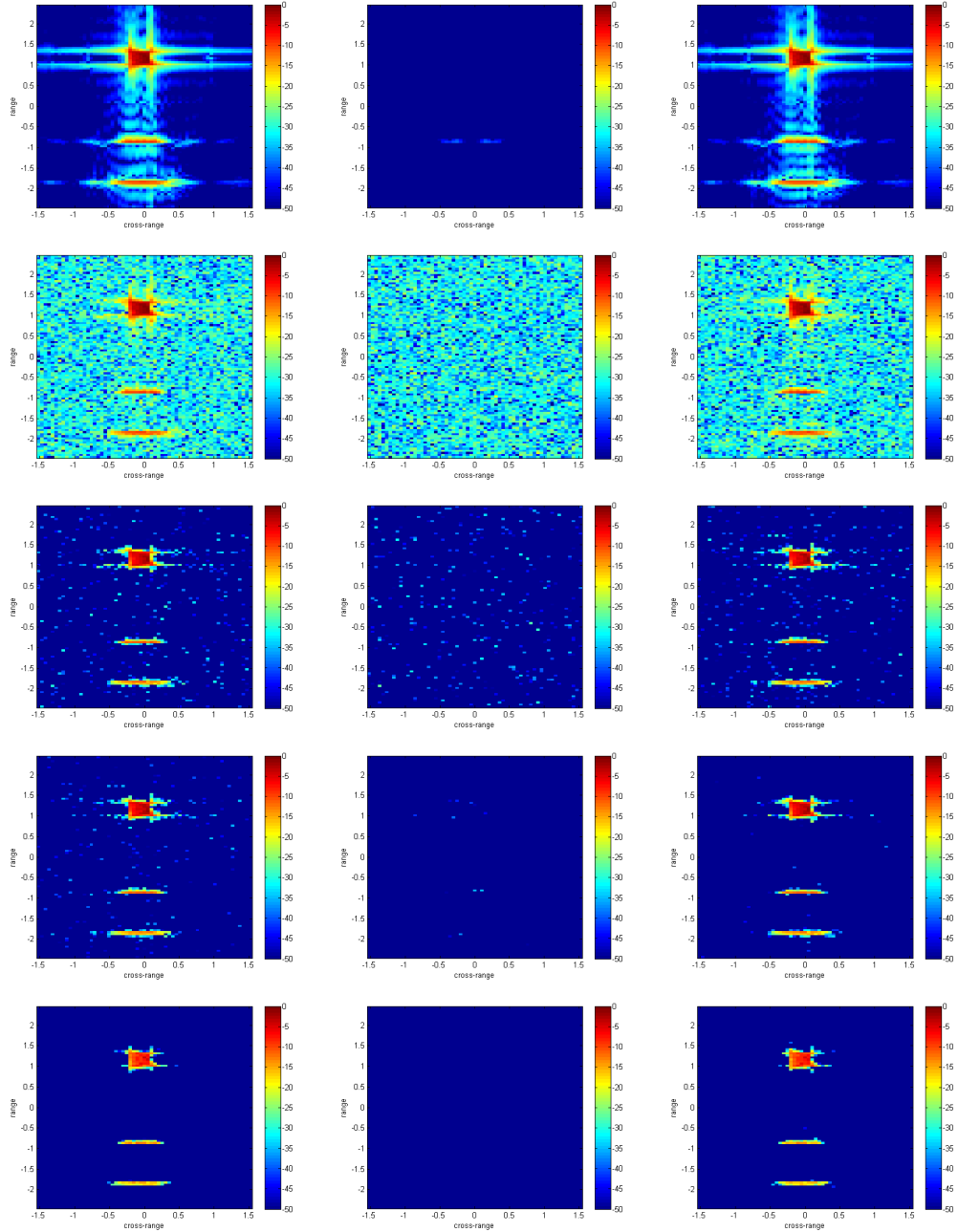
Figure 4.2: Plate scene images for all stages of enhancement. **Top Row:** Simulated $|S_{HH}|$, $|S_{HV}|$, and $|S_{VV}|$ with no added noise. **Second Row:** Simulated $|S_{HH}|$, $|S_{HV}|$, and $|S_{VV}|$ with 30 dB of WGN. **Third Row:** Independently restored $|S_{HH}|$, $|S_{HV}|$, and $|S_{VV}|$ with no polarimetric coupling constraint for $\lambda = 0.7$. **Fourth Row:** Jointly restored $|S_{HH}|$, $|S_{HV}|$, and $|S_{VV}|$ with non-convex coupling constraint for $\lambda = 0.7$. **Last Row:** Jointly restored $|S_{HH}|$, $|S_{HV}|$, and $|S_{VV}|$ with convex coupling constraint for $\lambda = 0.7$.

37
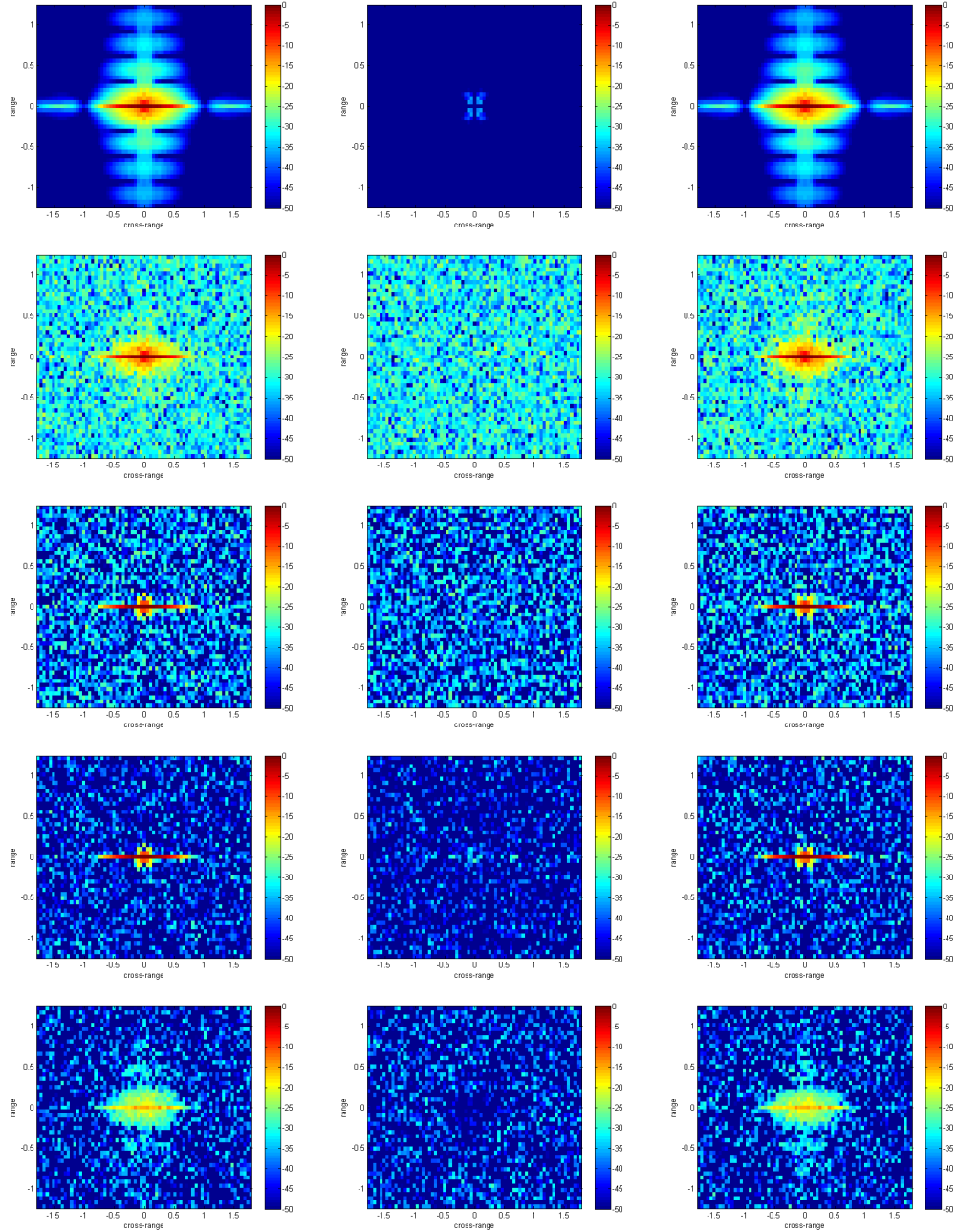
Figure 4.3: Dihedral scene images for all stages of enhancement.**Top Row:** Simulated $|S_{HH}|$, $|S_{HV}|$, and $|S_{VV}|$ with no added noise. **Second Row:** Simulated $|S_{HH}|$, $|S_{HV}|$, and $|S_{VV}|$ with 30 dB of WGN. **Third Row:** Independently restored $|S_{HH}|$, $|S_{HV}|$, and $|S_{VV}|$ with no polarimetric coupling constraint for $\lambda = 0.7$. **Fourth Row:** Jointly restored $|S_{HH}|$, $|S_{HV}|$, and $|S_{VV}|$ with non-convex coupling constraint for $\lambda = 0.7$. **Last Row:** Jointly restored $|S_{HH}|$, $|S_{HV}|$, and $|S_{VV}|$ with convex coupling constraint for $\lambda = 0.7$.

Figure 4.4: Tilted Dihedral scene images for all stages of enhancement. **Top Row:** Simulated $|S_{HH}|$, $|S_{HV}|$, and $|S_{VV}|$ with no added noise. **Second Row:** Simulated $|S_{HH}|$, $|S_{HV}|$, and $|S_{VV}|$ with 30 dB of WGN. **Third Row:** Independently restored $|S_{HH}|$, $|S_{HV}|$, and $|S_{VV}|$ with no polarimetric coupling constraint for $\lambda = 0.7$. **Fourth Row:** Jointly restored $|S_{HH}|$, $|S_{HV}|$, and $|S_{VV}|$ with non-convex coupling constraint for $\lambda = 0.7$. **Last Row:** Jointly restored $|S_{HH}|$, $|S_{HV}|$, and $|S_{VV}|$ with convex coupling constraint for $\lambda = 0.7$.

39

Figure 4.5: Group scene images for all stages of enhancement. **Top Row:** Simulated $|S_{HH}|$, $|S_{HV}|$, and $|S_{VV}|$ with no added noise. **Second Row:** Simulated $|S_{HH}|$, $|S_{HV}|$, and $|S_{VV}|$ with 30 dB of WGN. **Third Row:** Independently restored $|S_{HH}|$, $|S_{HV}|$, and $|S_{VV}|$ with no polarimetric coupling constraint for $\lambda = 0.7$. **Fourth Row:** Jointly restored $|S_{HH}|$, $|S_{HV}|$, and $|S_{VV}|$ with non-convex coupling constraint for $\lambda = 0.7$. **Last Row:** Jointly restored $|S_{HH}|$, $|S_{HV}|$, and $|S_{VV}|$ with convex coupling constraint for $\lambda = 0.7$.
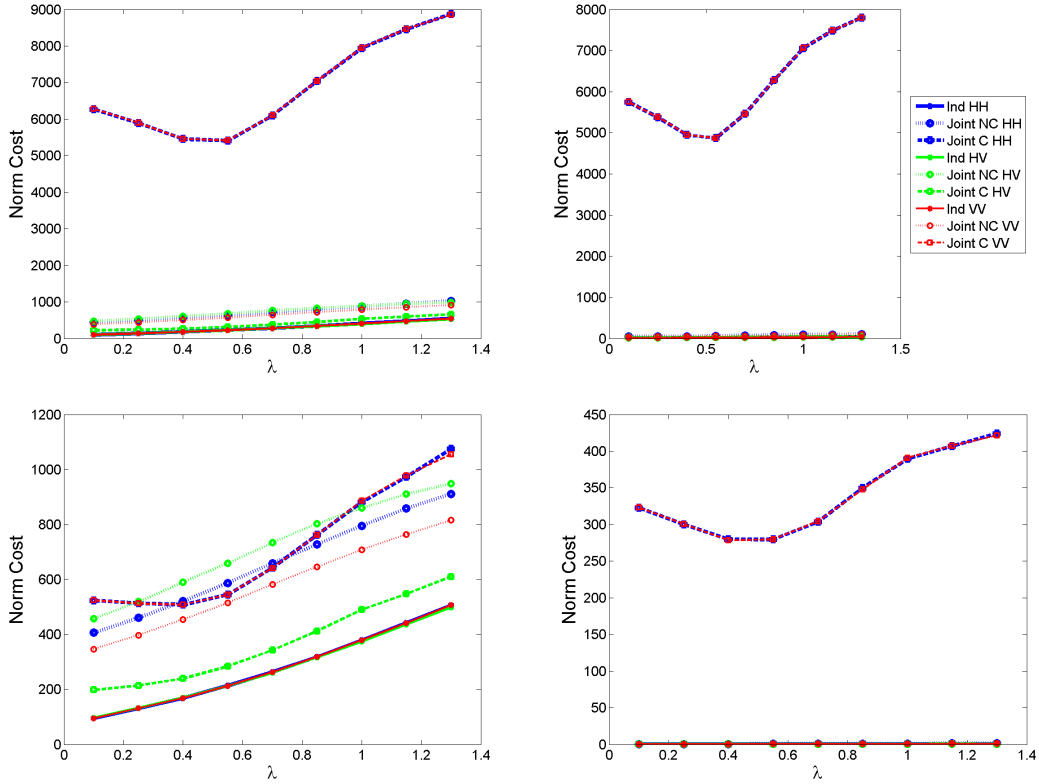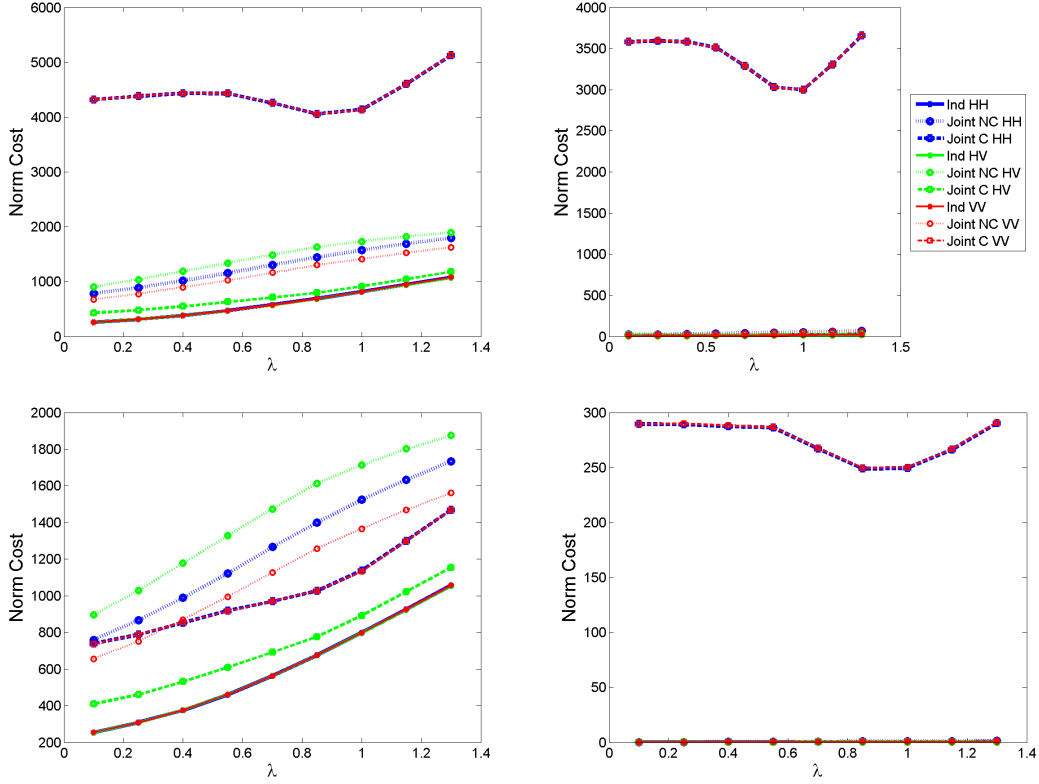
Figure 4.6: The 2-norm cost for the plate scene as a function of λ (SNR = 30 dB). The (**Top Left:**) Full scene error (**Top Right:**) On-Target Error (**Lower Left:**) Off-Target and (**Lower Right:**) Max Pixel cost of the 2-Norm for increasing λ (SNR = 30 dB).

the *HV* channel. However, for the group case the non-convex constraint appears to have added some *HV* response not present in the original images, which is undesirable. The tilted dihedral has good *HH*, *HV*, and *VV* response for all three enhancement types.

4.2.1 Signal Fidelity.

The error due to loss of signal fidelity is considered for each canonical scene over all the target regions for increasing values of λ and SNR. Figure 4.6 compares the 2-norm costs of the independently restored plate images with both the non-convex jointly restored plate images and the convex jointly restored plate images for increasing values of λ. Similarly, Figure 4.7 compares the 2-norm costs of the independently restored plate
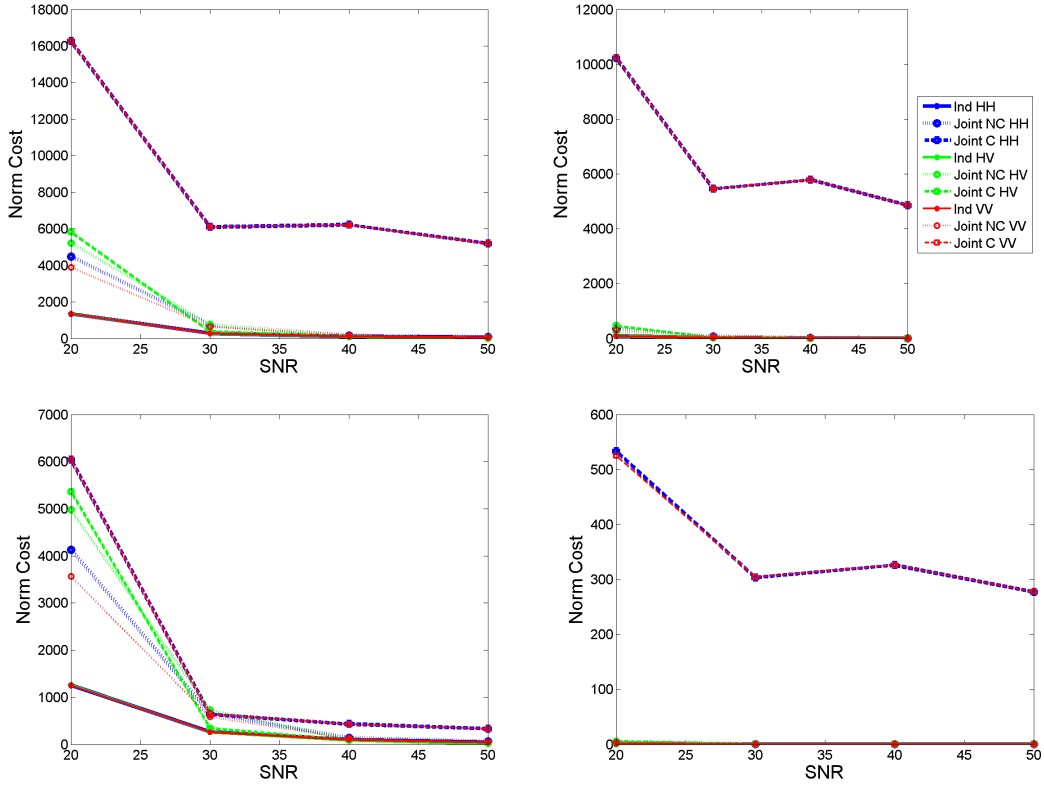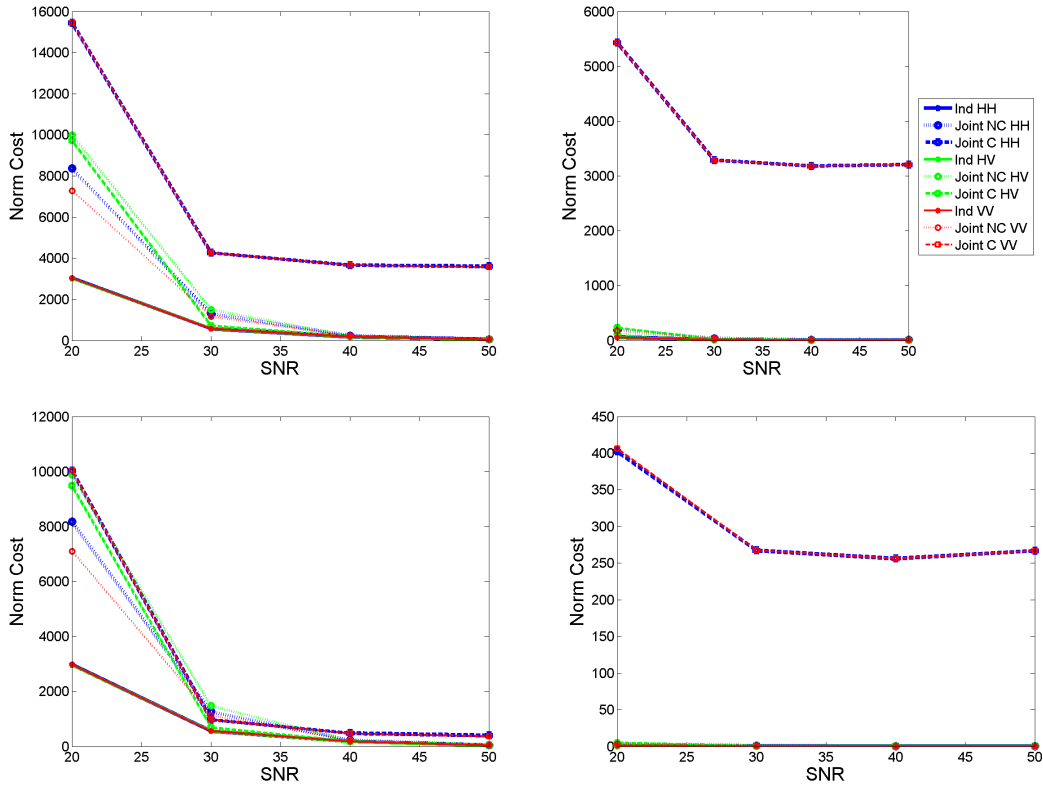
Figure 4.7: The 2-norm cost for the plate scene as a function of SNR ($\lambda = 0.7$). The (**Top Left:**) Full scene error (**Top Right:**) On-Target Error (**Lower Left:**) Off-Target and (**Lower Right:**) Max Pixel cost of the 2-Norm for increasing SNR ($\lambda = 0.7$).

images with the non-convex jointly restored plate images and the convex jointly restored plate images for increasing SNR. Notice that the 2-norm cost is considered individually for the *HH*, *HV* and *VV* channels. Moreover, note that in the graph legend Ind represents an independently enhanced channel, Joint C represents a convex jointly restored channel, and Joint NC represents a non-convex jointly restored channel. The subgraphs do not have the same scale. Figures 4.8-4.9, 4.10-4.11, and 4.12-4.13 show the corresponding images for the dihedral, tilted dihedral and group scenes, respectively.

First consider the independently restored images. For each scene, the independently restored images have a consistently lower full scene error cost in each channel compared to the jointly restored image channels. Furthermore, the on-target error of the independently
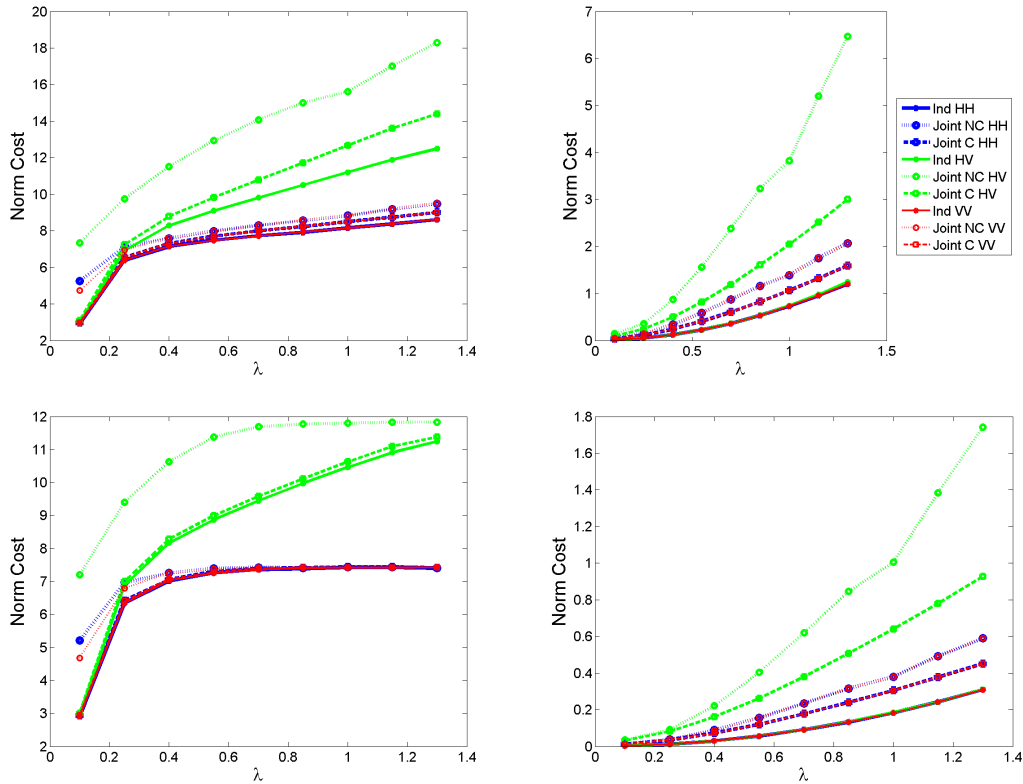
Figure 4.8: The 2-norm cost for the dihedral scene as a function of λ (SNR = 30 dB). The (**Top Left:**) Full scene error (**Top Right:**) On-Target Error (**Lower Left:**) Off-Target and (**Lower Right:**) Max Pixel cost of the 2-Norm for increasing λ (SNR = 30 dB).

enhanced channels is consistently lower than the corresponding off-target error. In the single shape scenes, the three independently restored channels have a similar on-target error magnitude. The three independently restored channels display on-target error magnitude differences when the number of scatterers increases. Specifically, the group scene displays a lower independently restored *HV* channel error compared to the *HH* and *VV* channels, which is attributable to the one region of low scattering response in the *HV* channel compared to the distinct regions of high scattering response in the *HH* and *VV* channels. Conversely, the tilted dihedral scene displays a higher full scene error in the independently restored *HV* channel versus the *HH* or *VV*. Upon inspection, the higher error in the *HV* channel comes from the off-target region and not the on-target region. In general, the
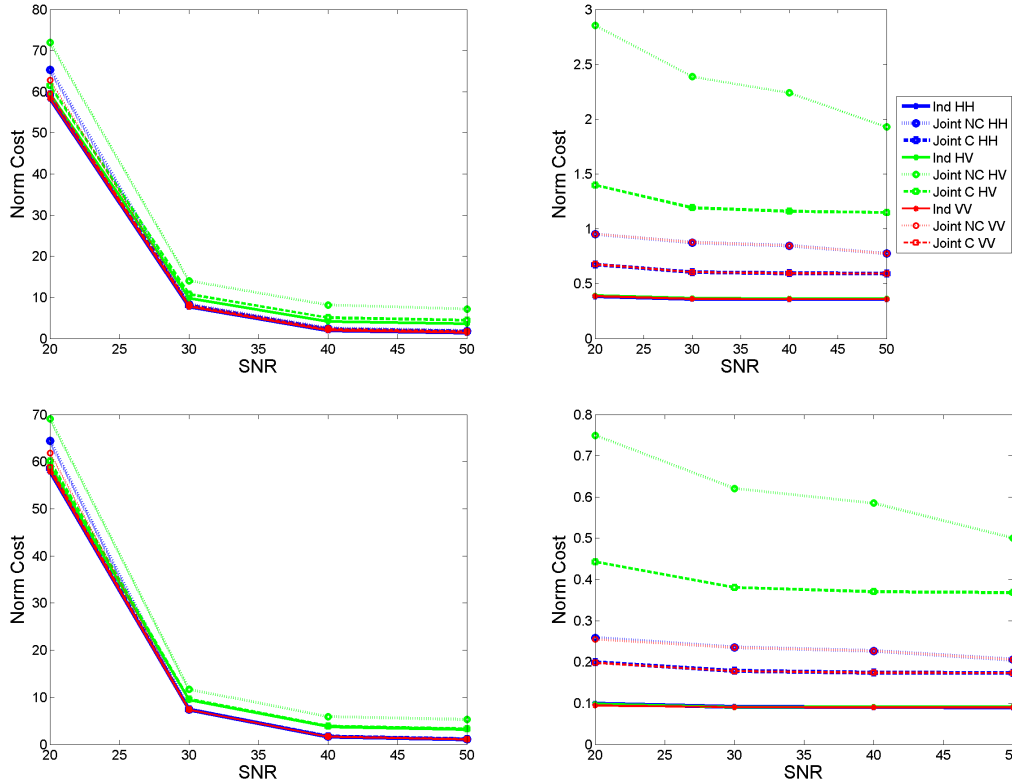
43

Figure 4.9: The 2-norm cost for the dihedral scene as a function of SNR ($\lambda = 0.7$). The (**Top Left:**) Full scene error (**Top Right:**) On-Target Error (**Lower Left:**) Off-Target and (**Lower Right:**) Max Pixel cost of the 2-Norm for increasing SNR ($\lambda = 0.7$).

2-norm cost steadily increases in each channel as λ increases and steadily decreases in each channel as SNR increases. These trends make sense; the signal fidelity and sparsity have a tradeoff. Thus higher penalties for sparsity lead to an increased error in signal fidelity. Moreover, as additive noise decreases the signal becomes easier to restore leading to decreased error in signal fidelity.

Next consider the non-convex jointly restored images. The non-convex jointly restored image channels consistently show the HV channel with the most full scene error, followed by the HH channel and then VV channel. For the plate and dihedral scenes, the three non-convex jointly restored channels have approximately the same error; in the tilted dihedral and group scene there is some difference between the HV channel and the other two

44

Figure 4.10: The 2-norm cost for the tilted dihedral scene as a function of λ (SNR = 30 dB). The (**Top Left:**) Full scene error (**Top Right:**) On-Target Error (**Lower Left:**) Off-Target and (**Lower Right:**) Max Pixel cost of the 2-Norm for increasing λ (SNR = 30 dB).

channels. Moreover, notice that the on-target error is significantly less than the off-target

error, which is desirable. In all scenes, the on-target non-convex jointly restored channels

have a similar level magnitude of error to the independent channels, particularly for small

λ. Moreover, notice that for the plate, dihedral and group scenes, the non-convex jointly

restored channels have less on-target error than the corresponding convex jointly restored

channels. However, in the tilted dihedral scenes the non-convex jointly restored channels

have a distinctly higher on-target error than the corresponding convex channels. Next,

notice that the non-convex jointly restored channels converge to the independently restored

channels as SNR increases. This is desirable, since the independent channels minimize

error in a no-noise environment, so it follows that the non-convex jointly restored channels
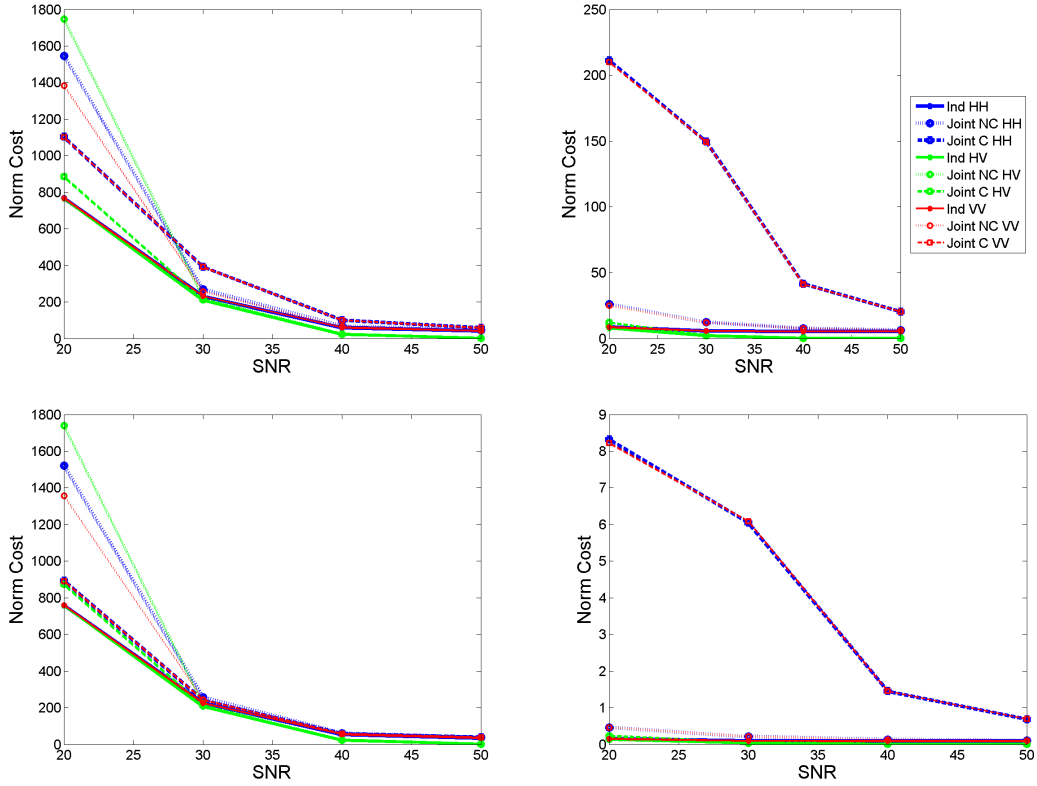
45

Figure 4.11: The 2-norm cost for the tilted dihedral scene as a function of SNR ($\lambda = 0.7$). The (**Top Left:**) Full scene error (**Top Right:**) On-Target Error (**Lower Left:**) Off-Target and (**Lower Right:**) Max Pixel cost of the 2-Norm for increasing SNR ($\lambda = 0.7$).

should converge to a similar solution. Overall, the non-convex jointly restored images display similar signal accuracy compared to the independent case.

Finally, consider the convex jointly restored image channels. The convex jointly restored channels consistently show the *HH* and *VV* channels with the same error and the *HV* channel with consistently lower error. Moreover, notice that in the plate and dihedral scenes, the full scene error of the convex jointly restored *HH* and *VV* channels is significantly higher than the corresponding full scene error in the independent and non-convex jointly restored channels. Looking closer, a significant portion of the convex jointly restored full scene error is due to on-target error, which is significantly higher than its off-target error. This trend is undesirable; the on-target regions of the scene are arguably
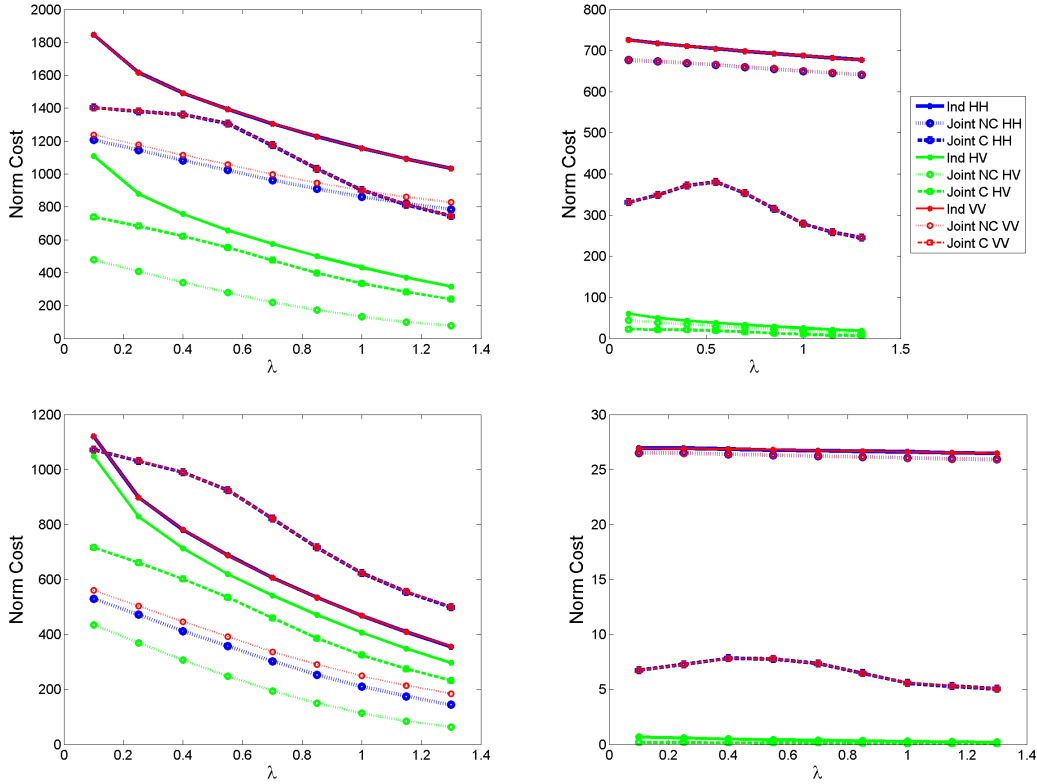
46
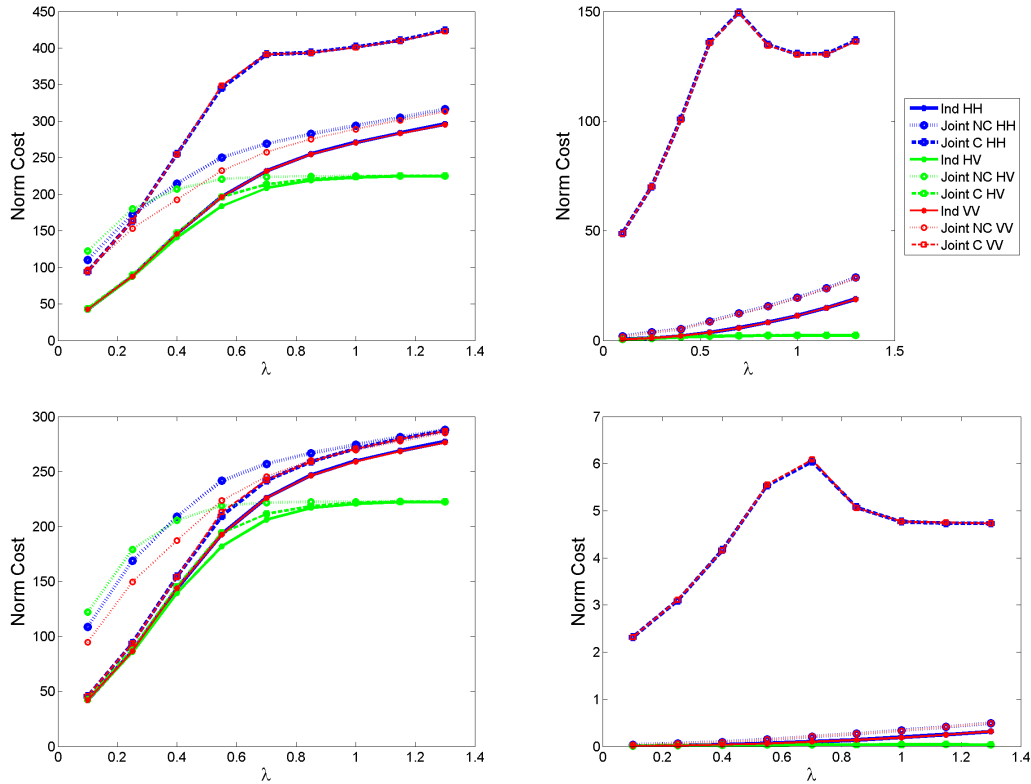
Figure 4.12: The 2-norm cost for the group scene as a function of λ (SNR = 30 dB). The (**Top Left:**) Full scene error (**Top Right:**) On-Target Error (**Lower Left:**) Off-Target and (**Lower Right:**) Max Pixel cost of the 2-Norm for increasing λ (SNR = 30 dB).

more important than the off-target regions. In the tilted dihedral scene, the convex jointly restored channels perform better in the on-target region than the off-target. Finally, notice that while all error types of the convex jointly restored channels do decrease with SNR, we do not see convergence to the corresponding independent channels.

Overall, the independently restored channels have a consistently lower 2-norm cost than the corresponding non-convex jointly restored channels and convex jointly restored channels. In the scenes with strong odd and even bounce scatterers, the *HV* channel has consistently lower 2-norm cost than the *HH* and *VV* channels for each enhancement type. Moreover, the non-convex jointly restored channels have a lower 2-norm cost compared to the convex jointly restored channels in the scenes with strong odd and even bounce
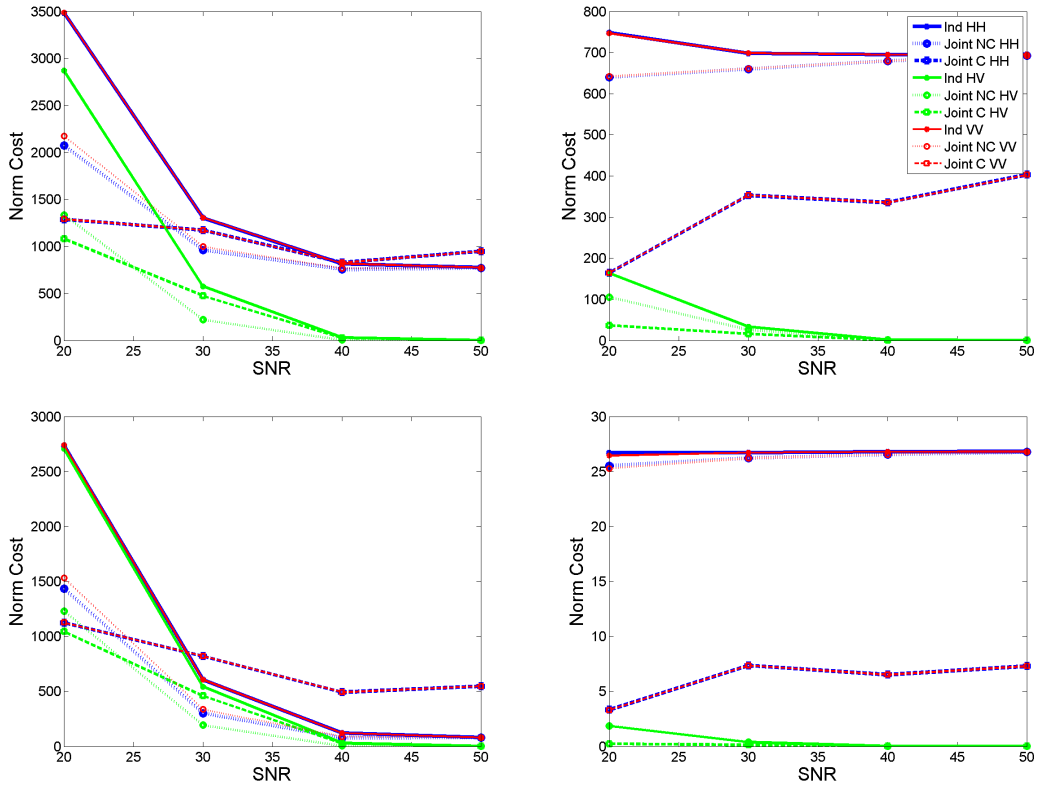
Figure 4.13: The 2-norm cost for the group scene as a function of SNR ($\lambda = 0.7$). The (**Top Left:**) Full scene error (**Top Right:**) On-Target Error (**Lower Left:**) Off-Target and (**Lower Right:**) Max Pixel cost of the 2-Norm for increasing SNR ($\lambda = 0.7$).

scattering. However, in the scenes with strong diffuse scattering the *HV* channel tends to have more error than the corresponding *HH* and *VV* channels, and we see a lower 2-norm cost in the convex jointly restored channels compared to the independently restored channels.

4.2.2 *Sparsity.*

The cost of the sparsity term is considered for each scene over increasing values of λ and SNR for various scene regions. Figure 4.14 compares the 1-norm cost of the independently restored plate images with both the non-convex jointly restored plate images and convex jointly restored plate images for increasing values of λ and various scene

48

Figure 4.14: The 1-norm cost for the plate scene as a function of λ (SNR = 30 dB). The (**Top Left:**) Full scene error (**Top Right:**) On-Target Error (**Lower Left:**) Off-Target and (**Lower Right:**) Max Pixel cost of the 1-Norm for increasing λ (SNR = 30 dB).

regions. Similarly, Figure 4.15 compares the 1-norm cost of the independently restored plate images with both the non-convex jointly restored plate images and convex jointly restored plate images for increasing SNR over various scene regions. Notice that the 1-norm cost is considered individually for the *HH*, *HV*, and *VV* channels. Figures 4.16-4.17, 4.18-4.19, and 4.20-4.21 show the corresponding images for the dihedral, tilted dihedral and group scenes, respectively.

First consider the independently restored channels. For each scene, and each scene region, the independently restored images have a higher 1-norm cost in each channel compared to the corresponding joint convex and joint non-convex channels. The exception is the off-target cost in the plate and dihedral scenes, where the convex jointly restored
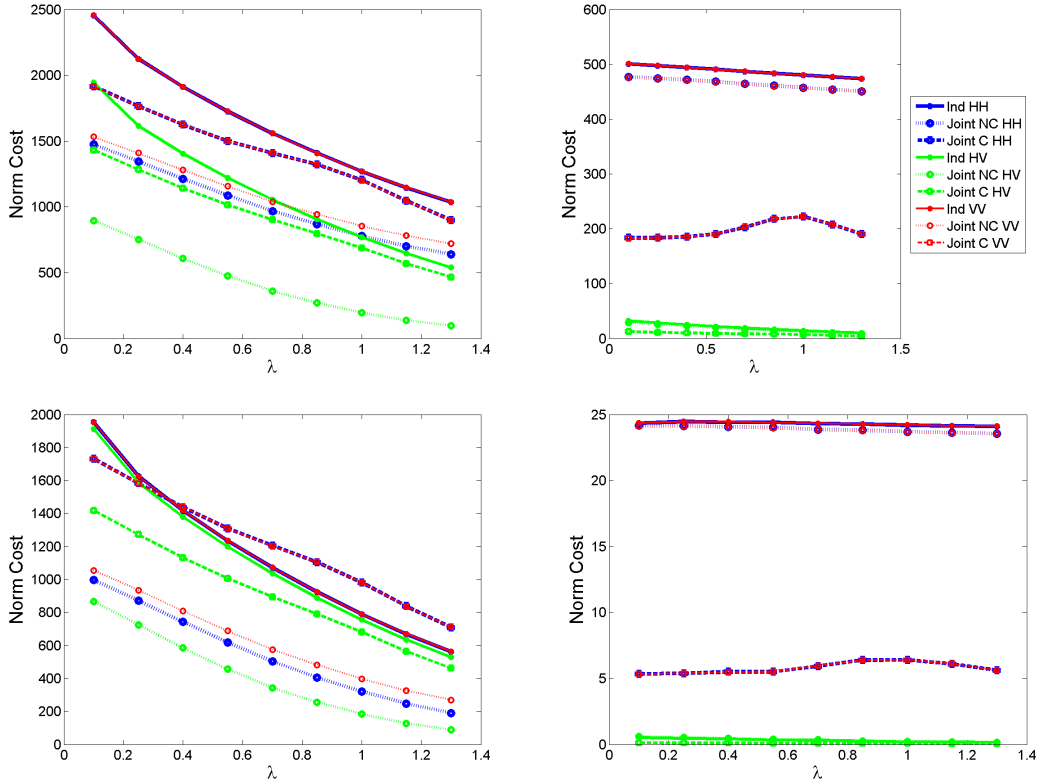
Figure 4.15: The 1-norm cost for the plate scene as a function of SNR ($\lambda = 0.7$). The (**Top Left:**) Full scene error (**Top Right:**) On-Target Error (**Lower Left:**) Off-Target and (**Lower Right:**) Max Pixel cost of the 1-Norm for increasing SNR ($\lambda = 0.7$).

images have a higher cost than the independent images. From Figures 4.2 - 4.5, it follows that the higher costs are due in part to the higher noise level in the independent images compared to the corresponding joint images, and in part to a stronger on-target signal. Furthermore, notice in plate, dihedral and group scenes, the independently restored images have a significantly higher signal response in the *HH* and *VV* channels compared to the *HV* channel, which leads to a consistently lower 1-norm cost for the *HV* channel compared to the *HH* and *VV* channels in all scene regions. In the tilted dihedral scene, where the *HV* channel has a strong signal response, the independently restored *HV* channel has a higher 1-norm cost than the *HH* and *VV* channels. Considering the average error per pixel indicates the independently restored images have a low cost average per pixel in the off-
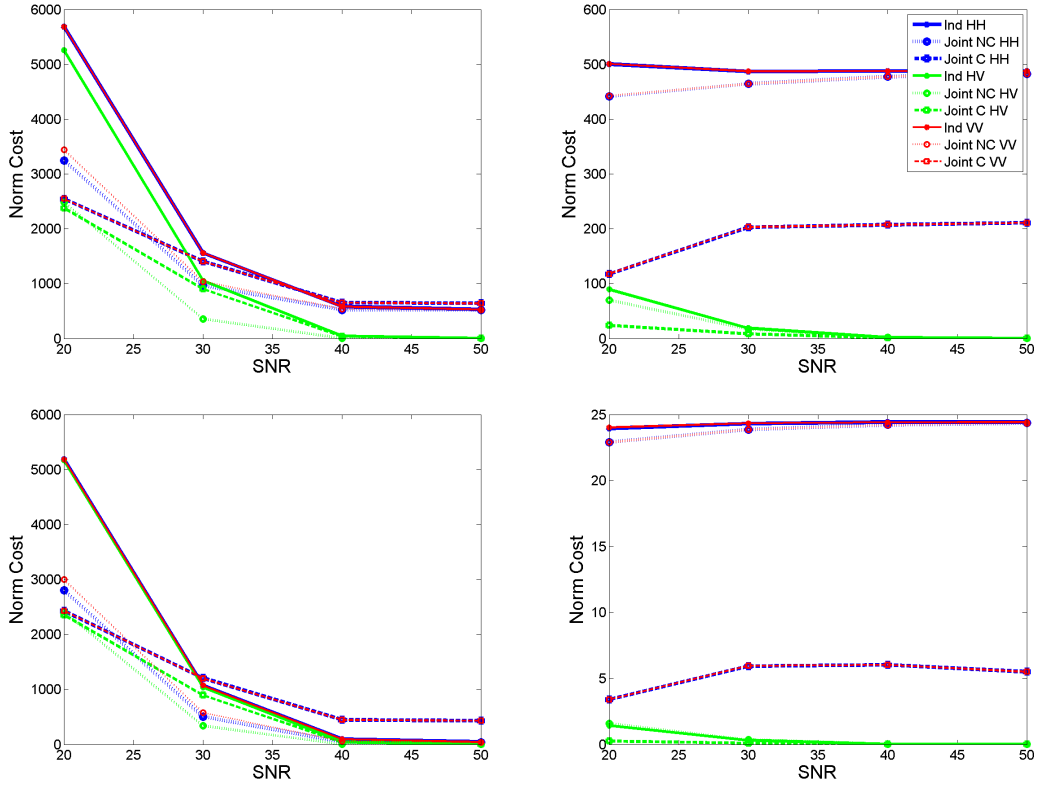
Figure 4.16: The 1-norm cost for the dihedral scene as a function of λ (SNR = 30 dB). The (**Top Left:**) Full scene error (**Top Right:**) On-Target Error (**Lower Left:**) Off-Target and (**Lower Right:**) Max Pixel cost of the 1-Norm for increasing λ (SNR = 30 dB).

target region, and a high average cost per pixel in the on-target region. Hence, the sparse pixels are picked primarily from the on-target region, which is desirable. Finally, notice that the 1-norm cost of the independent channels steadily decreases over λ and decreases over SNR, as expected.

Next consider the non-convex jointly restored images. The non-convex jointly restored channels display similar trends to the independent case; specifically, in the plate, dihedral and group scenes, the *HH* and *VV* channels have a consistently higher sparsity cost than the *HV* channel; in the tilted dihedral scene, the *HV* channel has a consistently higher cost. Moreover, the non-convex jointly restored channels converge to the sparsity level of the corresponding independent channels as SNR increases. Based on Figures 4.2-4.5, the
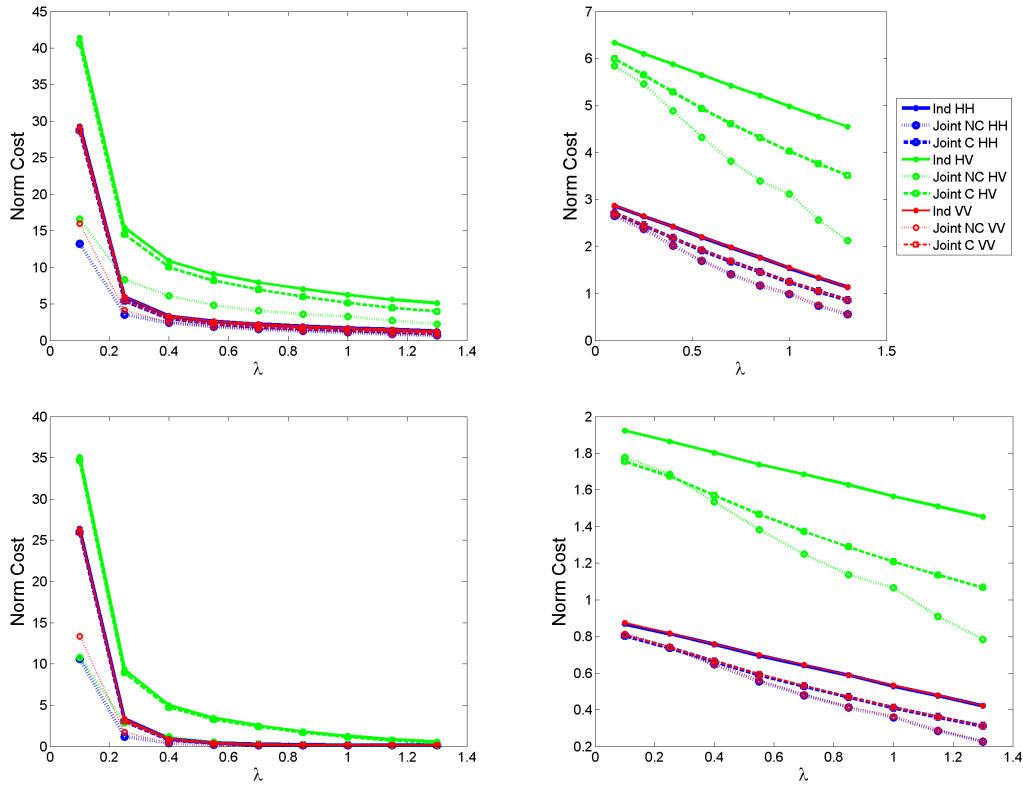
Figure 4.17: The 1-norm cost for the dihedral scene as a function of SNR ($\lambda = 0.7$). The (**Top Left:**) Full scene error (**Top Right:**) On-Target Error (**Lower Left:**) Off-Target and (**Lower Right:**) Max Pixel cost of the 1-Norm for increasing SNR ($\lambda = 0.7$).

independent and convex jointly restored images converge to a similar solution. Next, notice that the non-convex jointly restored images have a strong on-target signal and a low signal elsewhere, which manifests as a high average pixel 1-norm cost in the on-target region and a low average pixel 1-norm cost in the off target region, as desired.

Finally, consider the convex jointly restored images. The convex jointly restored channels display similar trends to the independent case; specifically, in the plate, dihedral and group scenes, the *HH* and *VV* channels have a consistently higher sparsity cost than the *HV* channel; in the tilted dihedral scene, the *HV* channel has a consistently higher cost. In the plate, dihedral, and group scenes, the convex jointly restored channels have a lower 1-norm cost average per pixel in the on-target region compared to the corresponding
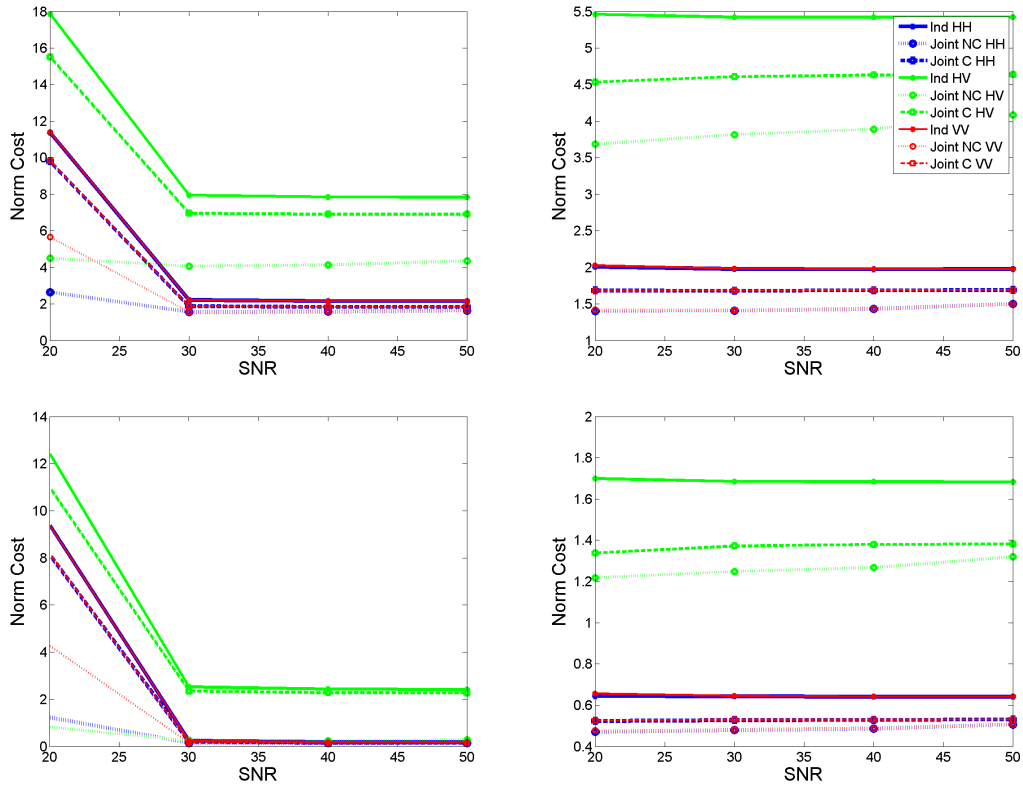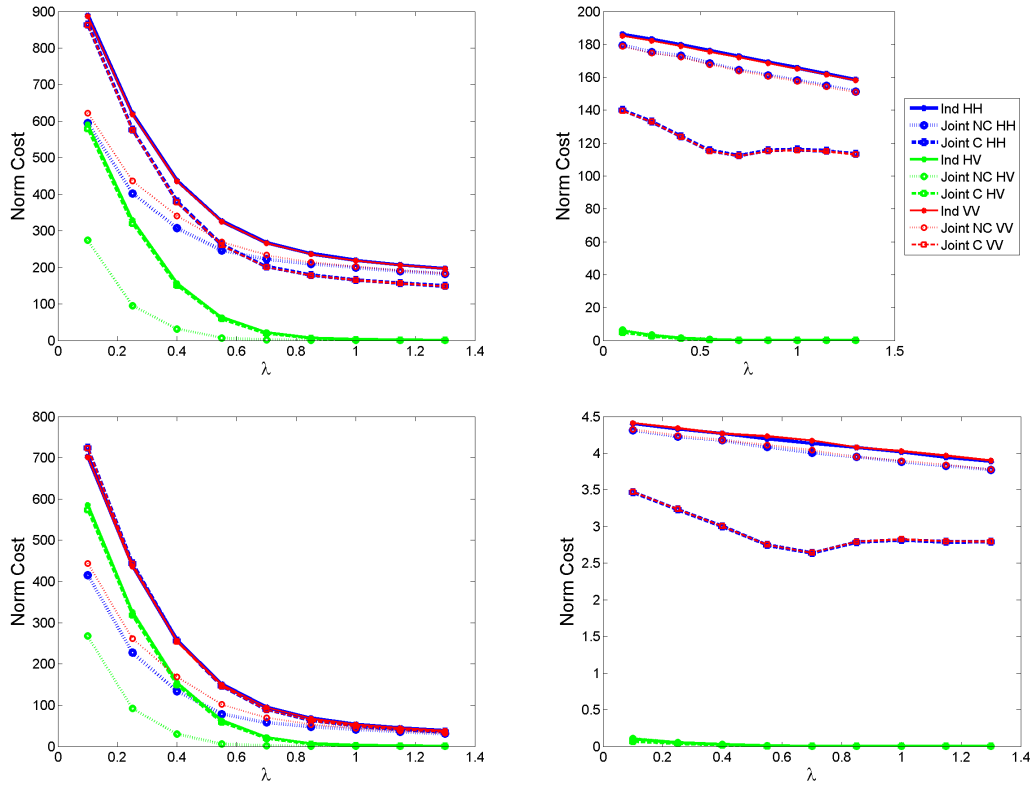
Figure 4.18: The 1-norm cost for the tilted dihedral scene as a function of λ (SNR = 30 dB). The (**Top Left:**) Full scene error (**Top Right:**) On-Target Error (**Lower Left:**) Off-Target and (**Lower Right:**) Max Pixel cost of the 1-Norm for increasing λ (SNR = 30 dB).

independent and non-convex jointly restored channels, and a higher 1-norm cost average per pixel in the off-target region. From Figures 4.2-4.5, its clear that the convex jointly restored images have a lower signal strength on-target, and have preserved some impulse response smearing off-target. In the titled dihedral scene, the convex jointly restored channels have a higher pixel average 1-norm cost on-target compared to the non-convex jointly restored channels.

Figure 4.19: The 1-norm cost for the tilted dihedral scene as a function of SNR ($\lambda = 0.7$). The (**Top Left:**) Full scene error (**Top Right:**) On-Target Error (**Lower Left:**) Off-Target and (**Lower Right:**) Max Pixel cost of the 1-Norm for increasing SNR ($\lambda = 0.7$).

Figure 4.20: The 1-norm cost for the group scene as a function of λ (SNR = 30 dB). The (**Top Left:**) Full scene error (**Top Right:**) On-Target Error (**Lower Left:**) Off-Target and (**Lower Right:**) Max Pixel cost of the 1-Norm for increasing λ (SNR = 30 dB).
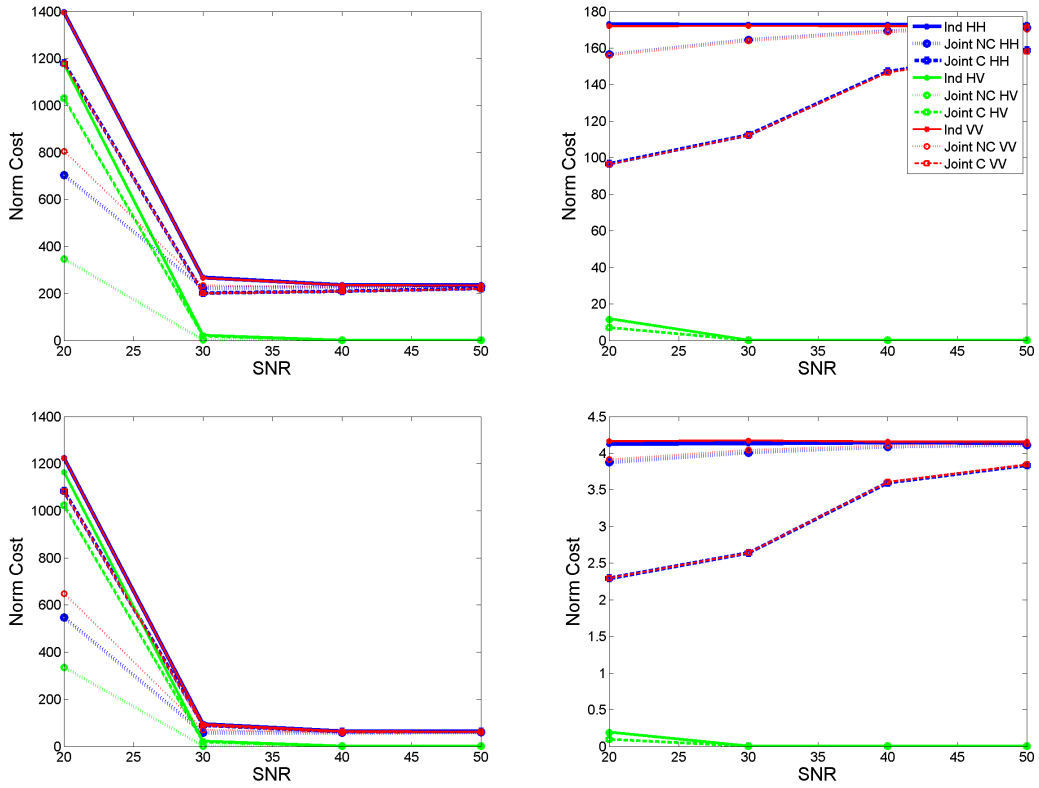
Figure 4.21: The 1-norm cost for the group scene as a function of SNR ($\lambda = 0.7$). The (**Top Left:**) Full scene error (**Top Right:**) On-Target Error (**Lower Left:**) Off-Target and (**Lower Right:**) Max Pixel cost of the 1-Norm for increasing SNR ($\lambda = 0.7$).

4.2.3 Polarimetric Preservation.

The error due to loss of polarimetric preservation is considered for each canonical shape over increasing values of λ and SNR for several scene regions. Figure 4.22 compares the polarimetric constraint cost of the independently restored plate images with both the non-convex jointly restored plate images and convex jointly restored plate images for increasing values of λ and various scene regions. Similarly, Figure 4.23 compares the polarimetric constraint cost of the independently restored plate images with both the non-convex jointly restored plate images and convex jointly restored plate images for increasing SNR over various scene regions. Notice that the polarimetric constraint cost is considered individually for the terms $\left|\frac{\underline{y}_{HH}(j)}{\underline{y}_{VV}(j)} - \frac{\underline{x}_{HH}(j)}{\underline{x}_{VV}(j)}\right|$, $\left|\frac{\underline{y}_{HV}(j)}{\underline{y}_{VV}(j)} - \frac{\underline{x}_{HV}(j)}{\underline{x}_{VV}(j)}\right|$, and $\left|\frac{\underline{y}_{HV}(j)}{\underline{y}_{HH}(j)} - \frac{\underline{x}_{HV}(j)}{\underline{x}_{HH}(j)}\right|$. Figures 4.24-4.25, 4.26-4.27, and 4.28-4.29 show the corresponding images for the dihedral, tilted dihedral and group scenes, respectively. Notice that among all figures, similar scattering in the *HH* and *VV* responses manifests itself as a similar error for the ratios $\left|\frac{\underline{y}_{HV}(j)}{\underline{y}_{VV}(j)} - \frac{\underline{x}_{HV}(j)}{\underline{x}_{VV}(j)}\right|$ and $\left|\frac{\underline{y}_{HV}(j)}{\underline{y}_{HH}(j)} - \frac{\underline{x}_{HV}(j)}{\underline{x}_{HH}(j)}\right|$.

First consider the independently restored image ratios. The independently restored polarimetric ratios have a high error compared to the corresponding jointly restored ratios for all scenes and scene regions. In the tilted dihedral scene, all preservation types appear to have similar levels of error in all scene regions. This improvement in the independently restored channels may be due to the similar signal strengths in each channel. In all scenes, the independently restored ratios have a high full scene error, the bulk of which comes from the off-target region. However, the independently restored on-target polarimetric ratio error is high compared to the corresponding jointly restored on-target polarimetric ratio error. For the plate and dihedral scenes, the independently restored image ratio error tends to increase as λ increases and decreases as SNR increases, as expected. However, for the tilted dihedral and group scenes, the full scene and off-target error of the independently
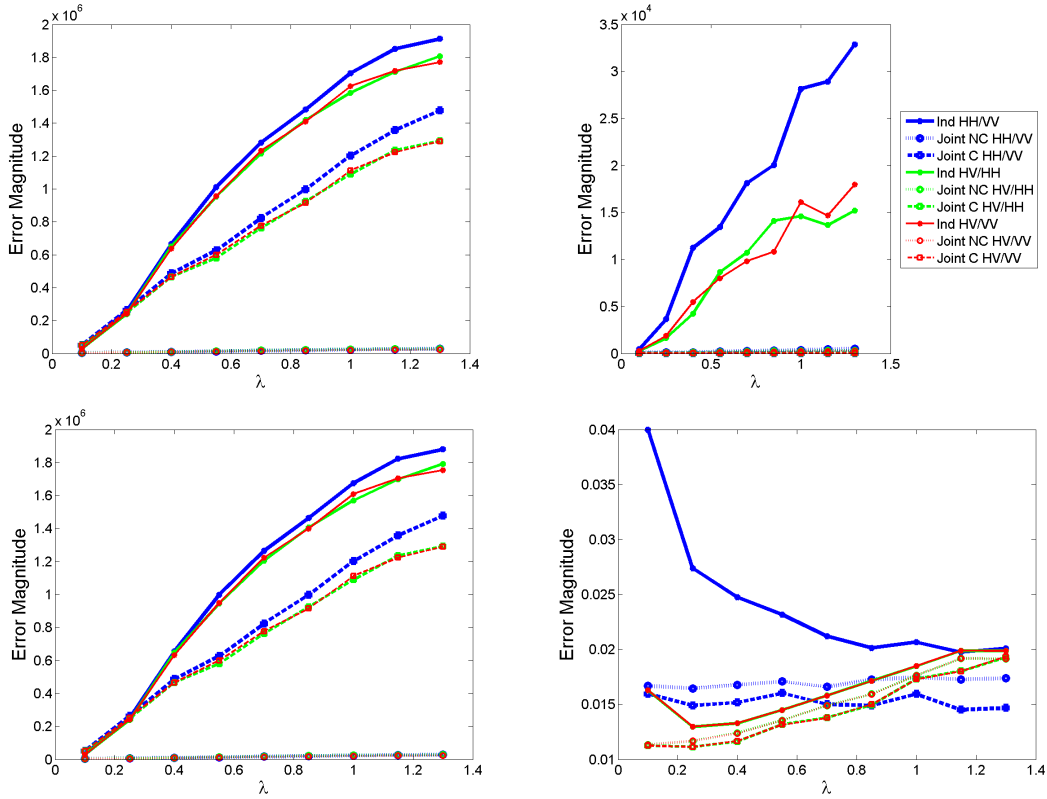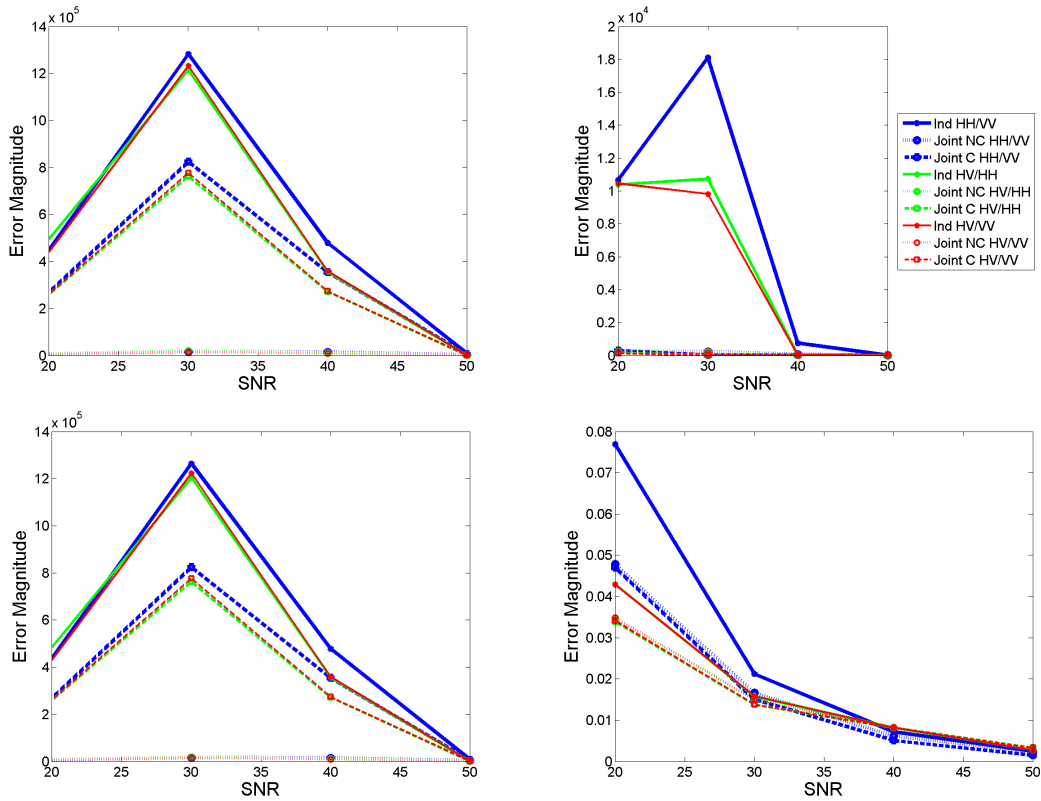
Figure 4.22: The polarimetric preservation cost for the plate scene as a function of λ (SNR = 30 dB). **Top Left**: Full scene error **Top Right**: On-Target error **Lower Left**: Off-Target Error **Lower Right**: Max Pixel Error of polarization preservation of the independent and jointly enhanced images for increasing values of λ.

restored image ratios decreases as λ increases. Moreover, notice that in the plate and dihedral scenes, the full scene and off-target error of the independently restored ratios and convex jointly restored ratios has a peak at 30 dB, which may be due in part to the large amount of 30 dB impulse response smearing throughout the plate and dihedral response.

Next consider the jointly restored image ratios. For all scenes, the non-convex jointly restored polarimetric ratios have a consistently low off and on-target error magnitude. For all scenes, the maximum pixel error of the non-convex jointly restored ratios is lower than the corresponding independently restored ratios, but higher than the corresponding convex
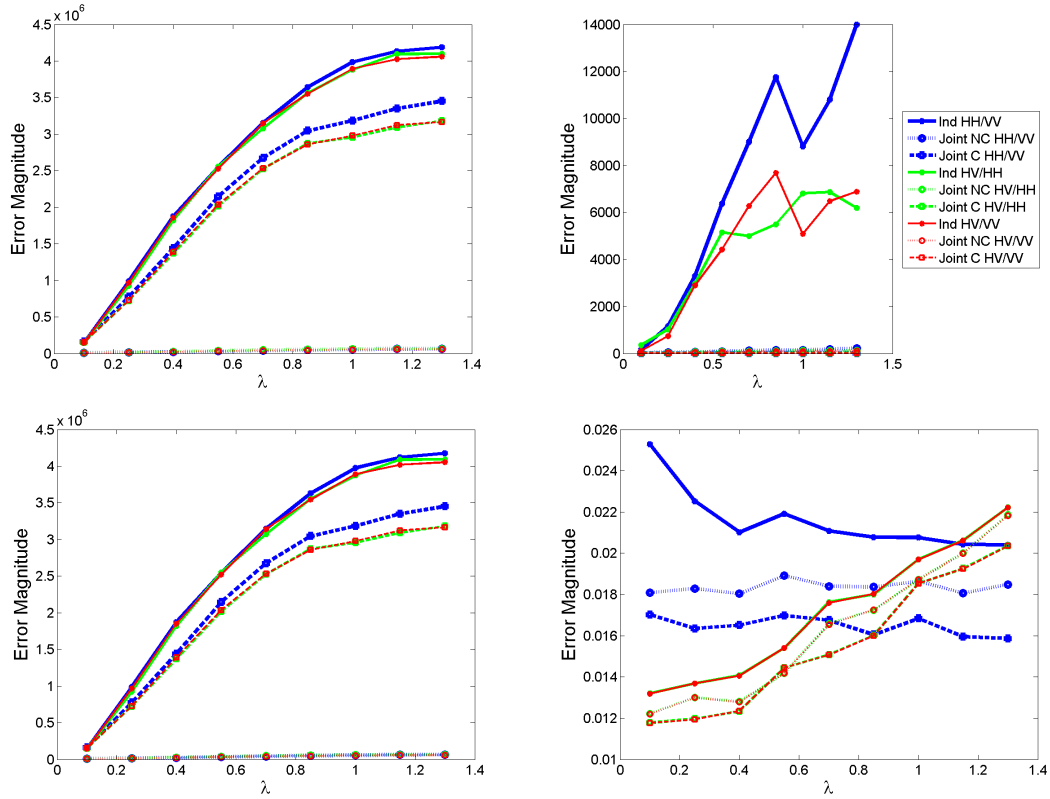
Figure 4.23: The polarimetric preservation cost for the plate scene as a function of SNR ($\lambda = 0.7$). **Top Left**: Full scene error **Top Right**: On-Target error **Lower Left**: Off-Target Error **Lower Right**: Max Pixel Error of polarization preservation of the independent and jointly enhanced images for increasing values of SNR.

jointly restored ratios. These trends are desirable; polarimetric preservation does better in the jointly restored channels compared to the independently restored channels.

Figure 4.24: The polarimetric preservation cost for the dihedral scene as a function of λ (SNR = 30 dB). **Top Left**: Full scene error **Top Right**: On-Target error **Lower Left**: Off-Target Error **Lower Right**: Max Pixel Error of polarization preservation of the independent and jointly enhanced images for increasing values of λ.
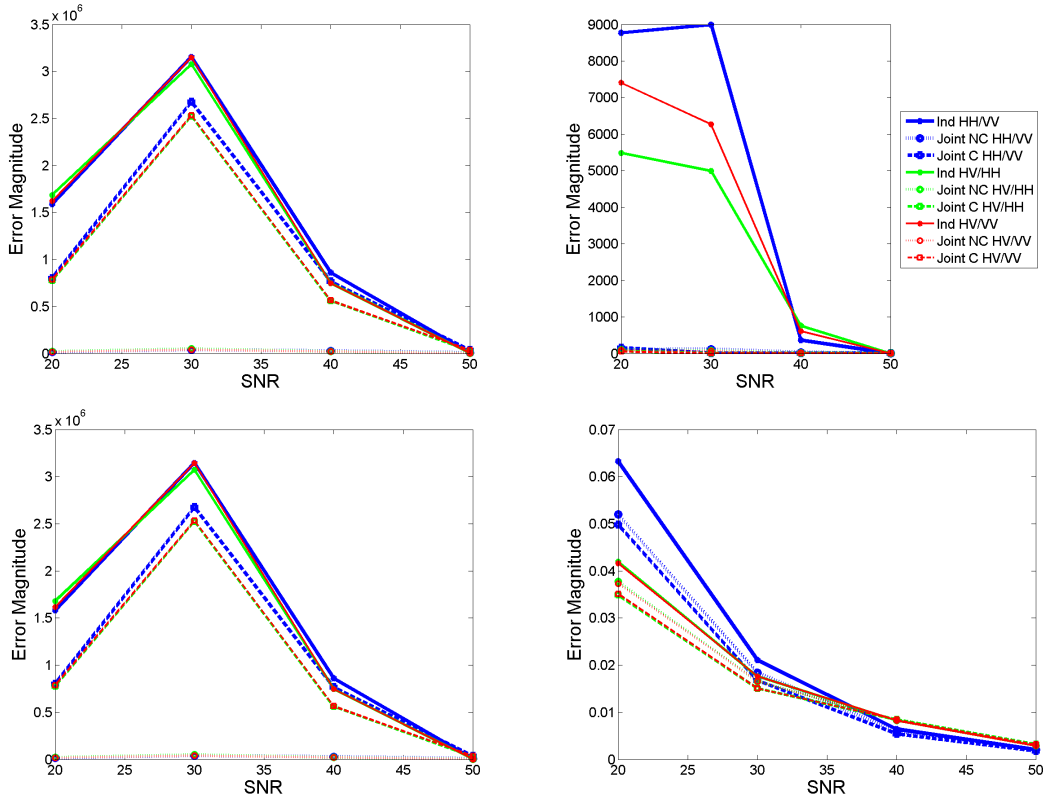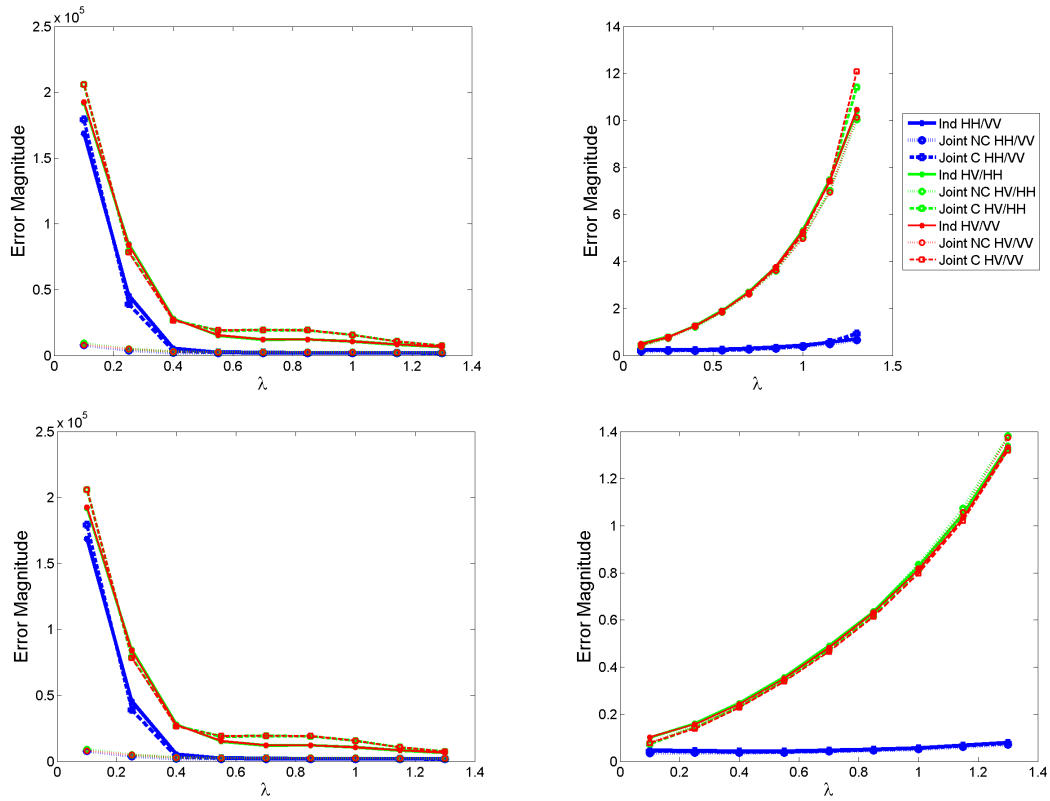
Figure 4.25: The polarimetric preservation cost for the dihedral scene as a function of SNR ($\lambda = 0.7$). **Top Left**: Full scene error **Top Right**: On-Target error **Lower Left**: Off-Target Error **Lower Right**: Max Pixel Error of polarization preservation of the independent and jointly enhanced images for increasing values of SNR.
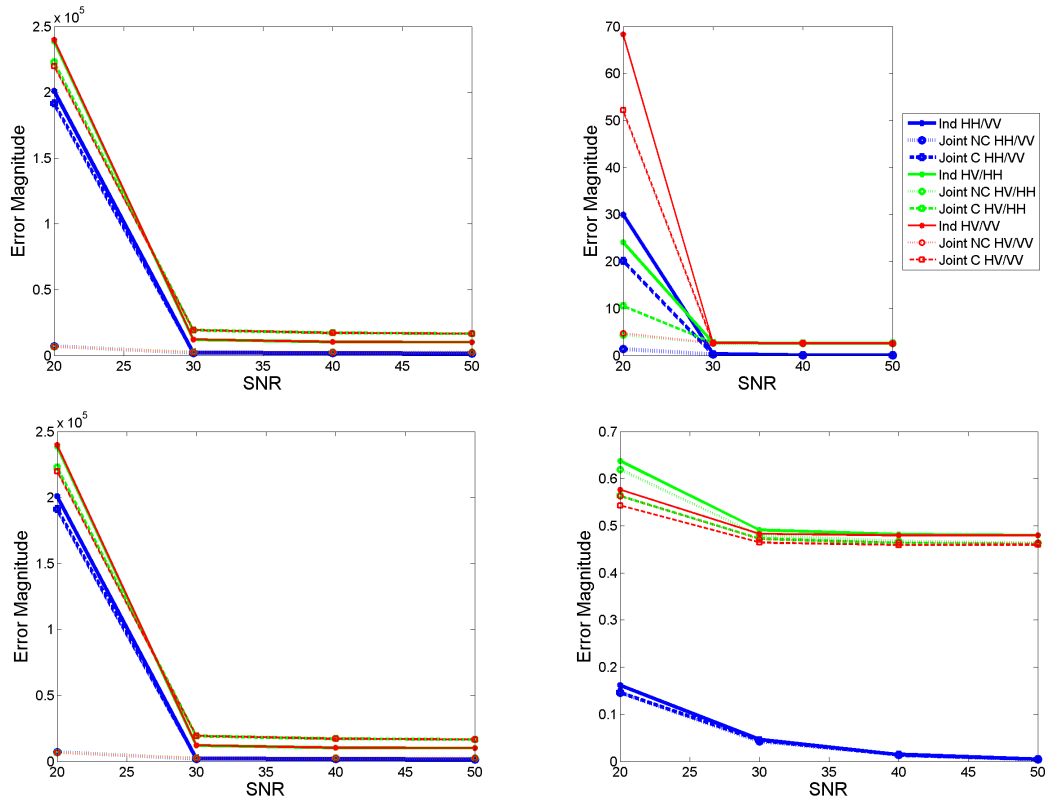
Figure 4.26: The polarimetric preservation cost for the tilted dihedral scene as a function of λ (SNR = 30 dB). **Top Left**: Full scene error **Top Right**: On-Target error **Lower Left**: Off-Target Error **Lower Right**: Max Pixel Error of polarization preservation of the independent and jointly enhanced images for increasing values of λ.
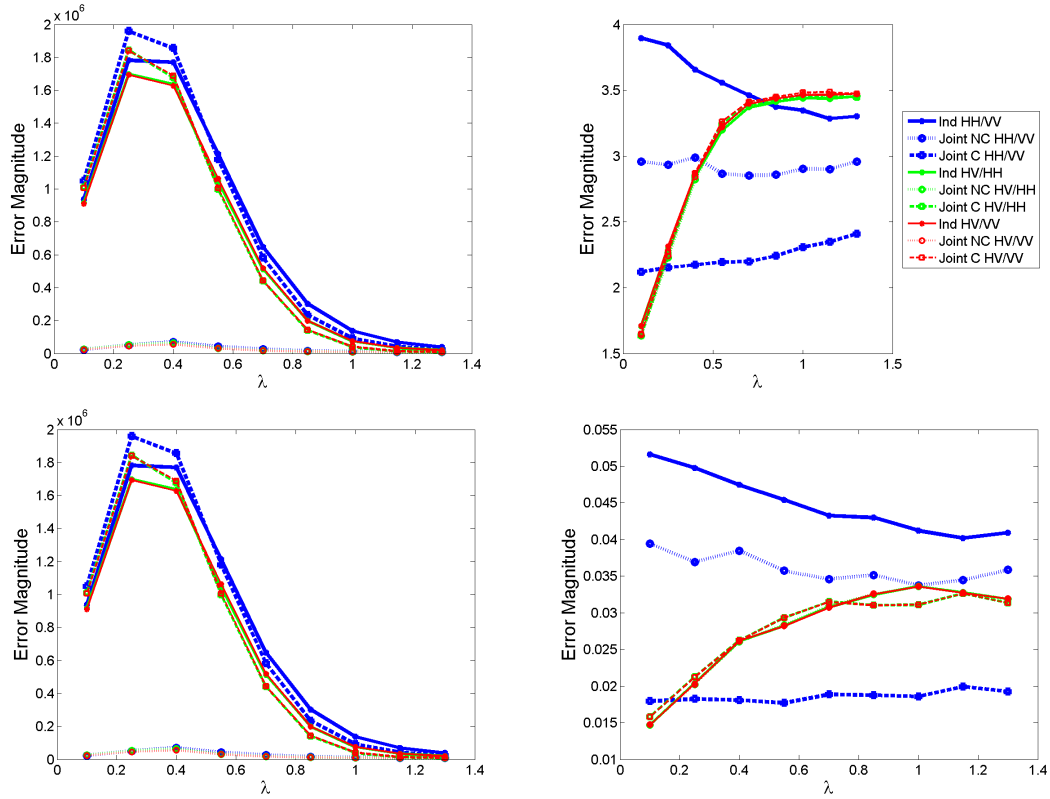
Figure 4.27: The polarimetric preservation cost for the tilted dihedral scene as a function of SNR ($\lambda = 0.7$). **Top Left**: Full scene error **Top Right**: On-Target error **Lower Left**: Off-Target Error **Lower Right**: Max Pixel Error of polarization preservation of the independent and jointly enhanced images for increasing values of SNR.
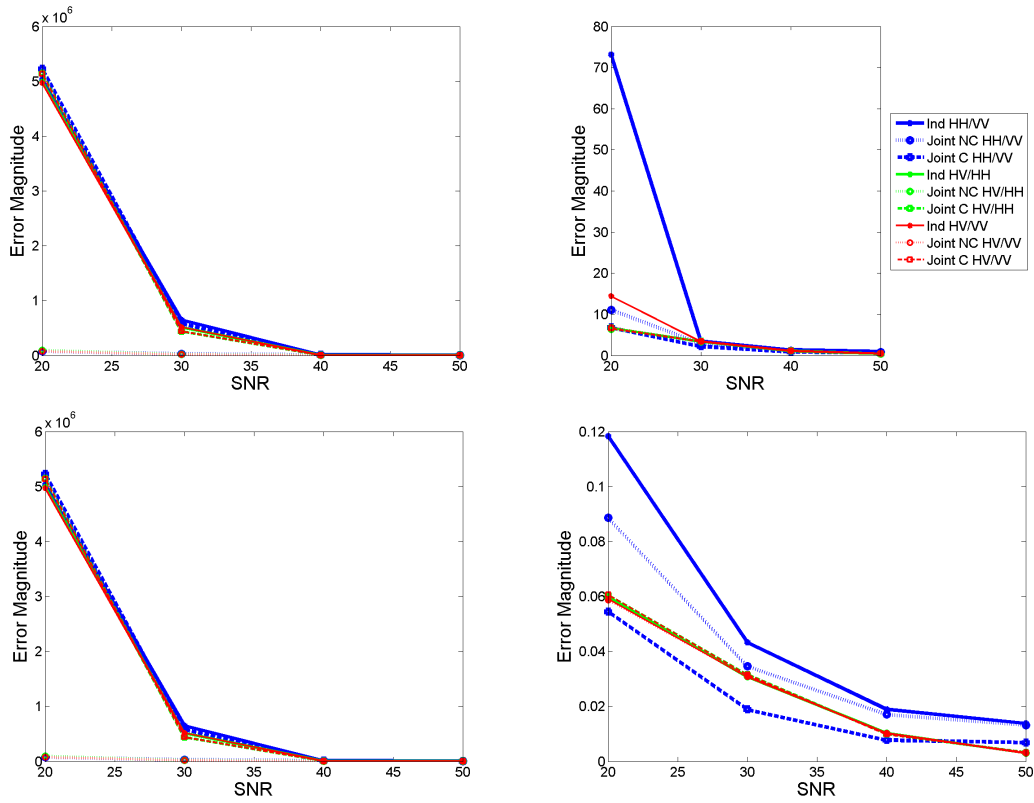
Figure 4.28: The polarimetric preservation cost for the group scene as a function of λ (SNR = 30 dB). **Top Left**: Full scene error **Top Right**: On-Target error **Lower Left**: Off-Target Error **Lower Right**: Max Pixel Error of polarization preservation of the independent and jointly enhanced images for increasing values of λ.

Figure 4.29: The polarimetric preservation cost for the group scene as a function of SNR ($\lambda = 0.7$). **Top Left**: Full scene error **Top Right**: On-Target error **Lower Left**: Off-Target Error **Lower Right**: Max Pixel Error of polarization preservation of the independent and jointly enhanced images for increasing values of SNR.

4.2.4 Scattering Measure.

The scattering measure is considered for each scene region over increasing values of λ and SNR as computed by Eq. (4.6). The error due to improper scattering classification is considered for each canonical shape over increasing values of λ and SNR for the on-target region. Figure 4.30 shows the Pauli basis decomposition of the ideal plate on-target scattering matrix, independently restored images, non-convex jointly restored images and the convex jointly restored images for $\lambda = 0.7$ and SNR = 30 dB. Figure 4.31 compares the plate scattering classification error of the independently restored plate images with both the non-convex jointly restored plate images and convex jointly restored plate images for increasing λ and SNR. Figures 4.32-4.33, 4.34-4.35, and 4.36-4.37 show the corresponding images for the dihedral, tilted dihedral and group scenes, respectively.

First consider the independently restored images. The independently restored images have a consistently lower scattering classification error than the non-convex jointly restored images. However, notice the graph scale indicates that the error cost difference between the all the restored images is less than 0.1. The scattering error of the independently restored images increases as λ increases, and decreases as SNR increases as expected. The independent, convex jointly restored, and non-convex jointly restored scattering classification error tend to converge as SNR increases. Notice, however, that the jointly restored images do perform better in low SNR cases compared to the independently restored images. In particular, the convex jointly restored images have a uniform scattering classification error across λ and SNR.

4.3   Summary

In theory, jointly optimizing polarimetric radar data to enforce sparsity and preserve scattering matrix relationships among image channels should lead to improved target classification. The figures and graphs throughout Ch. 4 demonstrate that the improved preservation in the jointly enhanced channels compared to the independently enhanced

channels did not consistently lead to improved scattering classification efforts under the metric considered. This discrepancy may arise from definition differences between the polarimetric coupling constraint, which preserved scattering matrix relationships of the received signals, and the scattering classification metric, which compared the ideal classification to the estimated classification. However, the jointly enhanced images did perform better in scattering classification than the independently restored images for some low SNR cases. These cases should be considered further, as polarimetric preservation may provide helpful insight into a scene of interest in high noise cases. Moreover, future research could consider ways to rephrase the polarimetric coupling constraint to better reflect imperfections in the received signals.
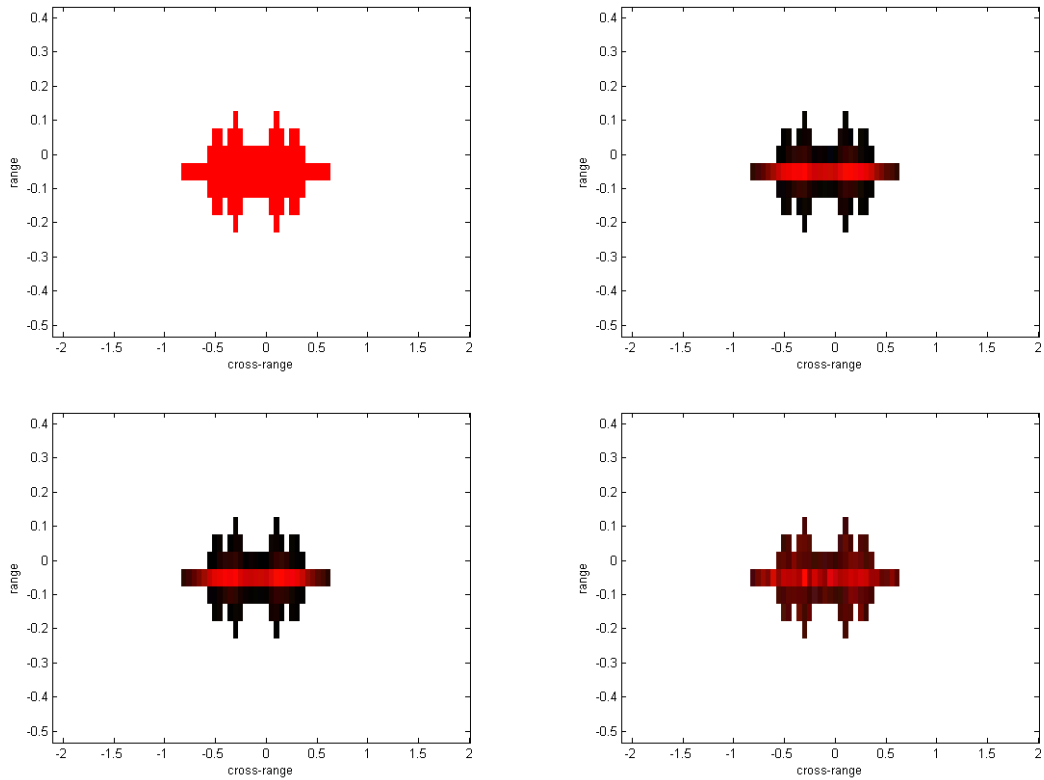
Figure 4.30: Pauli basis decomposition for the plate scene. The **Top Left**: ideal scattering matrix, **Top Right**: independently enhanced images, **Lower Left**: non-convex jointly enhanced images, and **Lower Right**: convex jointly enhanced images at SNR = 30 dB and $\lambda = 0.7$.
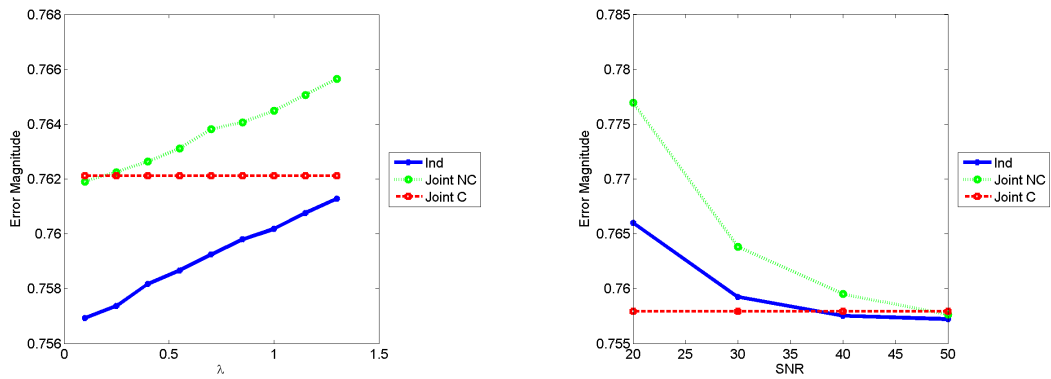

Figure 4.31: On-target average scattering error for the plate scene over λ and SNR.
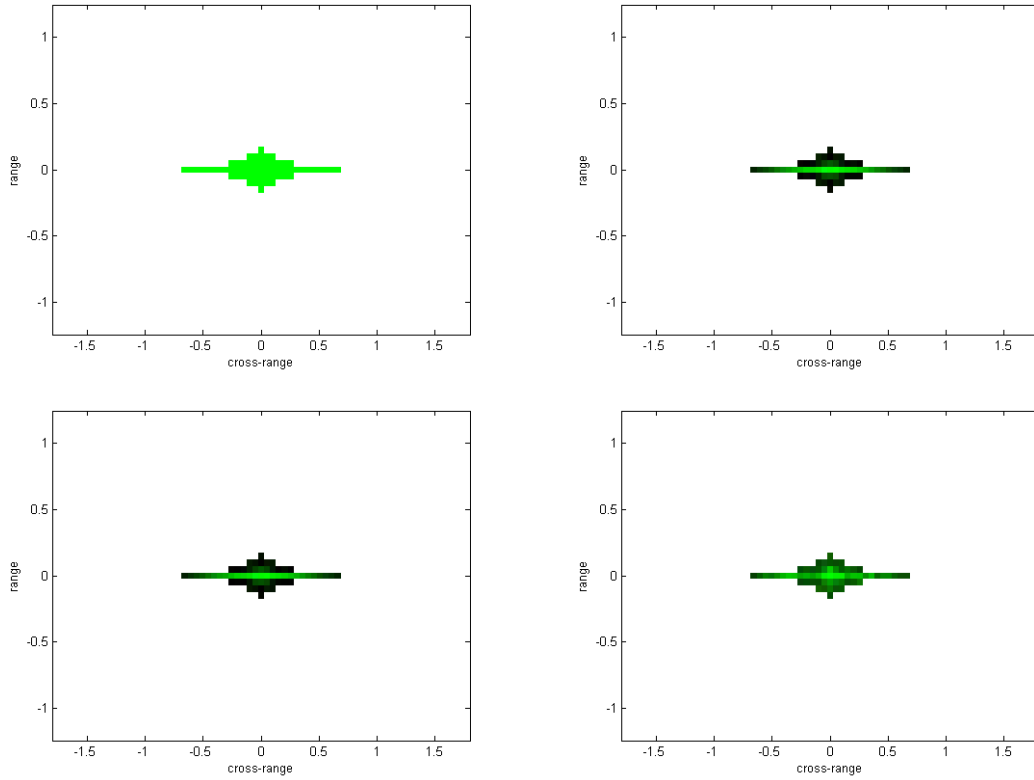
Figure 4.32: Pauli basis decomposition for the dihedral scene. The **Top Left**: ideal scattering matrix, **Top Right**: independently enhanced images, **Lower Left**: non-convex jointly enhanced images, and **Lower Right**: convex jointly enhanced images at SNR = 30 dB and $\lambda = 0.7$.

Figure 4.33: On-target average scattering error for the dihedral scene over λ and SNR.

Figure 4.34: Pauli basis decomposition for the tilted dihedral scene. The **Top Left**: ideal scattering matrix, **Top Right**: independently enhanced images, **Lower Left**: non-convex jointly enhanced images, and **Lower Right**: convex jointly enhanced images at SNR = 30 dB and $\lambda = 0.7$.
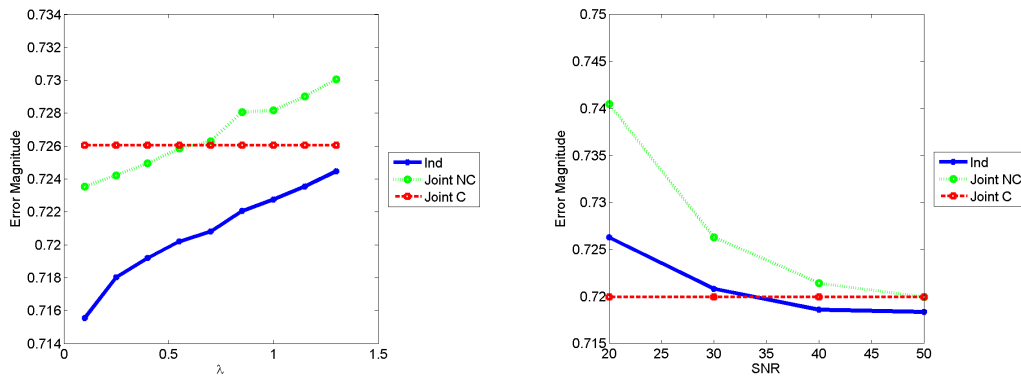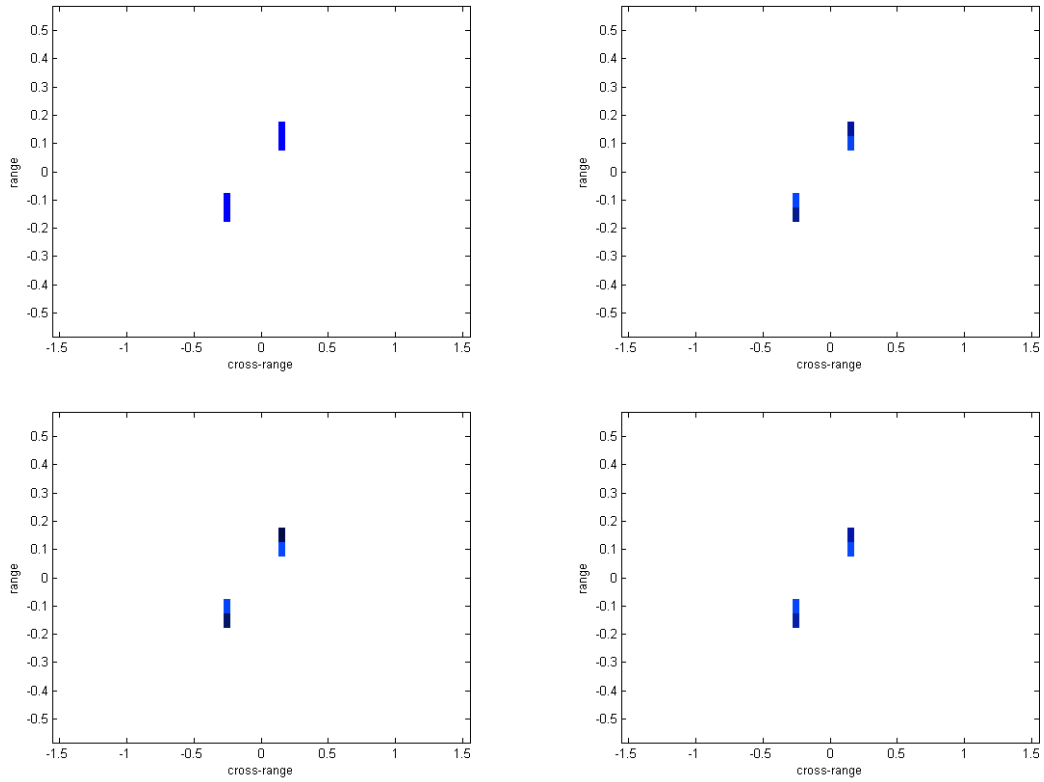

Figure 4.35: On-target average scattering error for the tilted dihedral over λ and SNR.

Figure 4.36: Pauli basis decomposition for the group scene. The **Top Left**: ideal scattering matrix, **Top Right**: independently enhanced images, **Lower Left**: non-convex jointly enhanced images, and **Lower Right**: convex jointly enhanced images at SNR = 30 dB and $\lambda = 0.7$.
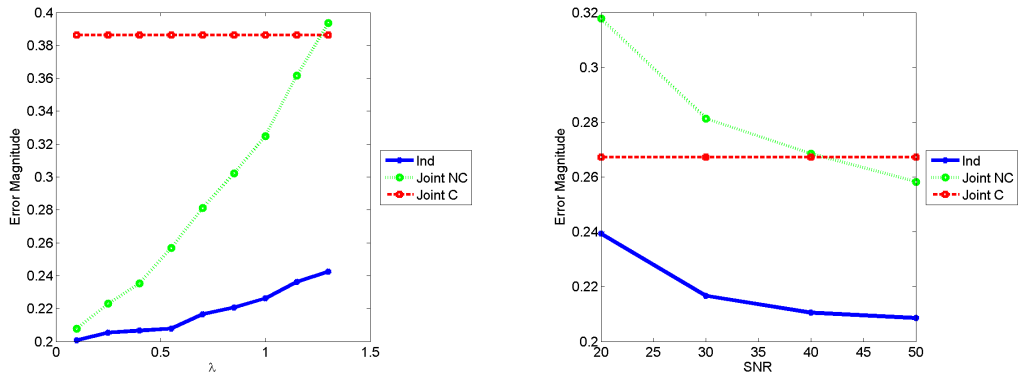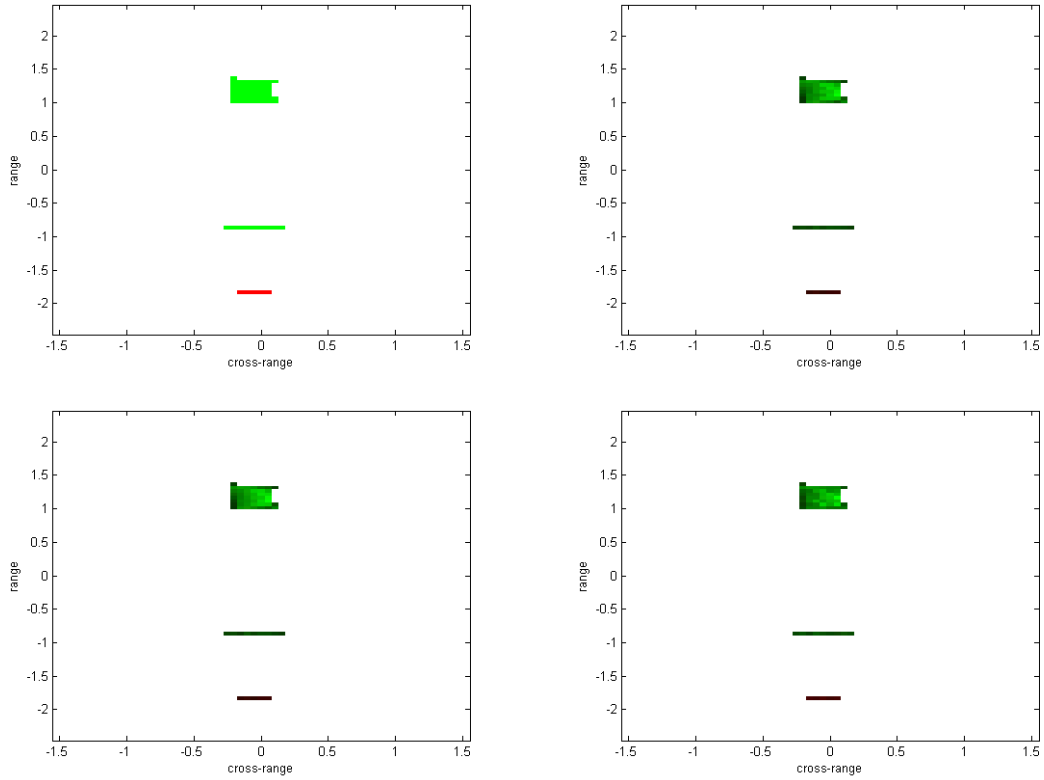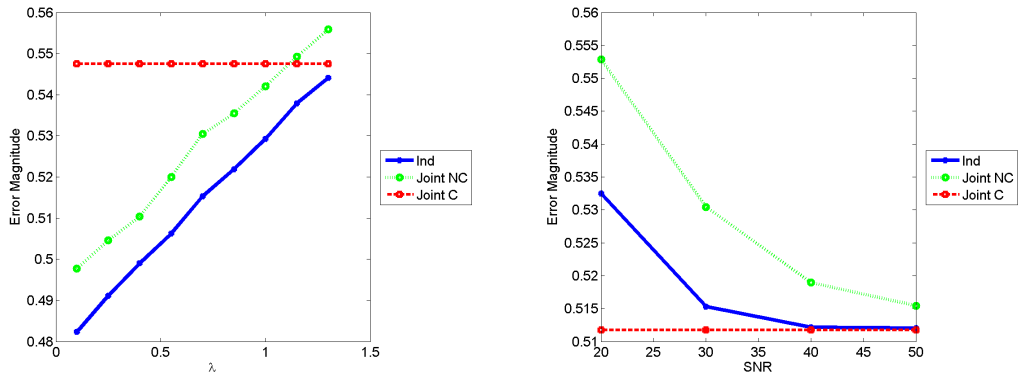

Figure 4.37: On-target average scattering error for the group scene over λ and SNR.

V. Conclusion

S ynthetic aperture radar images contain impulse response effects that appear to smear or blur the image [4]. Sparse imaging is a regularization method that provides a way to overcome limited datasets for image reconstruction [3]. Sparsity constraints enforced alongside data fidelity constraints lead to signal energy placement in only high amplitude pixels [3], thus emphasizing high magnitude scatterers in the scene while reducing the effects of noise and the impulse response.

Image data for a scene of interest may be collected over multiple polarization channels [5]. In the case of polarimetric SAR images, regularization techniques are typically applied independently to each polarimetric channel. However, independent processing does not account for cross-channel coupling and may corrupt the polarimetric information in the signals. Recent research into joint enhancement techniques has shown promising results for multi-channel datasets with similar regions of signal magnitude and/or phase [5, 6]. However, in the case of polarimetric SAR data, scattering may be present in some channels and not in others. This thesis mathematically formulated multi-channel sparse imaging for polarimetric radar data using a joint enhancement algorithm to enforce sparsity and polarimetric coupling constraints.

5.1 Summary of Findings

Two candidate functional relationships were separately considered to describe polarimetric coupling among received signal channels: one convex function g and one non-convex function h. Specifically, these functions were designed to preserve the Sinclair scattering matrix. The two functions g and h were reformed as optimization constraints g_j and h_j, respectively. Then, the coupling constraints were considered separately in an optimization problem constructed to maintain signal fidelity, enforced sparsity, and

preserve inter-channel coupling. The constrained problem was turned into an unconstrained dual problem similar to [5] by adding the sparsity constraint and polarimetric coupling constraint to the objective function using Lagrange multipliers.

An iterative dual gradient descent algorithm [5, 16] was used to alternatively calculate the updated scene estimates for each channel and then the maximizing Lagrange multipliers for each coupling constraint. Results were found for several polarimetric SAR datasets, including simulated radar data of various canonical scatterers. Jointly enhanced images were compared to corresponding images found through independent enhancement, taking into consideration signal fidelity, sparsity, polarimetric preservation, and scattering classification.

Overall, the jointly enhanced image channels displayed significantly better polarimetric preservation compared to the corresponding independently restored image channels. More research is needed to understand how polarimetric preservation can be used to improve target classification.

5.2   Future Research

Future research into this topic could consider the scattering classification improvement of jointly enhanced polarimetric images using more extensive classification tests. For example, one could test whether dictionary estimates of scatterers are improved with jointly enhanced polarimetric images versus independently enhanced polarimetric images. Moreover, future research could consider further polarimetric coupling constraints designed to emphasize desired polarization responses in the image, such as odd bouce or dihedral reflection. This should not be confused with enhancement of image regions, edges, or points, which has been well documented.

Bibliography

[1] W. M. Boerner, *Direct and Inverse Methods in Radar Polarimetry*. Springer, 1992.

[2] M. A. Richards, J. A. Scheer, and W. A. Holm, *Principles of Moder Radar: Basic Principles*. SciTech Publishing, 2010.

[3] L. C. Potter, E. Ertin, J. T. Parker, and M. Cetin, "Sparsity and compressed sensing in radar imaging," *Proceedings of the IEEE*, vol. 98, no. 6, pp. 1006 – 1020, 2010.

[4] C. Jakowatz, D. Wahl, P. Eichel, D. Ghiglia, and P. Thompson, *Spotlight-Mode Synthetic Aperture Radar: A Signal Processing Approach*. Boston, MA: Kluwer Academic Publishers, 1996.

[5] N. Ramakrishnan, E. Ertin, and R. L. Moses, "Enhancement of coupled multichannel images using sparsity constraints," *IEEE Trans. Image Processing*, vol. 19, no. 8, pp. 2115 – 2136, Aug 2010.

[6] P. Scheunders and J. Driesen, "Least-squares interband denoising of color and multispectral images," 2004.

[7] W. M. Boerner, "Polarimetry tutorial," Online: http://www.earth.esa.int, May 2014.

[8] F. T. Ulaby and C. Elachi, *Radar Polarimetry for Geoscience Applications*. Artech House, 1990.

[9] S. Cloude, *Polarisation: Applications in Remote Sensing*. Cary, NC: Oxford University Press, 2009.

[10] J. A. Jackson, "Three-dimensional feature models for synthetic aperture radar and experiments in feature extraction," Ph.D. dissertation, Ohio State University, 2009.

[11] W. L. Cameron, "Feature motivated polarization scattering matrix decomposition," 1990.

[12] D. E. Kreithen, S. D. Halverson, and G. J. Owirka, "Discriminating targets from clutter," *The Lincoln Laboratory Journal*, vol. 5, no. 1, 1993.

[13] M. I. Skolnik, *Introduction to Radar Systems*. New York, NY: McGraw-Hill, Inc., 1980.

[14] A. K. Jain, *Fundamentals of Digital Image Processing*. Englewood Cliffs, NJ: Prentice Hall, 1989.

[15] R. Baraniuk, "Compressive sensing," *IEEE Signal Processing Magazine*, 2007.

[16] T. Kragh and A. Kharbouch, "Monotonic iterative algorithms for SAR image restoration," *IEEE Int. Conf. Image Processing*, pp. 645 – 648, 2006.

[17] O. Batu and M. Cetin, "Parameter selection in sparsity-driven SAR imaging," *IEEE Trans. Aero. Elect. Sys.*, vol. 47, no. 4, 2011.

[18] M. Cetin and W. C. Karl, "Feature-enhanced synthetic aperture radar image formation based on nonquadratic regularization," *IEEE Trans. Image Processing*, vol. 10, no. 4, 2001.

[19] M. Fornasier and H. Rauhut, "Recovery algorithms for vector valued data with joint sparsity constraints," *SIAM Journal of Numerical Analysis*, 2007.

[20] J. Nocedal and S. J. Wright, *Numerical Optimization.* Springer, 1999.

REPORT DOCUMENTATION PAGE

Form Approved
OMB No. 0704–0188

The public reporting burden for this collection of information is estimated to average 1 hour per response, including the time for reviewing instructions, searching existing data sources, gathering and maintaining the data needed, and completing and reviewing the collection of information. Send comments regarding this burden estimate or any other aspect of this collection of information, including suggestions for reducing this burden to Department of Defense, Washington Headquarters Services, Directorate for Information Operations and Reports (0704–0188), 1215 Jefferson Davis Highway, Suite 1204, Arlington, VA 22202–4302. Respondents should be aware that notwithstanding any other provision of law, no person shall be subject to any penalty for failing to comply with a collection of information if it does not display a currently valid OMB control number. **PLEASE DO NOT RETURN YOUR FORM TO THE ABOVE ADDRESS.**

1. REPORT DATE *(DD–MM–YYYY)*	2. REPORT TYPE	3. DATES COVERED *(From — To)*
19–06–2014	Master's Thesis	Oct 2012- Jun 2014

4. TITLE AND SUBTITLE

Enhanced Polarimetric Radar Imaging Using Cross-Channel Coupling Constraints

5a. CONTRACT NUMBER

5b. GRANT NUMBER

5c. PROGRAM ELEMENT NUMBER

6. AUTHOR(S)

Perhai, Andrea E., Contractor, USAF

5d. PROJECT NUMBER

5e. TASK NUMBER

5f. WORK UNIT NUMBER

7. PERFORMING ORGANIZATION NAME(S) AND ADDRESS(ES)

Air Force Institute of Technology
Graduate School of Engineering and Management (AFIT/EN)
2950 Hobson Way
WPAFB, OH 45433-7765

8. PERFORMING ORGANIZATION REPORT NUMBER

AFIT-ENG-T-14-J-9

9. SPONSORING / MONITORING AGENCY NAME(S) AND ADDRESS(ES)

Intentionally Left Blank

10. SPONSOR/MONITOR'S ACRONYM(S)

11. SPONSOR/MONITOR'S REPORT NUMBER(S)

12. DISTRIBUTION / AVAILABILITY STATEMENT

DISTRIBUTION STATEMENT A:
APPROVED FOR PUBLIC RELEASE; DISTRIBUTION UNLIMITED

13. SUPPLEMENTARY NOTES

This work is declared a work of the U.S. Government and is not subject to copyright protection in the United States.

14. ABSTRACT

Data for a scene of interest may be collected over multiple polarization channels. In the case of polarimetric synthetic aperture radar images, regularization techniques are typically applied independently to each polarimetric channel. However, independent processing does not account for cross-channel coupling and may corrupt the polarimetric information in the signals. Recent consideration of joint enhancement techniques has shown promising results for multi-channel datasets with similar regions of signal magnitude and/or phase. However, in the case of polarimetric SAR data, scattering may be present in some channels and not in others. This thesis mathematically formulates multi-channel sparse imaging for polarimetric radar data using a joint enhancement algorithm to enforce sparsity and polarimetric coupling constraints.

Two candidate functional relationships are derived to describe polarimetric coupling among received signal channels: one convex function and one non-convex function. These functions are reformed as optimization constraints. Then, an optimization problem is constructed to maintain signal fidelity, enforce sparsity, and preserve interchannel coupling.

An iterative dual gradient descent algorithm is used to alternatively calculate updated scene estimates for each channel and the maximizing Lagrange multipliers for each coupling constraint. Results are found for several polarimetric SAR datasets. Jointly enhanced images are compared with corresponding images found through independent enhancement, taking into consideration signal fidelity, sparsity, polarimetric preservation, and scattering classification.

Overall, the jointly enhanced image channels display significantly better polarimetric preservation compared to the corresponding independently restored image channels. More research is needed to understand how improved polarimetric preservation can be used to improve target classification.

15. SUBJECT TERMS

Joint Optimization, Multichannel Data, Sparsity, Polarization

16. SECURITY CLASSIFICATION OF:			17. LIMITATION OF ABSTRACT	18. NUMBER OF PAGES	19a. NAME OF RESPONSIBLE PERSON
a. REPORT	b. ABSTRACT	c. THIS PAGE			Dr. Julie A. Jackson (ENG)
U	U	U	UU	90	**19b. TELEPHONE NUMBER** *(include area code)* (937) 255-3636 x4678 julie.jackson@afit.edu

Standard Form 298 (Rev. 8–98)
Prescribed by ANSI Std. Z39.18